Micro-optical fiber switch for a large number of interconnects

Yves-Alain Peter

Université de Neuchâtel
Institut de Microtechnique

Micro-optical fiber switch for a large number of interconnects

Thèse

Présentée à la Faculté des sciences
pour obtenir le grade de docteur ès sciences
par

Yves-Alain Peter

Neuchâtel, janvier 2001.

IMPRIMATUR POUR LA THESE

Micro-optical fiber switch for large number of interconnects

de M. Yves-Alain Peter

UNIVERSITE DE NEUCHATEL

FACULTE DES SCIENCES

La Faculté des sciences de l'Université de Neuchâtel sur le rapport des membres du jury,

MM. R. Dändliker (directeur de thèse), H.-P. Herzig, M.O. Solgaard (Stanford CA, USA) et G.-L. Bona (IBM, Rüschlikon)

autorise l'impression de la présente thèse.

Neuchâtel, le 23 janvier 2001

Le doyen:

J.-P. Derendinger

Abstract

During the past few years, the demand for optical telecommunications has boomed (*Scientific American*, January 2001). In order to satisfy this demand, new optical switches are required to replace the electrical switches used up until now. In this work, 1 × N optical switches are studied. Theoretical investigations are conducted to describe the physical properties of the switches and to determine their limitations. The merit function of optical switches is their power coupling efficiency. The limitations are mainly aberrations and misalignments of the optical components. We experimentally demonstrate these limitations and realize improvements to the optical switch. Two approaches have been chosen. The first is to use an adaptive mirror for the correction of the aberrations. The second is to integrate microlenses into the optical switch in order to reduce the aberrations and to relax the alignment tolerances. Both approaches have been realized and have brought significant improvements in power coupling efficiency. With the experiment, we demonstrate an optical switch allowing up to 3019 receiver fibers to be addressed. The measured coupling efficiency (including losses due to the optical elements) is between 6 dB and 3 dB for the adaptive system and between 3 dB and 2 dB for the system using microlenses.

Contents

Chapter 1

Introduction

1.1 Historical background

Optical communication originates back to antiquity. Most civilizations used fire and smoke signals to convey a single piece of information. Later, reflecting mirrors played the same role. Until the beginning of the 19th century the same idea had been used to transmit communications optically. Only the basic elements were improved, from fire to signaling lamps, flags or semaphore. The rate of transmitted information however remained very low, less than 1 bit per second.

In the 1830s, telegraphy replaced the use of light and began the era of electrical communications. With the use of coding techniques, such as Morse, the transmission rate increased up to 10 bits per second. In 1876, Graham Bell invented the telephone. This invention represented a major revolution in the communications as the electric signal was transmitted in the analog form. The same technique dominated communication systems for a century. With the use of coaxial cables, the system capacity increased considerably, up to 100 Mb/s in the 1970s. Such high-speed coaxial systems have nevertheless a major drawback: the need for repeaters placed at almost every kilometer that makes these systems relatively expensive to operate. The capacity of communication systems is measured through the bit rate-distance product BL, where B is the bit rate and L the repeater spacing. In the 1970s, electrical systems with $BL \sim 100$ (Mb/s)·km were available and limited to such values by fundamental limitations.

In 1880, four years after his invention of the telephone, Graham Bell sought to send speech over a visible light beam [1]. The photophone was born and able to transmit speech information over distances of several hundred meters. Although, the photophone was impractical (line transmission in the atmosphere is restricted to line of sight and severely affected by disturbances such as rain, snow, fog, dust and atmospheric turbulence), the basic elements employed in all forms of optical

telecommunications were there. An information-bearing signal modulates a light source. The light is transmitted through a medium and a detector recovers the modulation of the signal. However, neither a powerful coherent optical source, nor a suitable transmission medium was available.

In 1960, Maiman developed the laser which was the first generation of coherent light [2]. In 1966, Kao and Hockham suggested the use of optical fibers based on silica glass as transmission media for lightwave communications [3]. With these two major developments, the way to the era of optical telecommunications was open. In 1970, the fiber loss which was as high as 1000 dB/km was dramatically reduced down to 20 dB/km [4]. At about the same time, heterostructures AlGaAs/GaAs semiconductor lasers, operating continuously at room temperature, were demonstrated by Alferov (Nobel Prize in physics 2000) [5] and Hayashi [6]. Low loss optical fibers and compact optical sources were then available. These developments gave rise to the first generation of lightwave communication systems operating near 0.8 μm [7]. They operated at a bit rate in the 50-100 Mb/s range with a repeater spacing of about 10 km ($BL \sim 500$ (Mb/s)·km). Such a value was larger than the one reached by electrical systems ($BL \sim 100$ (Mb/s)·km). However, the bit rate was limited because of modal dispersion in multimode fibers. To overcome this limit, singlemode fibers have been developed. These fibers are characterized by a low pulse spreading which results in a small response time and in consequence in a large bandwidth. The bandwidth is directly proportional to the information carrying capacity. During the 1970s, InGaAs semiconductor lasers and detectors operating near 1.3 μm were developed [8]. The low attenuation ($\sim$0.35 dB/km) and minimum dispersion ($\sim$0.5 (ps/km)·nm) of light in the optical fibers in this wavelength region made possible the second generation of fiber optic communication systems in the early 1980s with a repeater spacing of 20 km. These improvements led to a 2 Gb/s rate with a repeater spacing of 50 km in the 1980s ($BL \sim 100$ (Gb/s)·km) [9]. The third generation lightwave systems operates at 1.55 μm in order to further decrease the attenuation ($\sim$0.2 dB/km). However, at this wavelength, the dispersion ($\sim$10 (ps/km)·nm) is larger than at 1.3 μm. This drawback is overcome in using dispersion shifted fibers designed to have minimum dispersion near 1.55 μm or/and by limiting the laser spectrum to a single longitudinal mode. Fiber optic communication systems of the third generation are operating at bit rates up to 10 Gb/s over distances of 100 km ($BL \sim 1$ (Tb/s)·km) [10].

1.2 Motivation

During the last years, the demand for more data capacity in telecommunication networks has dramatically increased, mainly due to the internet. In order to satisfy this demand, the use of multiple different wavelength carriers in

the same optical fiber has been introduced. Until 1994, Wavelength-division-multiplexing (WDM) transmission at 1.55 μm was limited by the instability of laser sources. However, recent developments with tunable lasers: distributed Bragg reflector (DBR) lasers and distributed-feedback (DFB) lasers enabled to overcome this problem [11]. Moreover, the development of Erbium doped fiber amplifiers (EDFA) enabled an increase in the repeater spacing. The advent of dense wavelength-division multiplexing (DWDM) optical communication systems (channel separation $\lesssim$ 1 nm), enhanced by the development of EDFA allowed an increase in fiber capacity in the range of 1 Tb/s over 400 km [12] ($BL \sim 400$ (Tb/s)·km). Such a system has 100 separate wavelengths (channels) carrying 10 Gb/s each. The separation between each channel is 0.2 nm. Very recently, a new optical fiber fabrication method has been proposed to enable low attenuation in the wavelength range 1.3 μm-1.6 μm. This will allow to use a telecommunication window as large as 40 THz [13]. Practical realization of a Wideband Wave Division Multiplexing (WWDM) has been announced by Lucent Technologies and Canoga Perkins [14].

We saw how the capacity of telecommunication systems exploded, thanks to new sources, new amplifiers and improved fabrication method of optical fibers. Until recently, electronic switches were used to route the information. However, with the huge capacity of today's WDM telecommunication systems, the use of electronic switches become expensive. Moreover, the optic-electronic-optic conversion at each node is cumbersome. The need for a new type of large capacity, wavelength independent switches naturally opened the way to optical switches.

1.3 Optical switches in telecommunication systems

Figure 1.1 [15] shows a general switching architecture in an all optical telecommunication network. If no electronic conversion is involved anymore, the system is said *transparent*. Several types of optical switches are needed depending of the functionality required (circuit or packet switching, restoration, etc...). A switch can be a 1 to 1 on-off switch, a 2 $\times$ 2 crossbar switch, a 1 $\times$ N switch or a N $\times$ N cross-connect. Figure 1.2 [16] shows these four types of switches. Several technologies are commonly used to realize optical switches. The input/output fibers can be interconnected mechanically, using a robot [17]. Such a device has a large number of interconnects (512 $\times$ 512), is slow (1 min), large in size, but has very low insertion loss ($\sim$1 dB) and no crosstalk. Smaller and more compact 1 $\times$ N mechanical switches moving the fibers [18, 19] have much shorter switching times (tens of ms), very low insertion loss ($\sim$1 dB), and very low crosstalk (-60 dB). Similar 1 $\times$ 2 micro-mechanical switches moving waveguides have been realized

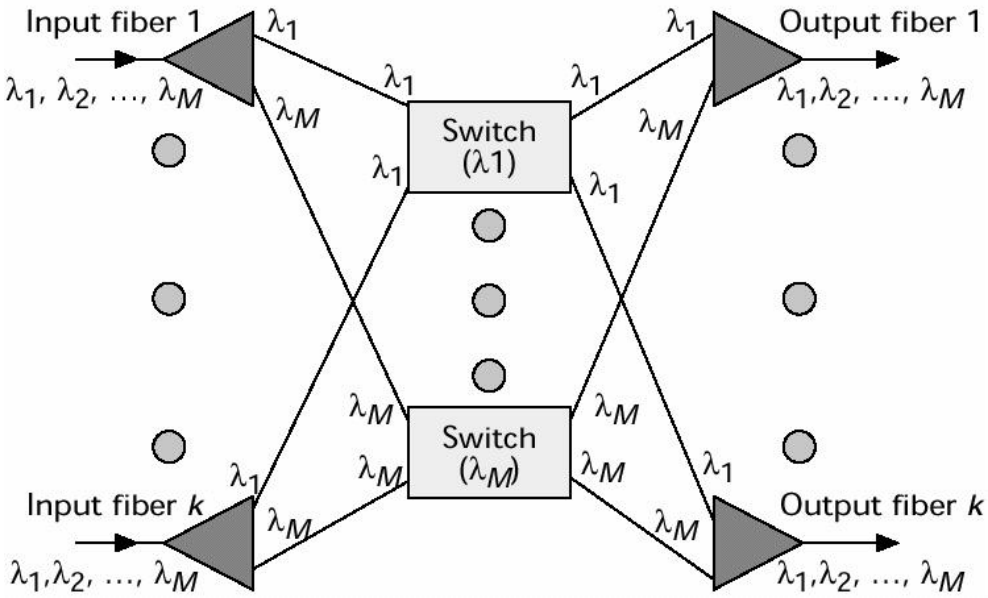

Figure 1.1: General switching architecture of a WDM network (from Elmirghani [15]).

[20] and show 4 dB insertion loss, crosstalk better than -45 dB and switching times in the order of 400 μs. Approaches using micro-optical elements (microlenses and microprisms) show interesting results for large number of interconnects. Microprisms have been used to interconnect 1 $\times$ 10 fibers with 2 dB insertion loss, -50 dB crosstalk and 1 ms switching time [21]. Rotating prisms have been used to interconnects 1 $\times$ 160 fibers with 3.5 dB insertion loss, and 2 ms switching time [22]. A more complex micro-optical switch has been proposed to interconnect N $\times$ N fibers using microlenses [23]. A 1 $\times$ 8 optical switch has been realized using a rotary electrostatic micromotor with 2 dB insertion loss, -45 dB crosstalk and 100 ms switching time [24]. The technology of micro-electro-mechanical systems (MEMS) is widely used to realize optical cross-connects. Using bulk silicon micromachining and surface silicon micromachining, several optical switches have been realized [25, 26, 27, 28]. They enable large number of interconnects, low insertion loss, small crosstalk and switching time in the range of 1-10 ms. For specific characteristics, please refer to Tab. 1.1. All the above mentioned technologies are wavelength independent and polarization independent.
Other technological approaches are investigated which are wavelength dependent and polarization dependent. Among these are integrated optics (IO) planar waveguide switches. Thermooptic [29] or electrooptic [30] Mach-Zehnder interferometer (MZI) switching devices have been reported. Thermooptic beam steering has been realized for 8 x 8 switch [31]. Finally, ferroelectric [32], chiral [33] or nematic [34] liquid crystal (LC) switches have been reported. The main drawback

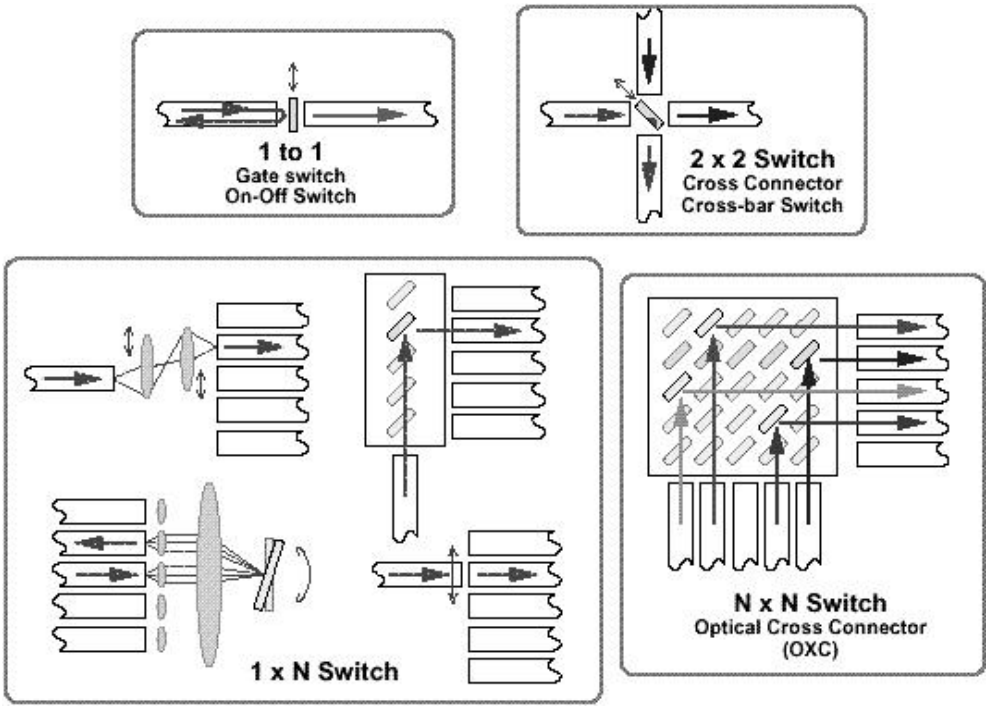

Figure 1.2: Four types of switches (from Fujita and Toshiyoshi [16]).

of these devices is their relatively large crosstalk. Table 1.1 summarizes also the characteristics of these optical switches.

The aim of this work is to investigate a micro-optical fiber switch for large number of interconnects (1 × N), with N>1000. Although switches with small number of interconnects (1 × 2, 2 × 2) are commercially available, switches with large number of interconnects are more critical due to high precision alignment requirements and large aberrations. We will use a $4f$ imaging system and investigate alignment tolerances and aberrations. We will propose and realize solutions to make alignment tolerances less critical (using microlenses) and to correct the aberrations (using a deformable mirror). The practical realization of the optical systems will be demonstrated at a wavelength of λ=633 nm. Although the commercial telecommunication systems use wavelengths between 1.3 μm and 1.6 μm, the use of a shorter wavelength does not affect the validity of the results, since the micro-optical switches presented in this work are basically wavelength independent. Only the alignment tolerances will be less critical at a wavelength $1.3 \lesssim \lambda \lesssim 1.6$ μm, due to the larger diameter of the core of the singlemode fibers for longer wavelengths ($\phi_{core} \cong 4.5$ μm at λ =633 nm and $\phi_{core} \cong 10.5$ μm at $\lambda = 1.5$ μm).

Technology	**Switch**	**Insertion loss**	**Crosstalk**	**Switching time**	**Reference**
Moving optical fiber	N × N	1 dB	no	100 ms-1 min	[17, 18, 19]
Moving waveguide	1 × 2	4 dB	-45 dB	400 μs	[20]
Microprisms	1 × 10	2 dB	-50 dB	1 ms	[21]
Prisms	1 × 160	3.5 dB		2 ms	[22]
Rotary micromotor	1 × 8	2 dB	-45 dB	100 ms	[24]
Vertical micromirrors	32 × 32	7 dB	-50 dB	2 ms	[25, 26]
Vertical micromirror	2 × 2	2 dB	-50 dB	1 ms	[27]
Micromirror array	112 × 112	7.5 dB	-50 dB	10 ms	[28]
IO thermooptic MZI	2 × 2	1 dB	-21 dB	150 μs	[29]
IO electrooptic MZI	4 × 4	5 dB	-15 dB	200 ps	[30]
IO thermooptic	8 × 8	8.4 dB	-22 dB	1 ms	[31]
Ferroelectric LC	2 × 2	7 dB	-34 dB	35 μs	[32]
Chiral LC	2 × 2	1.4 dB	-26 dB	40 ms	[33]
Nematic LC	2 × 2	1.4 dB	-20 dB	250 μs	[34]

Table 1.1: Comparison of the performance of optical space switches using different technology approaches.

1.4 Outline of this thesis

This thesis describes the investigation and the realization of free space optical switches for large number of interconnects (1 × N), for applications in telecommunication systems. Different optical systems are investigated, considering particularly the influence of the aberrations on the power coupling efficiency. Switching systems correcting adaptively the aberrations, and low aberration switching systems are realized practically. These realizations demonstrates the feasibility of 1 × N systems with N larger than 3000.

This thesis is divided into four main chapters.
In **chapter 2**, we present the theoretical background with the main physical laws used to describe and investigate our systems. The propagation of light in fibers, in free space and through an optical system is described. Non paraxial raytracing is introduced and a description of the aberrations is done using Zernike polynomials. Finally, we detail a method to calculate the power coupling efficiency of the switching systems.

In **chapter 3**, we investigate several systems and calculate their aberrations and their coupling efficiency. Limitations in size, number of interconnects and alignment tolerances are given. The deformable mirror used in the adaptive system correcting the aberrations is described as well as its driving genetical algorithm.

The description of the low aberration system using microlenses is detailed.

In **Chapter 4** we present the experimental results for three systems: a first system limited by the aberrations, the adaptive system correcting the aberrations with a deformable mirror and the low aberration system using microlenses.

Chapter 5 concludes this thesis with a summary of the most important results and a comparison with other optical switching systems.

Chapter 2

Theory

This chapter presents the fundamental physical laws needed to describe an optical switch. Section 2.1 is dedicated to the description of light propagation. First, the guided modes propagation of light in single mode fibers is detailed. Then, the paraxial propagation of a Gaussian beam in free space (air) as well as the transformation by a lens is introduced. In section 2.2, a geometrical description of light propagation (raytracing) is introduced to describe the aberrations generated by the optical elements (lens, mirror,...). Finally, section 2.3 is dedicated to the computation of light coupling into a fiber.

2.1 Light propagation

2.1.1 Light propagation in step-index fibers

An optical fiber is a cylindrical waveguide. A brief mathematical description will show that light propagates in modes inside the fibers. The description will be restricted to step-index singlemode fibers.

Figure 2.1 shows a step-index fiber. It is composed of a core, a cladding and a jacket. It is a cylindrical dielectric waveguide made of silica glass (SiO_2) with low concentrations of doping materials like titanium, germanium or boron. Figure 2.2 shows the cross section and index profile of a step-index fiber. The numerical aperture NA is given by

$$NA = \sqrt{n_1^2 - n_2^2}, \tag{2.1}$$

where n_1 is the refractive index of the core and n_2 the refractive index of the cladding. If the core radius a is much larger than the wavelength λ, a geometrical-optics description for the propagation of light is valid. However, when a is in the order of λ, a wave-propagation theory is needed. In modern communication systems using fibers, the core diameter $2a$ is typically 10 μm for a wavelength $\lambda = 1550$ nm. In this work, fibers with a core diameter a of typically 4 μm for a

wavelength of $\lambda = 633$ nm are used. However, the general principe is identical. For these values of a and λ, a wave-propagation treatment is necessary.

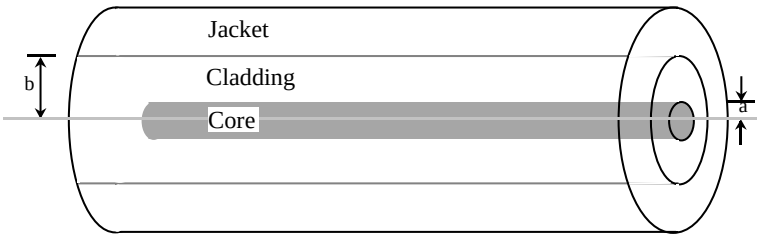

Figure 2.1: Schematic drawing of a step-index fiber.

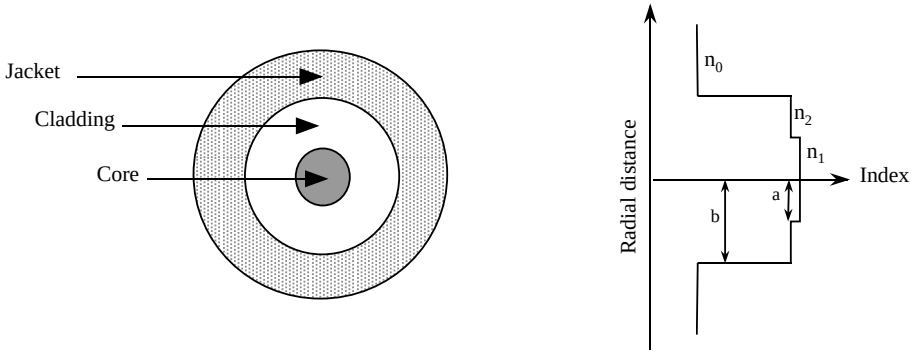

Figure 2.2: Cross section and index profile of a step-index fiber.

Several text books [35, 36, 37] describe the mathematical derivation which leads to the description of the propagation of monochromatic light in step-index fiber as optical modes. Here, a short summary will be given, highlighting the major results. In electromagnetic theory, we determine the electric and magnetic fields of guided waves that satisfy Maxwell's equations and the boundary conditions imposed by the cylindrical dielectric core and the cladding of the fiber. Each component of the electric and magnetic field must satisfy the Helmholtz equation [38]

$$\nabla^2 U + n^2 k^2 U = 0, \tag{2.2}$$

where the refractive index is $n = n_1$ in the core ($r \leqslant a$) and $n = n_2$ in the cladding ($r \geqslant a$). $k = 2\pi/\lambda$ is the wave number. Since the refractive index profile $n(r)$ is cylindrically symmetric, we use cylindrical coordinates (r, ϕ, z). In these coordinates, the wave equation (2.2) becomes

$$\frac{\partial^2 U}{\partial r^2} + \frac{1}{r}\frac{\partial U}{\partial r} + \frac{1}{r^2}\frac{\partial^2 U}{\partial \phi^2} + \frac{\partial^2 U}{\partial z^2} + n^2 k^2 U = 0, \tag{2.3}$$

where $U = U(r, \phi, z)$ represents any of the axial components E_z and H_z in cylindrical coordinates. The other components E_r, E_ϕ, H_r, H_ϕ can be calculated in terms of E_z and H_z using Maxwell equations. We are interested in solutions that take the form of waves traveling in the z direction with a propagation constant β, so that the z dependence of U is of the form $e^{-i\beta z}$. Since U must be a periodic function of the angle ϕ with period 2π, we assume that the dependence on ϕ is harmonic, $e^{-i\ell\phi}$, where ℓ is an integer. Substituting the general expression of a mode

$$U(r, \phi, z) = u(r)e^{-i\ell\phi}e^{-i\beta z}, \qquad \ell = 0, \pm 1, \pm 2, ..., \tag{2.4}$$

into (2.3), we get for $u(r)$ the differential equation

$$\frac{d^2u}{dr^2} + \frac{1}{r}\frac{du}{dr} + (n^2k^2 - \beta^2 - \frac{\ell^2}{r^2})u = 0. \tag{2.5}$$

Since we want a propagating wave in the core ($\beta < n_1 k$), and an evanescent wave in the cladding ($\beta > n_2 k$), we define

$$n_1^2k^2 - \beta^2 = \alpha^2 \tag{2.6}$$

and

$$\beta^2 - n_2^2k^2 = \gamma^2. \tag{2.7}$$

Note that

$$\alpha^2 + \gamma^2 = (n_1^2 - n_2^2)k^2 = NA^2k^2 \tag{2.8}$$

Equation (2.5) can then be written in the core and cladding separately as

$$\frac{d^2u}{dr^2} + \frac{1}{r}\frac{du}{dr} + (\alpha^2 - \frac{\ell^2}{r^2})u = 0, \qquad r \leqslant a \text{ (core)}, \tag{2.9}$$

$$\frac{d^2u}{dr^2} + \frac{1}{r}\frac{du}{dr} - (\gamma^2 + \frac{\ell^2}{r^2})u = 0, \qquad r \geqslant a \text{ (cladding)}. \tag{2.10}$$

Solutions for these equations are the Bessel functions [39]:

$$u(r) \propto \begin{cases} J_\ell(\alpha r), & r \leqslant a \text{ (core)}, \\ K_\ell(\gamma r), & r \geqslant a \text{ (cladding)}. \end{cases} \tag{2.11}$$

We introduce the normalized variables

$$X = \alpha a, \qquad Y = \gamma a, \tag{2.12}$$

with which Eq. (2.8) can be written as

$$X^2 + Y^2 = V^2, \tag{2.13}$$

where

$$V = 2\pi \frac{a}{\lambda} NA. \tag{2.14}$$

V is called the fiber parameter. The boundary conditions requires E_z and H_z to be continuous and to have a continuous derivative at the interface between the core and the cladding. These conditions apply to $u(r)$ in (2.11): $u(r)$ is continuous and has a continuous derivative at $r = a$, i.e.

$$J_\ell(X) = K_\ell(Y) \qquad X J'_\ell(X) = Y K'_\ell(Y). \tag{2.15}$$

This leads to the relation

$$\frac{(\alpha a) J'_\ell(\alpha a)}{J_\ell(\alpha a)} = \frac{(\gamma a) K'_\ell(\gamma a)}{K_\ell(\gamma a)}. \tag{2.16}$$

Due to the properties of the Bessel functions [39] and using relations (2.12), (2.16) can be written as

$$X \frac{J_{\ell\pm1}(X)}{J_\ell(X)} = \pm Y \frac{K_{\ell\pm1}(Y)}{K_\ell(Y)}. \tag{2.17}$$

Equation (2.17) can be solved graphically (see [35]). For every given values of ℓ and V, we have several solutions denoted $X_{\ell m}, m = 1, 2, ..., M_\ell$, each one defining a mode. If we choose the value of V sufficiently small, i.e. $V < 2.405$ [35], we get only the so called fundamental mode noted LP_{01} for linearly polarized light, $\ell = 0, m = 1$. The V parameter depends on the physical properties of the fiber (core radius a, refractive index n_1 and n_2), and on the wavelength λ (see Eq. (2.14)). Given a wavelength λ, we can choose a, n_1 and n_2 so that the fiber guides only the fundamental mode. Such fibers are called singlemode fibers.
From Eqs. (2.6) and (2.12) we get finally the propagation constant

$$\beta_{\ell m} = n_1^2 k^2 - \left(\frac{X_{\ell m}}{a} \right)^2. \tag{2.18}$$

And the radial solutions

$$u_{\ell m}(\rho) = \begin{cases} J_\ell(X_{\ell m}\, \rho), & \rho = \frac{r}{a} \leqslant 1 \text{ (core)}, \\ b_{\ell m} K_\ell(Y_{\ell m}\, \rho), & \rho = \frac{r}{a} \geqslant 1 \text{ (cladding)} \end{cases} \tag{2.19}$$

$$\text{with} \qquad b_{\ell m} = \frac{J_\ell(X_{\ell m})}{K_\ell(Y_{\ell m})}, \tag{2.20}$$

describe any (ℓ, m) mode $U_{\ell m}(r, \phi, z)$ propagating inside the fiber.
Nevertheless, such a description is cumbersome to work with, especially when one wants to compute coupling efficiencies (see section 2.3). It has been shown

[40, 41] that the transverse field distribution of the fundamental mode LP_{01} in a fiber can be approximated by a Gaussian profile

$$U = Ae^{-r^2/w^2}e^{-i\beta z}, \tag{2.21}$$

where w is the field radius. According to Marcuse [41], the approximation

$$w/a \approx 0.65 + 1.619V^{-3/2} + 2.879V^{-6}. \tag{2.22}$$

is accurate to within 1% for $1.2 < V < 2.4$ (telecommunication singlemode fibers are designed to operate in the range $2 < V < 2.4$). Figure 2.3 shows the LP_{01} mode for $V = 2.1$ and its approximated Gaussian profile (see Eq. (2.22)) with $a = 1.9$ μm. At the field radius w, the amplitude of the Gaussian profile drops by a factor$1/e$.

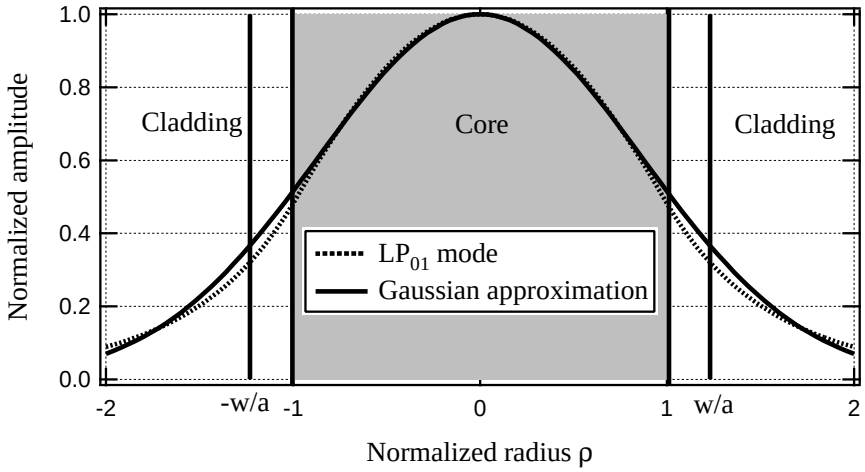

Figure 2.3: Normalized amplitude of the LP_{01} mode and its Gaussian approximation versus the normalized radius of the fiber $\rho = r/a$ for $V = 2.1$. $\rho = 1$ is the limit between the core and the cladding. The normalized Gaussian field radius is $w/a = 1.23$.

2.1.2 Gaussian beam propagation in free space

We will describe the properties and the parameters of a paraxial Gaussian beam propagating in free space. The complex amplitude $U(\vec{r})$ of a paraxial Gaussian beam is given by [35]

$$U(\vec{r}=(x,y,z)) = \frac{A_1}{q(z)} \exp\left[-ik\frac{\rho^2}{2q(z)}\right] e^{-ikz}, \tag{2.23}$$

where A_1 is a constant, $\rho^2 = x^2 + y^2$ is the distance from the axis of the Gaussian beam and z is the propagation direction of the Gaussian beam (see Fig. 2.4). We can separate amplitude and phase of the complex envelope by writing

$$\frac{1}{q(z)} = \frac{1}{R(z)} - i\frac{\lambda}{\pi w^2(z)}. \tag{2.24}$$

Introducing Eq. (2.24) in Eq. (2.23), we get

$$U(\vec{r}) = \underbrace{A_0\frac{w_0}{w(z)} \exp\left[-\frac{\rho^2}{w^2(z)}\right]}_{\text{amplitude factor}} \underbrace{\exp\left[-ik\frac{\rho^2}{2R(z)}\right]}_{\text{radial phase}} \underbrace{\exp\left[-ikz + i\,tan^{-1}\left(\frac{z}{z_r}\right)\right]}_{\text{longitudinal phase}}, \tag{2.25}$$

with

$$w(z) = w_0\sqrt{1+\left(\frac{z}{z_r}\right)^2} \tag{2.26}$$

$$R(z) = z\left[1+\left(\frac{z_r}{z}\right)^2\right] \tag{2.27}$$

$$w_0 = \sqrt{\frac{\lambda z_r}{\pi}} \tag{2.28}$$

$$z_r = \frac{\pi w_0^2}{\lambda}. \tag{2.29}$$

$w(z)$ is the beam radius, $R(z)$ the wavefront radius of curvature, w_0 the beam waist radius and z_r the Rayleigh range. Figure 2.4 shows some of these parameters. At the Rayleigh range z_r, the beam size $w(z_r) = \sqrt{2}w_0$ and $R(z)$ is minimal. Note that for $z \gg z_r$ the angular beam divergence is given by

$$\theta_0 = \lambda/\pi w_0. \tag{2.30}$$

The optical intensity $I(\vec{r}) = |U(\vec{r})|^2$ is given by

$$I(\rho,z) = I_0\left[\frac{w_0}{w(z)}\right]^2 \exp\left[-\frac{2\rho^2}{w^2(z)}\right], \tag{2.31}$$

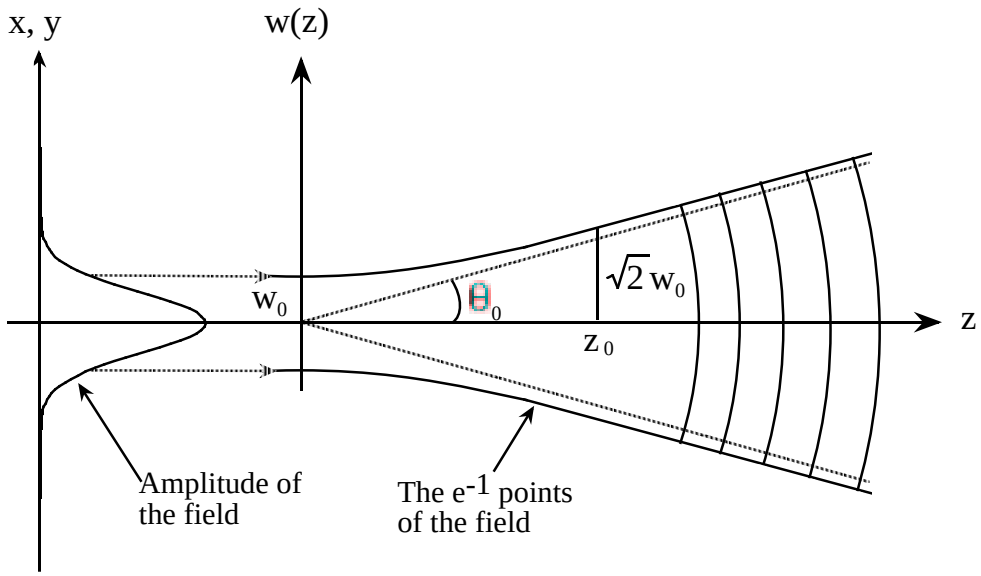

Figure 2.4: Gaussian beam parameters

where, $I_0 = |A_0|^2$. The total optical power carried by the beam is:

$$P = \int_0^\infty I(\rho, z) 2\pi\rho \, d\rho = \frac{1}{2} I_0 \pi w_0^2. \tag{2.32}$$

Finally, the ratio of the power carried within a circle of radius ρ_0 in the transverse plane at position z to the total power is

$$\frac{P_{\rho_0}(z)}{P} = \frac{1}{P} \int_0^{\rho_0} I(\rho, z) 2\pi\rho \, d\rho = 1 - \exp\left[-\frac{2\rho_0^2}{w^2(z)}\right]. \tag{2.33}$$

Considering the ratio $M = \rho_0/w(z)$, the power contained within a circle of radius $\rho_0 = w(z)$ is approximately 86% (the beam intensity drops by the factor $1/e^2 \approx 0.135$). About 99% of the power is contained within a circle of radius $\rho_0 = 1.5\ w(z)$.

2.1.3 Paraxial geometrical optics

In section 2.1.2, we have seen the main properties of a paraxial Gaussian beam propagating in free space and described by the complex amplitude given in Eq. (2.23). More generally, monochromatic light can be described by an amplitude and phase distribution

$$U(\vec{r}) = A(\vec{r}) e^{-ikS(\vec{r})}, \tag{2.34}$$

where $A(\vec{r})$ is the amplitude and $kS(\vec{r})$ is the phase of the wave. $S(\vec{r})$ is the Eikonal function and a wavefront is defined by

$$S(\vec{r}) = constant. \tag{2.35}$$

A ray is a trajectory that starts at any point on the wavefront and moves through space with the wave, always remaining perpendicular to the wavefronts.
In this section, we will describe the properties of paraxial rays in optical systems. A ray is completely described by two parameters: the ray position r and the ray slope r'. These two parameters are the elements of a ray-vector. Under paraxial approximation (rays travelling close to the optical axis and at small angles to that axis), the propagation of optical rays can be treated with a matrix formalism [42]. An optical system is characterized by a 2 x 2 ray-transfer matrix relating the position and inclination of the transmitted ray (r_2, r_2') to those of the incident ray (r_1, r_1'):

$$\begin{pmatrix} r_2 \\ r_2' \end{pmatrix} = \begin{pmatrix} A & B \\ C & D \end{pmatrix} \begin{pmatrix} r_1 \\ r_1' \end{pmatrix}. \tag{2.36}$$

For example, the ray-transfer matrix describing the propagation over a distance d through free space is

$$\begin{pmatrix} 1 & d \\ 0 & 1 \end{pmatrix}. \tag{2.37}$$

The passage through a thin lens with focal length f is described by the ray-transfer matrix

$$\begin{pmatrix} 1 & 0 \\ -1/f & 1 \end{pmatrix}. \tag{2.38}$$

2.1.4 Gaussian beam propagation through an optical system

Using the paraxial description of a Gaussian beam (see section 2.1.2) and the ray-matrix formalism introduced in section 2.1.3, we can describe the propagation of a paraxial Gaussian beam through an optical system by the $ABCD$ law introduced by Kogelnik [43]. Considering a matrix $\left(\begin{smallmatrix} A & B \\ C & D \end{smallmatrix}\right)$ describing an arbitrary optical system, the $ABCD$ law relates the q-parameters q_1 and q_2 of the incident and transmitted Gaussian beams at the input and output planes by [35]

$$q_2 = \frac{Aq_1 + B}{Cq_1 + D}. \tag{2.39}$$

Figure 2.5 shows three optical systems which couple light from a source fiber into a receiver fiber. We will investigate these systems using the $ABCD$ law. The LP_{01} modes of fibers are approximated by Gaussian beams (see section 2.1.1). The Gaussian beam of a fiber is characterized by the radius of curvature of the wavefront $R_0 = \infty$ and the beam waist w_0. Therefore, the q-parameter becomes

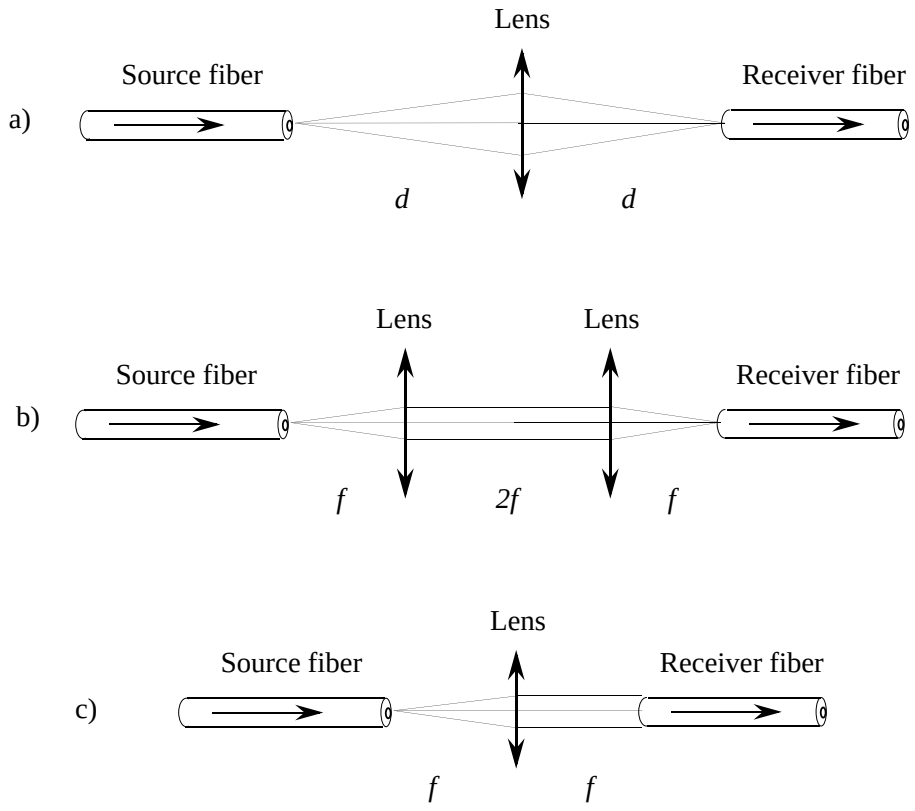

Figure 2.5: Three configurations for fiber coupling: a) single-lens 1 : 1 imaging, b) 4f system, c) Fourier transform. The drawn rays are geometrical rays (the diffraction of the Gaussian beam is not shown).

$q = q_0 = -iz_r = -i\pi w_0^2/\lambda$.
The 1 : 1 imaging system shown in Fig. 2.5 a) is described by the $\left(\begin{smallmatrix} A & B \\ C & D \end{smallmatrix}\right)$ matrix

$$\underbrace{\begin{pmatrix} 1 & d \\ 0 & 1 \end{pmatrix}}_{\text{free space 2f}} \underbrace{\begin{pmatrix} 1 & 0 \\ -1/f & 1 \end{pmatrix}}_{\text{lens}} \underbrace{\begin{pmatrix} 1 & d \\ 0 & 1 \end{pmatrix}}_{\text{free space 2f}} = \begin{pmatrix} 1-d/f & 2d-d^2/f \\ -1/f & 1-d/f \end{pmatrix}, \tag{2.40}$$

where f is the focal length of the lens. Using Eq. (2.39), we get

$$q_2 = \frac{(1-d/f)\,q_1 + 2d - d^2/f}{1 - q_1/f - d/f}. \tag{2.41}$$

With Eq. (2.24), Eq. (2.41) shows that the beam radius w and the radius of curvature R of the wavefront are conserved only if

$$f = \frac{d}{2} + \frac{z_r^2}{2d}. \tag{2.42}$$

Equation (2.42) is graphically represented in Fig. 2.6 for $z_r = 25.13$ μm ($\lambda = 633$ nm). For $d \gtrapprox 4z_r$, the beam radius w and the radius of curvature R are

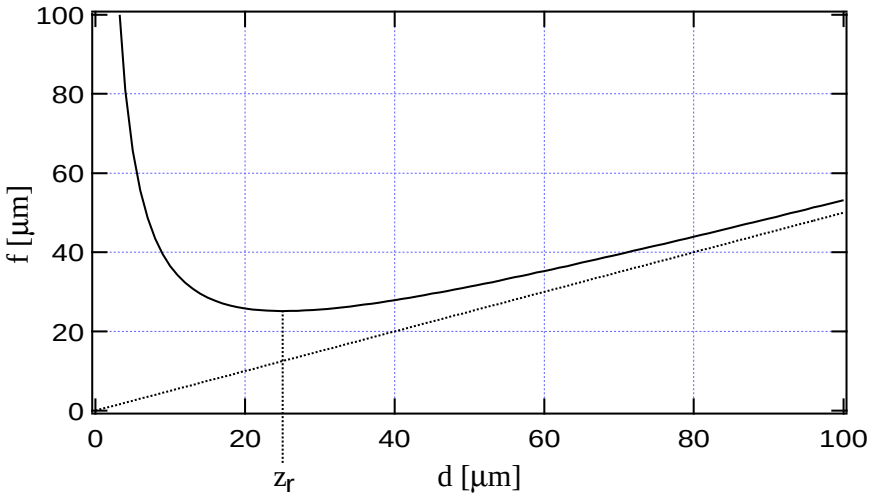

Figure 2.6: Solid line: focal length f versus the distance d in a $1:1$ imaging system for a perfect reproduction of w and R ($z_r = 25.13$ μm). Dotted line: $d = 2f$.

reproduced for $d \cong 2f$. For $f = d = z_r$ we are in the special case where the $1:1$ imaging system is a Fourier system.
The $1:1$ imaging system using two lenses ($4f$ system), as shown in Fig. 2.5 b), is described by the matrix

$$\underbrace{\begin{pmatrix} 1 & f \\ 0 & 1 \end{pmatrix}}_{\text{free space f}} \underbrace{\begin{pmatrix} 1 & 0 \\ -1/f & 1 \end{pmatrix}}_{\text{lens 2}} \underbrace{\begin{pmatrix} 1 & 2f \\ 0 & 1 \end{pmatrix}}_{\text{free space 2f}} \underbrace{\begin{pmatrix} 1 & 0 \\ -1/f & 1 \end{pmatrix}}_{\text{lens 1}} \underbrace{\begin{pmatrix} 1 & f \\ 0 & 1 \end{pmatrix}}_{\text{free space f}} = \begin{pmatrix} -1 & 0 \\ 0 & -1 \end{pmatrix}. \tag{2.43}$$

Using Eq. (2.39), we get $q_1 = q_2$. The q-parameter q_1 of the Gaussian beam at the source fiber is equal to the q-parameter q_2 of the Gaussian beam at the receiver fiber. This is the ideal case for coupling light from a source fiber into a receiver fiber.
Another system to be mentioned is the Fourier transform system shown in Fig. 2.5 c). The corresponding $ABCD$ matrix is

$$\underbrace{\begin{pmatrix} 1 & f \\ 0 & 1 \end{pmatrix}}_{\text{free space f}} \underbrace{\begin{pmatrix} 1 & 0 \\ -1/f & 1 \end{pmatrix}}_{\text{lens}} \underbrace{\begin{pmatrix} 1 & f \\ 0 & 1 \end{pmatrix}}_{\text{free space f}} = \begin{pmatrix} 0 & f \\ -1/f & 0 \end{pmatrix}. \tag{2.44}$$

Using Eq. (2.39), we get

$$q_1 q_2 = -f^2. \tag{2.45}$$

With Eq. (2.24), Eq. (2.45) gives

$$w_2 = \frac{\lambda f}{\pi w_1} \quad \text{and} \quad R_2 = R_1 = \infty. \tag{2.46}$$

The radius of curvature of the beam R is conserved, but not the beam radius w. The beam radius w is conserved only if

$$f = z_r. \tag{2.47}$$

2.2 Aberrations

In section 2.1.4, the propagation of a Gaussian beam through a paraxial system has been described. In order to replace the paraxial lenses by real lenses (with thickness and aberrations) in our system, non-paraxial ray tracing has to be introduced. In geometrical optics, light is assumed to consist of rays (see section 2.1.3). The chief ray is defined as the ray from an object point which passes through the center of the aperture stop and the center of both entrance and exit pupils (see Fig. 2.7). If rays emerging from the object point P are traced through the optical system up to the exit pupil such that each one travels an optical path length equal to that of the chief ray, the surface passing through their end points is called the system wavefront for the object point under consideration. If the wavefront is spherical, we say that the image is perfect; else, the image is aberrated. The deviations of the optical path length (i.e. geometric deviations times the refractive index n_i of the image space) of the wavefront from the reference sphere in the pupil plane are called wave aberrations W (see Fig. 2.7).

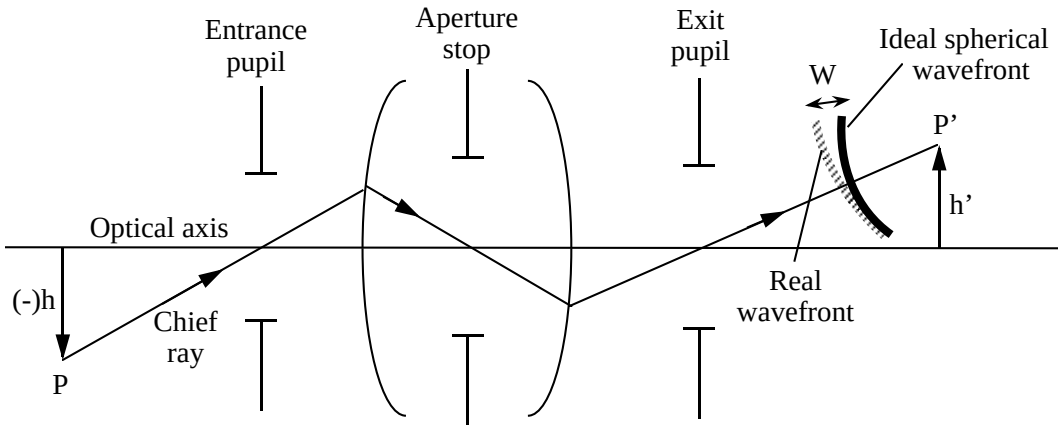

Figure 2.7: Schematic of an optical imaging system.

The object and the optical systems used in this work are all rotationally symmetric. In that case, the wave aberrations W depend on the object height h and pupil coordinates $\vec{r} = (r, \theta)$ through rotational invariants h^2, r^2 and $\vec{h} \cdot \vec{r}$ [44, 45]. A power-series expansion of the aberration function in terms of these invariants may be written in the form

$$W\left(\vec{h}, \vec{r}\right) = \sum_{l=0}^{\infty} \sum_{p=0}^{\infty} \sum_{m=0}^{\infty} C_{lpm} \left(h^2\right)^l \left(r^2\right)^p \left[hr \cos\theta\right]^m , \tag{2.48}$$

where C_{lpm} are the expansion coefficients and l, p, m, positive integers including zero. Equation (2.48) can also be written as

$$W(h, r, \theta) = \sum_{l=0}^{\infty} \sum_{n=1}^{\infty} \sum_{m=0}^{n} {}_{2l+m}a_{nm} h^{2l+m} r^n \cos^m \theta. \tag{2.49}$$

The degree of the expansion is even and given by $i = 2l + m + n$ also called the order of the aberration. Table 2.1 gives the principal aberration terms of orders 0,2,4 and 6. For a system that images a given object point, the explicit

i	Aberration name	Aberration term	Aberration order
0	piston	constant	zeroth order
2	tilt	$hr\cos\theta$	second
	defocus	r^2	order
4	primary astigmatism	$h^2r^2\cos^2\theta$	fourth order
	primary coma	$hr^3\cos\theta$	or
	primary spherical	r^4	primary
	primary defocus	h^2r^2	or
	primary tilt	$h^3r\cos\theta$	Seidel
6	secondary astigmatism	$h^2r^4\cos^2\theta$	
	secondary coma	$hr^5\cos\theta$	
	secondary spherical	r^6	sixth order
	lateral defocus	h^4r^2	or
	lateral tilt	$h^5r\cos\theta$	secondary
	pfeilfehler	$h^3r^3\cos^3\theta$	or
	lateral astigmatism	$h^4r^2\cos^2\theta$	Schwarzschild
	lateral coma	$h^3r^3\cos\theta$	
	lateral spherical	h^2r^4	

Table 2.1: Classification of wavefront aberrations.

dependance on the object height h can be included in the coefficient b_{nm} of the power-series expansion of the aberration function W so that

$$W(\rho, \theta) = \sum_{n01}^{\infty} \sum_{m=0}^{n} b_{nm} \rho^n \cos^m \theta, \tag{2.50}$$

where

$$b_{nm} = p^n \sum_{l=0}^{\infty} {}_{2l+m}a_{nm} h^{2l+m}, \tag{2.51}$$

and $\rho = r/p$ with is the radius p of the exit pupil of the system. An expansion similar to Eq. (2.50) is also possible using a complete set of Zernike circle

polynomials $R_n^m(\rho)\cos m\theta$, which are orthogonal over a unit circle, leading to

$$W(\rho,\theta) = \sum_{n=0}^{\infty}\sum_{m=0}^{n} c_{nm}\sqrt{\frac{2(n+1)}{1+\delta_{m0}}}R_n^m(\rho)\cos m\theta, \tag{2.52}$$

where c_{nm} are the Zernike coefficients and δ_{ij} is the Kronecker symbol. R_n^m are the radial functions

$$R_n^m(\rho) = \sum_{s=0}^{(n-m)/2} \frac{(-1)^s(n-s)!}{s!\left(\frac{n+m}{2}-s\right)!\left(\frac{n-m}{2}-s\right)!}\rho^{n-2s}. \tag{2.53}$$

The Zernike coefficients are then given by

$$c_{nm} = \frac{1}{\pi}\sqrt{2(n+1)(1+\delta_{m0})}\int_0^1\int_0^{2\pi} W(\rho,\theta)R_n^m(\rho)\cos m\theta\,\rho\,d\rho\,d\theta. \tag{2.54}$$

Each term of the Zernike-polynomial expansion refers to a Zernike aberration listed in Tab. 2.2 (for $n, m \leqslant 4$). Note that each Zernike aberration is made up of one or more classical aberrations listed in Tab. 2.1. The wavefront shapes

n	**m**	**Orthonormal Zernike Polynomial** $Z_n^m(\rho,\theta) = \sqrt{\frac{2(n+1)}{1+\delta_{m0}}}R_n^m(\rho)\cos m\theta$	**Aberration name**
0	0	1	piston
1	1	$\rho\cos\theta$	tilt
2	0	$\sqrt{3}(2\rho^2-1)$	defocus
2	2	$\sqrt{6}\rho^2\cos 2\theta$	primary astigmatism
3	1	$\sqrt{8}(3\rho^3-2\rho)\cos\theta$	primary coma
3	3	$\sqrt{8}\rho^3\cos 3\theta$	trifoil
4	0	$\sqrt{5}(6\rho^4-6\rho^2+1)$	primary spherical
4	2	$\sqrt{10}(4\rho^4-3\rho^2)\cos 2\theta$	secondary astigmatism
4	4	$\sqrt{10}\rho^4\cos 4\theta$	tetrafoil

Table 2.2: Orthonormal Zernike aberrations.

for some aberrations are shown in Fig. 2.8 [46, Fig. 8.2, p.258]. An interesting and useful point of the orthogonal-polynomial expansion of the aberration function in the form of Eq. (2.52) is that each aberration coefficient c_{nm} represents the standard deviation σ of the corresponding aberration term across the exit pupil. Computing the standard deviation of the aberration function $\sigma_{_W}$ is then

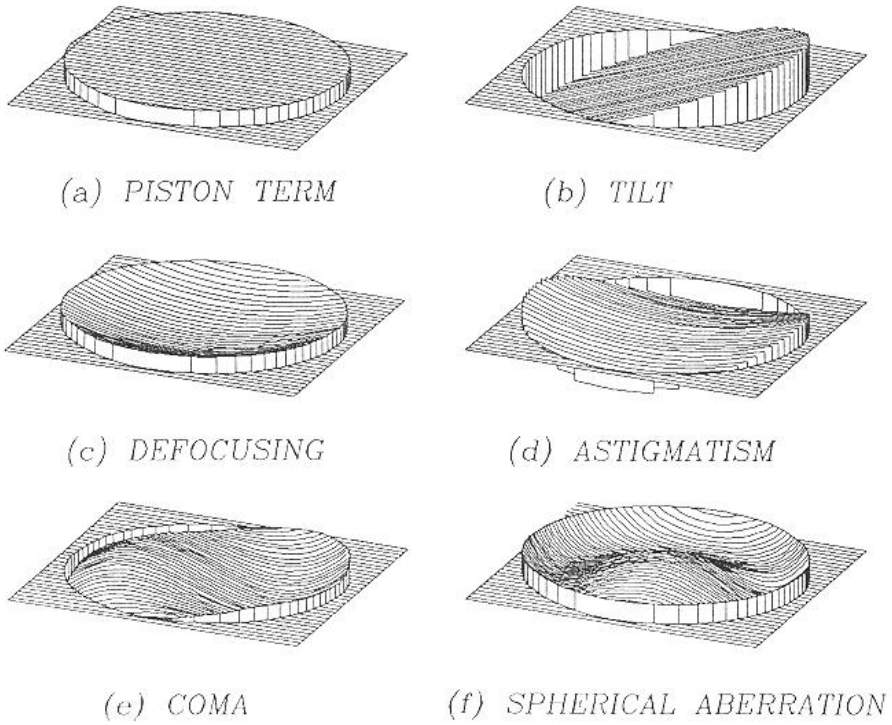

Figure 2.8: Wavefront shapes for the main aberrations. (from Malacara, [46, Fig. 8.2, p.258])

straightforward. Consider the mean value of the aberration function

$$< W(\rho,\theta) >= \frac{\int_0^1 \int_0^{2\pi} W(\rho,\theta)\rho\, d\rho\, d\theta}{\int_0^1 \int_0^{2\pi} \rho\, d\rho\, d\theta} = c_{00} \tag{2.55}$$

since $\int_0^{2\pi} \cos m\theta\, d\theta = 2\pi\delta_{m0}$. The mean square value of the aberration function is

$$< W^2(\rho,\theta) >= \frac{\int_0^1 \int_0^{2\pi} W^2(\rho,\theta)\rho\, d\rho\, d\theta}{\int_0^1 \int_0^{2\pi} \rho\, d\rho\, d\theta} = \sum_{n=0}^{\infty}\sum_{m=0}^{n} c_{nm}^2, \tag{2.56}$$

due to the orthogonality properties of the radial polynomials $R_n^m(\rho)$ and the angular $\cos m\theta$ functions. Hence, the variance of the aberration function is given

by

$$\sigma_W^2 =< W^2(\rho,\theta) > - < W(\rho,\theta) >^2 = \sum_{n=1}^{\infty}\sum_{m=0}^{n} c_{nm}^2. \tag{2.57}$$

Beside the standard deviation σ, the root-mean-square (rms) value

$$W_{rms} =< W^2 >^{1/2} \tag{2.58}$$

of the aberration is often referred in the literature. Finally, given the pupil function $P(x,y)$, the generalized pupil function is defined by

$$\mathcal{P}(x,y) = P(x,y)e^{ikW(x,y)}. \tag{2.59}$$

2.3 Coupling efficiency

In section 2.1, light propagation in the fiber and in free space have been introduced. It has been shown that the field distribution in the source plane, which is located at the end of the source fiber, can be approximated by a Gaussian profile (see Eq. (2.21)). In section 2.2 it has been shown how an optical system modifies the wavefront. In this section, we will describe the basic principles for computing a power-coupling efficiency.
Considering the source wave function ϕ, we compute the source efficiency

$$\eta_P = \frac{\iint\limits_{P(x,y)} \phi(x,y)\ \phi^*(x,y)\ dxdy}{\int\limits_{-\infty}^{\infty}\int\limits_{-\infty}^{\infty} \phi(x,y)\ \phi^*(x,y)\ dxdy}, \tag{2.60}$$

which is the normalized power collected by the entrance pupil of the optical system. The integral in the numerator is taken over the aperture of the system given by the pupil function $P(x,y)$. The * symbol represents the complex conjugate. Then, we compute the power-coupling efficiency

$$\eta = \frac{\left| \int\limits_{-\infty}^{\infty}\int\limits_{-\infty}^{\infty} \phi'(x,y)\ \psi^*(x,y)\ dxdy \right|^2}{\int\limits_{-\infty}^{\infty}\int\limits_{-\infty}^{\infty} \phi'(x,y)\ \phi'^*(x,y)\ dxdy \int\limits_{-\infty}^{\infty}\int\limits_{-\infty}^{\infty} \psi(x,y)\ \psi^*(x,y)\ dxdy}, \tag{2.61}$$

which is the normalized overlap integral of the incident wave function $\phi'(x,y)$ illuminating the receiver fiber and the modal wave function $\psi(x,y)$ of the receiver fiber. The wave function ϕ' is given by

$$\phi' = h \circ \phi, \tag{2.62}$$

where h is the impulse response or point-spread function (PSF) of the system, ϕ is the wave function of the source fiber and the $\circ$ symbol represents the convolution. The impulse response h is proportional to the Fourier transform of the generalized pupil function $\mathcal{P}(\xi,\zeta)$ [47]:

$$h \propto TF\{\mathcal{P}(\xi,\zeta)\}. \tag{2.63}$$

The generalized pupil function is defined by

$$\mathcal{P}(\xi,\zeta) = P(\xi,\zeta)e^{ikW(\xi,\zeta)}, \tag{2.64}$$

where $W(\xi, \zeta)$ is the function describing the aberrations (see section 2.2).
Finally, the total power coupling efficiency is

$$\eta_{tot} = \eta_P \eta. \tag{2.65}$$

In this chapter, we showed how light propagates through a singlemode optical fiber and how the LP_{01} mode can be approximated by a Gaussian beam. The properties of paraxial Gaussian beams propagating in free space and through an optical system have been given. Non-paraxial ray tracing has been introduced to consider the effects of real optical elements (with non zero thickness and aberrations). The description of the aberrations with Zernike polynomials has been detailed. Finally, the power coupling efficiency of an optical system, coupling light between a source fiber and a receiver fiber, has been described.
These tools will allow to investigate different optical switching systems in the next chapter.

Chapter 3

Optical fiber switch systems

In this chapter we investigate the optimum conditions and limitations of an optical switching system. The key parameters of the study are the power coupling efficiency, the number of possible interconnects, the system size and the tolerances. Several system configurations will be presented and evaluated. A complete description of the basic elements (including fabrication processes and tolerances) will be given.

3.1 General description

Figure 3.1 shows the general setup for a free space optical switching system. The

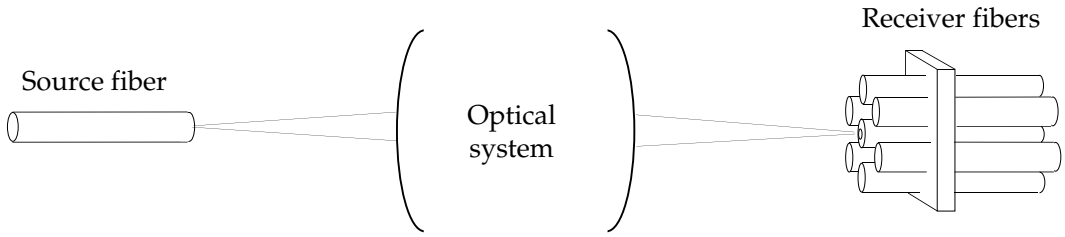

Figure 3.1: Schematic setup of the free space optical switching system.

optical system has two functions. First, it images a singlemode source fiber on a singlemode receiver fiber (coupling function). Second, it deflects the beam to address one of the receiver fibers (switching function). In sections 3.2, 3.3 and 3.4, the optical system will remain on axis (no switching). This configuration is a simple coupling optical system which allows to investigate for different optical systems (section 3.2) alignment tolerances (section 3.3) and the influence of a limited aperture (section 3.4). In section 3.5 we investigate further the coupling efficiency for systems with real optical elements, including aberrations. In the

first part the system is investigated on axis and in the second part the effect of switching is introduced.

3.2 Coupling losses for different systems

There are three different systems considered: the single-lens $1:1$ imaging system, the $4f$ system and the Fourier system (see Fig. 2.5). According to the calculations in section 2.1.2, the $4f$ system is the best as it conserves both the waist w and the radius of curvature R of the Gaussian beam. In this section, we will investigate quantitatively the coupling losses for the three systems. In order to estimate the power coupling efficiency, we use a system composed of a source fiber, a paraxial lens (perfect, without aberrations) and a receiver fiber (see Fig. 3.2).

The coupling efficiency for these three configurations can be calculated by the

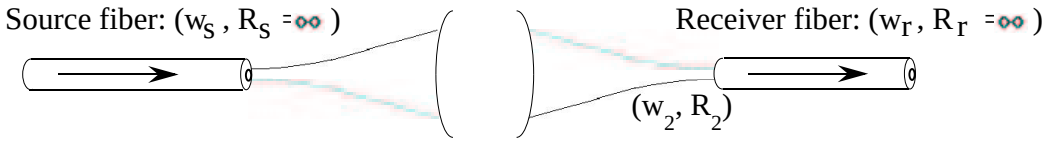

Figure 3.2: General setup of an optical system which couples light from a source fiber into a receiver fiber.

following approach. We consider the Gaussian profile approximation

$$G(x,y) = \exp\left[-\frac{x^2+y^2}{w^2}\right]\exp\left[-ik\frac{x^2+y^2}{2R}\right] \tag{3.1}$$

for both source and receiver fiber modes. Within the approximation of paraxial (geometrical) optics, the Gaussian beam parameters can be computed using $ABCD$ matrices (see section 2.1.4). With these assumptions, the power coupling efficiency between the source fiber and the receiver fiber can be calculated as the coupling efficiency between two Gaussian modes. The coupling efficiency η between the Gaussian wave function $\phi'(x,y)$ of the incoming Gaussian beam at the receiver fiber plane and the Gaussian mode $\psi(x,y)$ of the receiver fiber is given by Eq. 2.61. Let $\phi'(x,y)$ and $\psi(x,y)$ given by the complex amplitudes

$$\phi'(x,y) = \exp\left[-\frac{x^2+y^2}{w_2^2}\right]\exp\left[-ik\frac{x^2+y^2}{2R_2}\right] \qquad \text{and} \tag{3.2}$$

$$\psi(x,y) = \exp\left[-\frac{x^2+y^2}{w_r^2}\right], \tag{3.3}$$

with w_2 and R_2 the beam radius and the radius of curvature of the wave function of the incoming Gaussian beam at the receiver fiber plane, w_r the waist of the

Gaussian mode of the receiver fiber at the receiver fiber plane (see Fig. 3.2). Expressing the integral of Eq. (2.61) in polar coordinates we get

$$\eta = \frac{\left| \int_0^\infty e^{-\left[\frac{1}{w_2^2}+i\frac{k}{2R_2}\right]\rho^2} e^{-\frac{\rho^2}{w_r^2}} \rho \, d\rho \right|^2}{\int_0^\infty e^{-\left[\frac{1}{w_2^2}+i\frac{k}{2R_2}\right]\rho^2} e^{-\left[\frac{1}{w_2^2}-i\frac{k}{2R_2}\right]\rho^2} \rho \, d\rho \int_0^\infty e^{-2\frac{\rho^2}{w_r^2}} \rho \, d\rho}, \tag{3.4}$$

with $\rho^2 = x^2 + y^2$. For further numerical calculations, we will take identical singlemode source and receiver fibers ($w_s = w_r$) with $w_0 = 2.25$ μm at a wavelength of $\lambda = 633$ nm, corresponding to $z_r = \pi w_0^2/\lambda = 25.13$ μm. In comparison, $z_r = 57.73$ μm for $\lambda = 1.5$ μm.

3.2.1 Single-lens 1 : 1 imaging system

As shown in section 2.1.4, the single-lens 1 : 1 imaging system conserves the beam width w and the radius of curvature R of the beam only under the condition given by Eq. (2.42). If we consider the case where d is larger than $4z_r$, then Eq. (2.42) gives $d \cong 2f$. We have $w_2 = w_s$ and $R_2 = f$. Equation (3.4) becomes

$$\eta = \frac{\left| \int_0^\infty e^{-\left[\frac{2}{w^2}+i\frac{k}{2f}\right]\rho^2} \rho \, d\rho \right|^2}{\int_0^\infty e^{-\frac{2}{w^2}\rho^2} \rho \, d\rho \int_0^\infty e^{-\frac{2}{w^2}\rho^2} \rho \, d\rho} = \frac{1}{1+\left(\frac{kw^2}{4f}\right)^2} = \frac{1}{1+\left(\frac{z_r}{2f}\right)^2}. \tag{3.5}$$

$\eta(f/z_r)$ is graphically represented in Fig. 3.3. A focal length $f = z_r/2$ results in 3 dB insertion loss (50% coupling efficiency). Ideally (no backreflection), an efficiency $\eta \gtrsim 98\%$ is obtained with a focal length $f \gtrsim 4z_r$. In conclusion, the change of radius of curvature $R_2 \neq R_r$ of the Gaussian beam is uncritical for single-lens 1 : 1 imaging systems with a focal length $f \gtrsim 4z_r$.

3.2.2 Fourier transform system

As shown in section 2.1.4, the Fourier transform system conserves the radius of curvature R of the beam, but not the waist w. We have $R_2 = R_s = \infty$. Equation

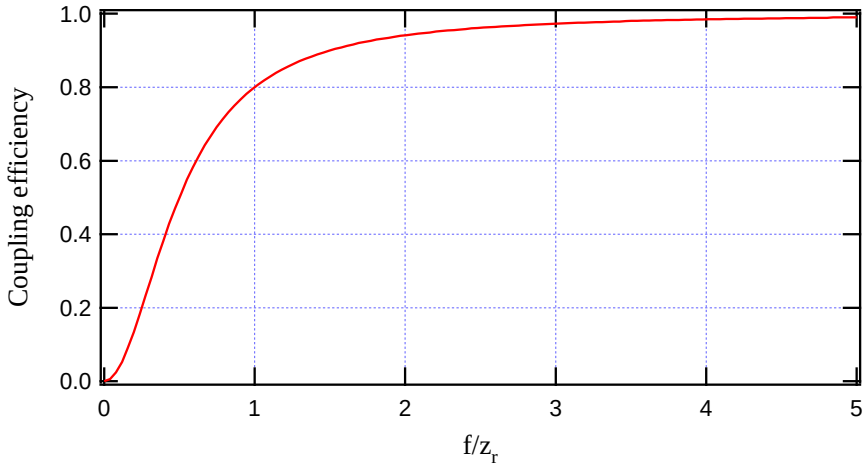

Figure 3.3: Coupling efficiency for the $1:1$ imaging system versus normalized focal length f/z_r.

(3.4) becomes

$$\eta = \frac{\left| \int_0^\infty e^{-\left(\frac{1}{w_2^2}+\frac{1}{w_r^2}\right)\rho^2} \rho \, d\rho \right|^2}{\int_0^\infty e^{-\frac{2}{w_2^2}\rho^2} \rho \, d\rho \int_0^\infty e^{-\frac{2}{w_r^2}\rho^2} \rho \, d\rho} = \frac{4 w_2^2 w_r^2}{\left(w_2^2 + w_r^2\right)^2} = \left(\frac{2 f/z_r}{1 + (f/z_r)^2} \right)^2 . \tag{3.6}$$

$\eta(f/z_r)$ is graphically represented in Fig. 3.4. A maximum coupling efficiency of $\eta = 1$ is reached when the waist is conserved ($w_2 = w_r$). This condition is fulfilled for $f = z_r$. Finally, the Fourier transform system has an efficiency higher than 50% only if $0.4 \lesssim f/z_r \lesssim 2.4$.

3.2.3 4f system

From the above calculations it is evident that the Fourier transform system is not adapted for optical fiber switches with a large number of interconnects. The single-lens $1:1$ imaging system is more appropriate. However, as shown in section 2.1.4, the $4f$ system conserves both the waist w and the radius of curvature R of the Gaussian beam. Moreover, the $4f$ system offers the possibility to insert mirrors in the collimated path. We have seen from Eq. (3.5) that the radius of curvature of the incoming Gaussian beam R_2 does not need to be exactly $R_r = \infty$ for a good coupling efficiency. For the $4f$ system, this has the consequence, that the collimated path does not need to be exactly $2f$ (see Fig. 2.5 b)). We will now investigate the consequences of a change of the distance between the two lenses

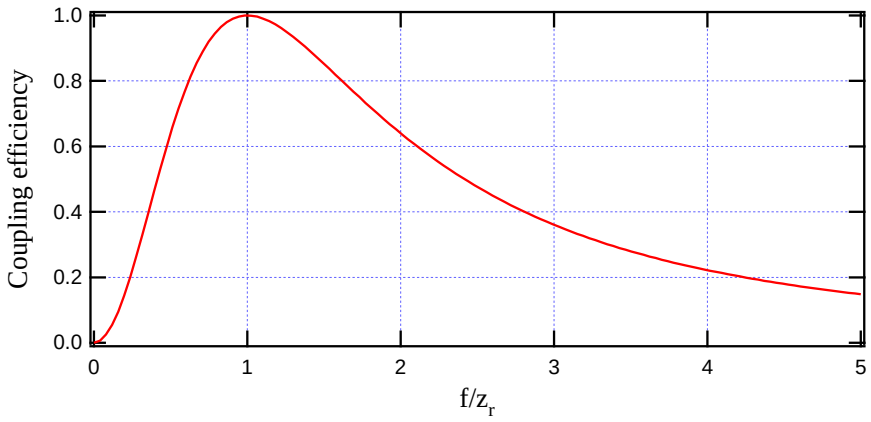

Figure 3.4: Coupling efficiency for the Fourier system versus normalized focal length f/z_r.

in a $4f$ system. A larger distance between the two lenses generates two effects. First, the beam size on the second lens will be larger due to the diffraction of the Gaussian beam between the two lenses. The diffraction angle is given by

$$\theta = \frac{w_s}{f}. \tag{3.7}$$

Therefore, this effect is more critical for small focal length. Second, the radius of curvature R_2 of the incoming Gaussian beam is not conserved anymore ($R_2 \neq R_s = \infty$). Let us consider a distance $2f + d$ between the two lenses. Using Eq. (2.43) and replacing $2f$ by $2f + d$, the $ABCD$ law (see Eq. (2.39) for the $4f$ system gives

$$R_2 = -\frac{f^2}{d}. \tag{3.8}$$

Equation 3.4 becomes

$$\eta = \frac{\left| \int_0^\infty e^{-\left[\frac{2}{w^2} - i\frac{kd}{2f^2}\right]\rho^2} \rho \, d\rho \right|^2}{\int_0^\infty e^{-\frac{2}{w^2}\rho^2} \rho \, d\rho \int_0^\infty e^{-\frac{2}{w^2}\rho^2} \rho \, d\rho} = \frac{1}{1 + \left(\frac{kdw^2}{4f^2}\right)^2} = \frac{1}{1 + \left(\frac{z_r d}{2f^2}\right)^2}. \tag{3.9}$$

$\eta(\frac{d}{f^2/z_r})$ is graphically represented in Fig. 3.5. A coupling efficiency higher than $\eta = 50\%$ is reached for

$$d \leqslant \frac{2f^2}{z_r}. \tag{3.10}$$

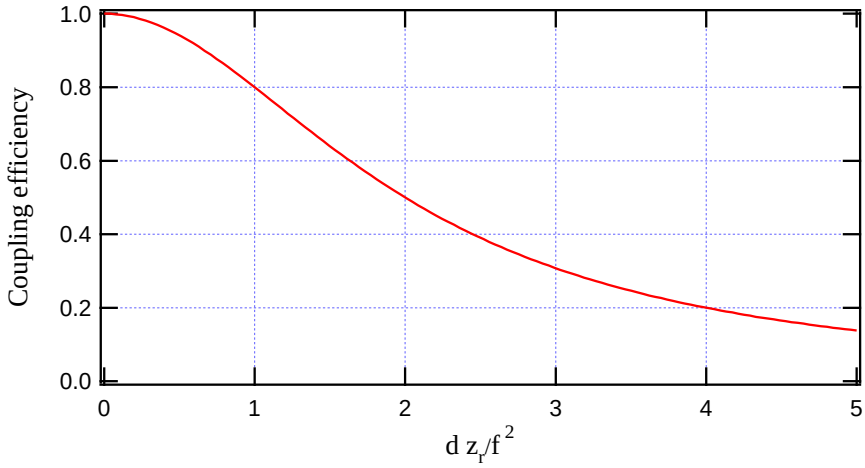

Figure 3.5: Coupling efficiency for the $4f$ system versus normalized distance $d\ z_r/f^2$ between the two lenses.

Numerically ($w_0 = 2.25\ \mu$m and $\lambda = 633$ nm $\Rightarrow z_r = 25.13\ \mu$m), Eq. (3.10) gives $d \lesssim 80\text{mm}^{-1} f^2$. This result shows that the distance between the two lenses in a $4f$ system is uncritical for focal lengths $f = 1$ mm or larger.

3.3 Alignment tolerances

The effect of fiber misalignment (lateral and longitudinal) and tilt (see Fig. 3.6) on the power coupling efficiency between one source fiber and one receiver fiber can be calculated using Eq. (2.61) [41]. The receiver fiber mode at the receiver

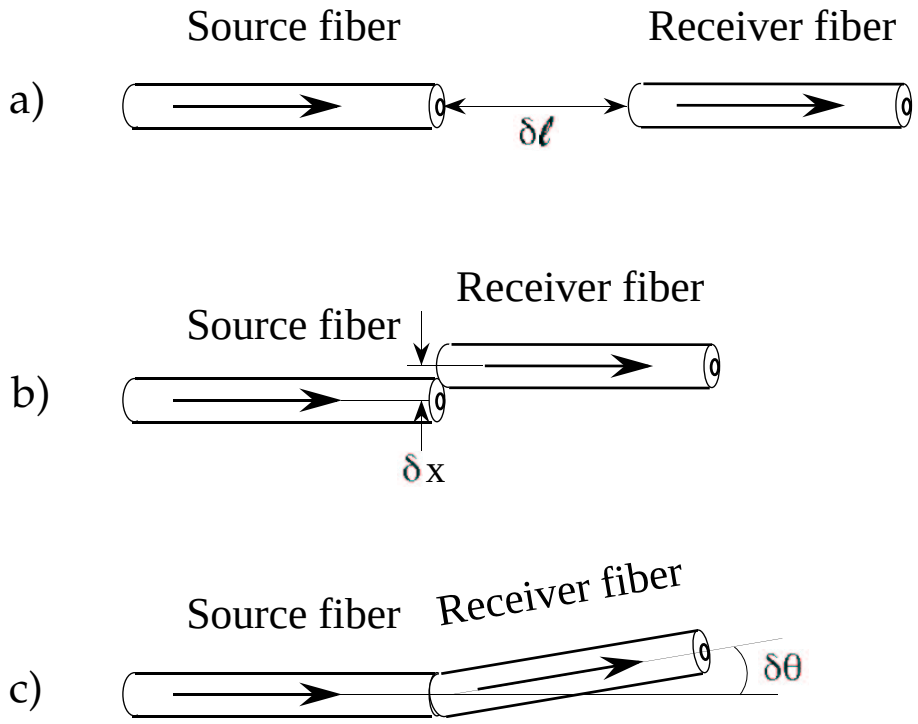

Figure 3.6: Misalignments for coupling light from a source fiber into a receiver fiber. a) longitudinal offset; b) lateral offset; c) tilt.

fiber plane is given by Eq. (3.3). For a longitudinal misalignment δl, the mode $\phi'_{\delta l}(x, y)$ at the receiver fiber plane becomes

$$\phi'_{\delta l}(x, y) = \exp\left[-\frac{x^2 + y^2}{w_2^2(\delta l)}\right], \tag{3.11}$$

with $w_2(\delta l)$ given by Eq. (2.26). The coupling efficiency between two identical fibers ($w_s = w_r = w$) is then given, using Eq. (2.61), by

$$\eta_{\delta l} = \frac{(\delta l / z_r)^2 + 1}{\frac{1}{4}(\delta l / z_r)^4 + (\delta l / z_r)^2 + 1}. \tag{3.12}$$

Figure 3.7 shows how the power coupling efficiency decreases with increasing fiber distance δl in terms of $z_r = \pi w^2/\lambda$ using Eq. (3.12). For $w = 2.25$ μm

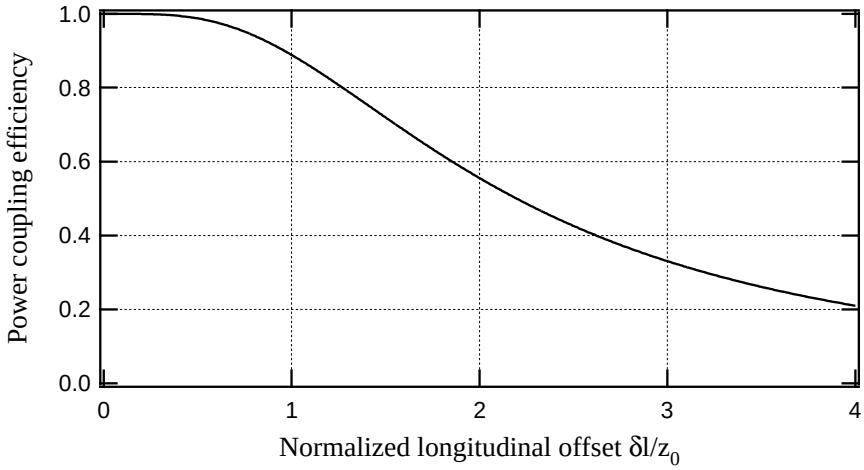

Figure 3.7: Power coupling efficiency between two identical singlemode fibers versus normalized longitudinal misalignment $\delta l/z_r$.

and $\lambda = 633$ nm ($z_r = 25.13$ μm), a longitudinal offset of 30 μm generates 1dB insertion loss (80% coupling efficiency).
For a lateral misalignment δx, the mode $\phi'_{\delta x}(x, y)$ becomes

$$\phi'_{\delta x}(x, y) = \exp\left[-\frac{(x + \delta x)^2 + y^2}{w_s^2}\right]. \tag{3.13}$$

The coupling efficiency between two identical fibers ($w_s = w_r = w$) is then given, using Eq. (2.61), by

$$\eta_{\delta x} = \exp\left(-\frac{\delta x^2}{w^2}\right). \tag{3.14}$$

Figure 3.8 shows how the power coupling efficiency decreases with increasing lateral offset δx between the two fibers using Eq. (3.14) in terms of the Gaussian beam width w. For $w = 2.25$ μm, a lateral offset of 1 μm generates 1dB insertion loss (80% coupling efficiency).

Finally, an angular misalignment $\delta\theta$ between two identical fibers ($w_s = w_r = w$), produces a linear phase change across the beam on the receiver fiber. The mode $\phi'_{\delta\theta}(x, y)$ can be described by

$$\phi'_{\delta\theta}(x, y) = \exp\left[-\frac{x^2 + y^2}{w_s^2}\right] \exp\left[x\frac{-2\pi i}{\lambda}\tan\delta\theta\right]. \tag{3.15}$$

Using Eq. (2.61), the coupling efficiency is given by

$$\eta_{\delta\theta} = \exp\left[-\left(\frac{\tan\delta\theta}{\theta_0}\right)^2\right] \cong \exp\left[-\left(\frac{\delta\theta}{\theta_0}\right)^2\right], \tag{3.16}$$

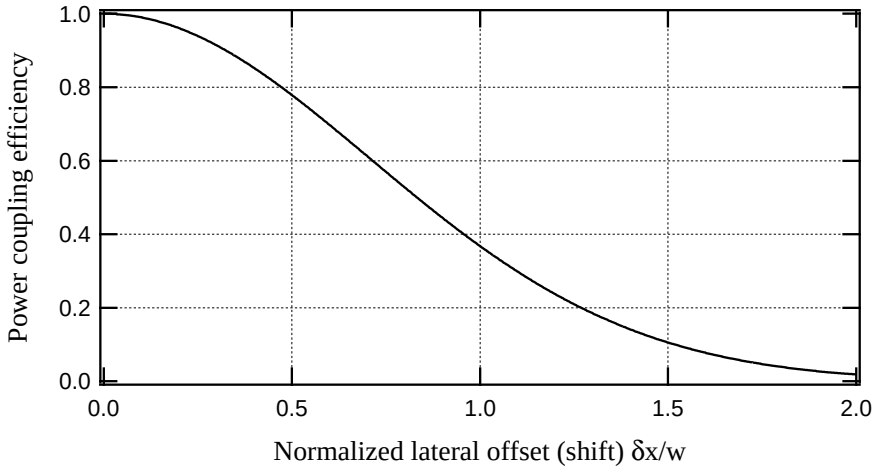

Figure 3.8: Power coupling efficiency between two identical singlemode fibers versus normalized lateral offset $\delta x/w$.

with $\theta_0 = \lambda/\pi w_0$, the angular divergence of the Gaussian beam. Figure 3.9 shows how the power coupling efficiency decreases with increasing angular misalignment between the two fibers $\delta\theta$ in terms of divergence $\theta_0 = \lambda/\pi w_0$ of the Gaussian beam using Eq. (3.16). For $w = 2.25$ μm and $\lambda = 633$ nm ($\theta_0 = 5.14°$), a tilt of 2.4°generates 1dB insertion loss (80% coupling efficiency).

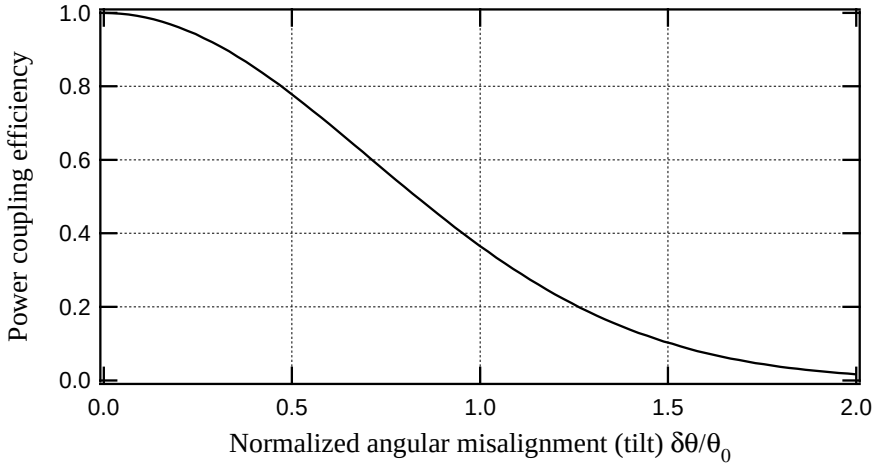

Figure 3.9: Power coupling efficiency versus normalized angular misalignment $\delta\theta/\theta_0$ between two identical singlemode fibers.

From the above calculations, we see that longitudinal alignment is less critical than lateral or angular alignment.

3.4 Aperture of the optical system

In a fiber coupling system, the effect of a stop, given by its radius r_{max}, has two effects. First, the stop will cut a part of the propagating beam (loss accounted in η_P, see section 2.3). Second, the aperture will cause an image broadening due to diffraction (the wave function ϕ' in Eq. (2.61) differs from the source wave function ϕ and the coupling efficiency η is reduced). The two effects are cumulative. In the following, we discuss the losses due to finite stops and we determine the ratios $r_{max}/w(z)$ needed to get an acceptable coupling efficiency.

Let us consider the simple case where the optical coupling system has a single lens with a stop of radius r_{max}. The total power coupling efficiency η_{tot} introduced in section 2.3 can be simplified and computed at the plane of the lens. Let $\phi(x, y)$ and $\psi(x, y)$ be the source and receiver fiber modes, respectively (see Eqs. (3.1) and (3.3)), the total power coupling efficiency expressed in polar coordinates is

$$\eta_{tot} = \frac{\left| \int_0^{r_{max}} e^{-2\frac{\rho^2}{w^2}} \rho \, d\rho \right|^2}{\int_{-\infty}^{\infty} e^{-2\frac{\rho^2}{w^2}} \rho \, d\rho \int_{-\infty}^{\infty} e^{-2\frac{\rho^2}{w^2}} \rho \, d\rho} = \left[1 - e^{-2\frac{r_{max}^2}{w^2}} \right]^2, \tag{3.17}$$

with $\rho^2 = x^2 + y^2$. As can be seen in Fig. 3.10, the coupling efficiency η is better than 98% for $r_{max}/w(z) \geqslant 1.5$. In terms of the numerical apertures of the optics (NA_{lens}) and of the source fiber (NA_{fiber}), this condition can also be expressed as $NA_{lens} \geqslant 1.5 NA_{fiber}$. This condition can be considered as a rule of thumb for any optical fiber switch.

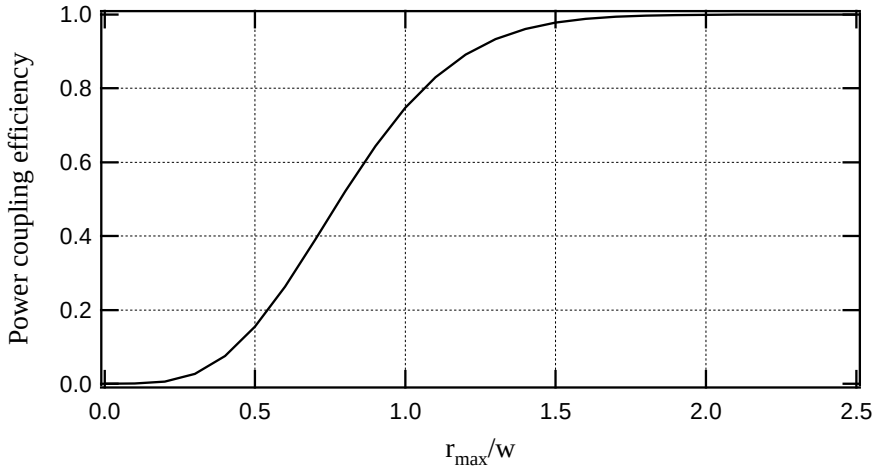

Figure 3.10: Effect of the aperture size on the coupling efficiency ($2r_{max}$ =diameter of the aperture, $2w$ =diameter of the Gaussian beam).

3.5 Simulations of the switching system

In this section, the $4f$ system is investigated in more detail. The aberrations of a real lens will play a central role. The characteristics of the lens will be discussed regarding their influence on the power coupling efficiency. These investigations were carried out using Zemax© simulations and the power coupling efficiency method described in section 2.3. An important part of this chapter is dedicated to the dependence of the aberrations on the optical system. Several system designs are numerically analyzed using different values for the aperture of the lens, the focal length, and the size of the system.

Calculations of the power coupling efficiency will be done based on the method described in section 2.3. The point spread function h is calculated by the ray tracing program Zemax©. The incident wave function ϕ' illuminating the receiver fiber is calculated using Eq. (2.62). The power coupling efficiency is then obtained by computing the normalized overlap integral of Eq. (2.61).

The real system is composed of a source fiber, a lens and a mirror. The source fiber is imaged ($4f$ system) onto one of the receiver fibers by moving the lens laterally as shown in Fig. 3.11. In this section, we use a flat mirror and investigate the aberrations of the system. In section 3.6, a deformable mirror will be introduced to correct some of these aberrations.

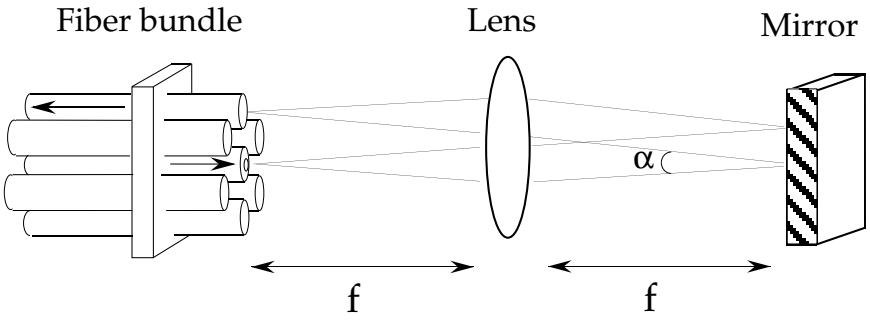

Figure 3.11: Schematic setup of the free space optical switching system.

The choice of the lens is important, since the lens is the main source of aberrations in the system. In principle, we could choose the optimum objective for one given connection. This would maximize the coupling efficiency for this connection. However, other connections, or a modification of the system (due to any external perturbation) would not be correct anymore.
For rotationally symmetric elements, only spherical aberration (see Tab. 2.1) can occur on axis (object height $h = 0$). The spherical aberrations are proportional to the power of 4 of the numerical aperture and proportional to the focal length

[48, 49]:

$$W_{sph} \sim NA^4 f. \tag{3.18}$$

It means that reducing the size of the lens will reduce the aberrations to the power of 4. It means also that reducing the focal length will decrease the aberrations proportionally. Note that it is not possible (due to fabrication limitations) to make the size of the lens arbitrarily small and keep the same focal length. It is also not possible to reduce the focal length below a certain limit, if we want to address a large number of receiver fibers and keep the deflection angles α relatively small (see Fig. 3.11).

3.5.1 Effect of aberrations for different lenses on-axis

In order to investigate the influence of the aberrations in our system, we simulate the $4f$ system using the ray tracing program Zemax©. Two values will be investigated: the standard deviation σ_W of the aberrations W (see Eq. (2.57)) and the power coupling efficiency. The aberrations are computed over the entire aperture of the optical system given by NA_{lens}.

3.5.1.1 Plano-convex lenses

First, we consider a plano-convex lens. As an example, a commercially available plano-convex lens made of BK7 ($n = 1.52$ at 633 nm) was chosen. Figure 3.12 shows the setup of the system with the plano-convex lens placed with its plane surface facing the fibers. Figure 3.13 shows the dependence of the standard

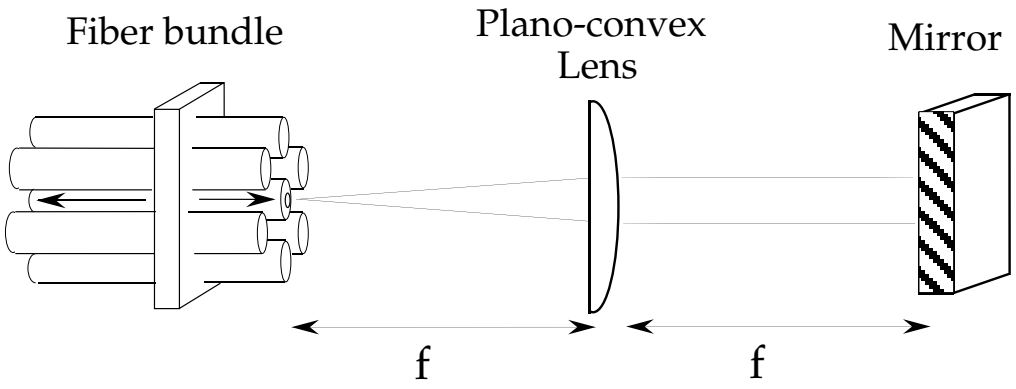

Figure 3.12: Setup of the free space optical switching system with a plano-convex lens.

deviation σ_W of the aberrations and the power coupling efficiency as a function of the focal length f of the plano-convex lens in the on-axis position. The numerical

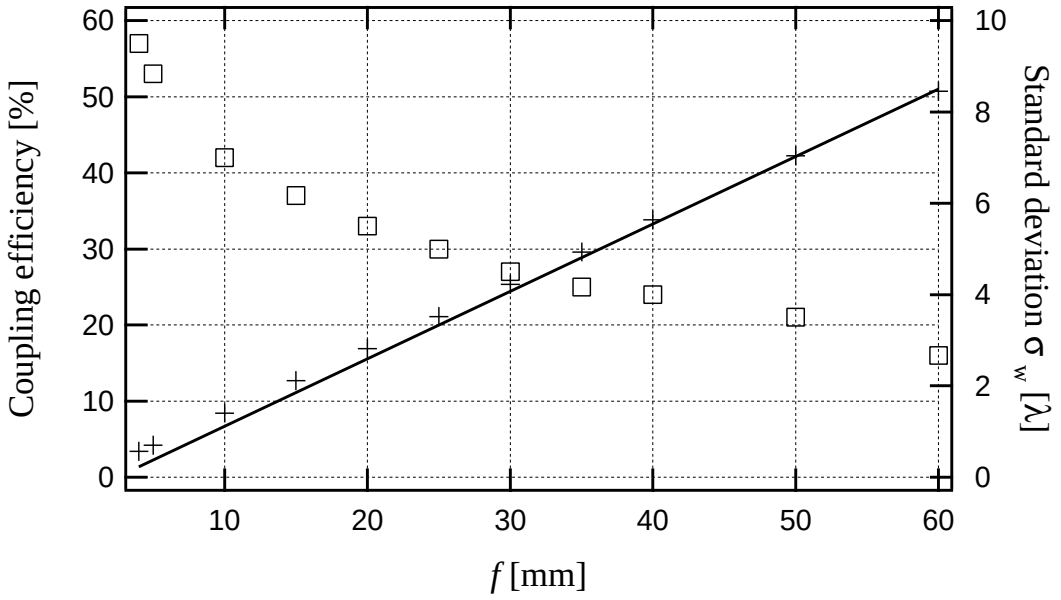

Figure 3.13: Power coupling efficiency (□) and standard deviation σ_W (+) of the aberration function W vs. focal length f of the plano-convex lens (BK7: $n = 1.52$ at 633 nm) with a numerical aperture $NA_{lens} = 0.17$.

aperture of the fibers is $NA_{fiber} = 0.11$ and the numerical aperture of the lens is chosen as $NA_{lens} = 1.5NA_{fiber} = 0.17$ to satisfy the criterion given in section 3.4. We see in Fig. 3.13 the linear dependence of the aberrations (standard deviation σ_W) with the focal length f as expected from Eq. (3.18). The smaller, the focal length, the smaller the aberrations and thus, the higher the power coupling efficiency. However, the efficiency here is quite poor, even for very small focal lengths. This is due to the aberrations which remain important, even for small focal length ($\sigma_W = 0.6$ for $f = 4$ mm). In order to have the maximum coupling efficiency, the system should be diffraction-limited. This means that the performance of the system is limited by the physical effects of diffraction rather than by the aberrations. Let us consider the *Strehl ratio* [50]

$$Strehl\ ratio \simeq 1 - \left(\frac{2\pi}{\lambda}\right)^2 \sigma_W^2 \cong \eta, \tag{3.19}$$

the illumination at the center of the airy disc for an aberrated system expressed as a fraction of the corresponding illumination for a perfect system. The Strehl ratio is a good approximation for the coupling efficiency η valid for small aberrations only. A diffraction limited system has a Strehl ratio of 1. A Strehl ratio of 0.8 corresponds to a peak to value wavefront error W of around $\lambda/4$ and to a standard deviation of $\sigma_W = 0.07\lambda$.

In Fig. 3.13 we see that a focal length $f = 6$ mm of the plano-convex lens corresponds to a coupling efficiency of 50% (3dB insertion loss). Such a focal length is however too small to address a large number of receiver fibers in a switching configuration (lens off-axis) while keeping the deflection angle α relatively small (see Fig. 3.11). The low values obtained for the coupling efficiency of the system using a plano-convex lens are even worse if the lens is placed with its curved surface facing the fibers. Effectively, placing the plano-convex lens with the curved surface facing the fibers make the rays undergo one large refraction instead of two small refractions. For a focal length $f = 40$ mm, $\sigma_{_W} = 5.6$ and the coupling efficiency is 23 % if the lens is placed with the flat surface facing the fibers, and $\sigma_{_W} = 22$ and the coupling efficiency is 10 % if the lens is placed with the curved surface facing the fibers.

3.5.1.2 Achromats

The use of an achromat instead of a plano-convex lens is a better choice in order to have small aberrations. The chosen achromat is a commercially available doublet (Linos # 322209, see Fig 3.14) made of SF2 (n=1.64 at 633 nm) and BK7 (n=1.52 at 633 nm). The refraction index is calculated using the Sellmeier dispersion formula [46]

$$n^2 - 1 = \frac{K_1\lambda^2}{\lambda^2 - L_1} + \frac{K_2\lambda^2}{\lambda^2 - L_2} + \frac{K_3\lambda^2}{\lambda^2 - L_3}, \tag{3.20}$$

with the coefficients for BK7 and SF2 listed in Tab. 3.1. Figure 3.15 shows

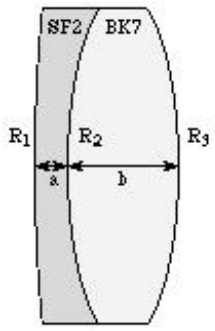

Figure 3.14: Schematic drawing of the achromat Linos # 322209. $f = 40$ mm, $a = 1.2$ mm, $b = 5.8$ mm, the refraction index $\mathrm{n}_{_{SF2}} = 1.64$ and $\mathrm{n}_{_{BK7}} = 1.52$ at 633 nm, $R_1 = 71.8$ mm, $R_2 = 17.5$ mm, $R_3 = -21.9$ mm.

the dependence of the standard deviation $\sigma_{_W}$ of the aberrations and the power coupling efficiency as a function of the focal length f of the scaled achromat. The numerical aperture of the lens is $NA_{lens} = 0.17$ and the numerical aperture of the fibers is $NA_{fiber} = 0.11$. We see again the linear dependence of the aberrations

Glass	BK7	SF2
$\mathbf{K}_1$	1.03961212	1.40301821
$\mathbf{L}_1$	$6.00069867 \cdot 10^{-3}$	$1.05795466 \cdot 10^{-2}$
$\mathbf{K}_2$	0.231792344	0.231767504
$\mathbf{L}_2$	$2.00179144 \cdot 10^{-2}$	$4.93226978 \cdot 10^{-2}$
$\mathbf{K}_3$	$1.03560653 \cdot 10^{2}$	0.939056586
$\mathbf{L}_3$	1.01046945	$1.12405955 \cdot 10^{2}$

Table 3.1: Sellmeier coefficients for BK7 and SF2.

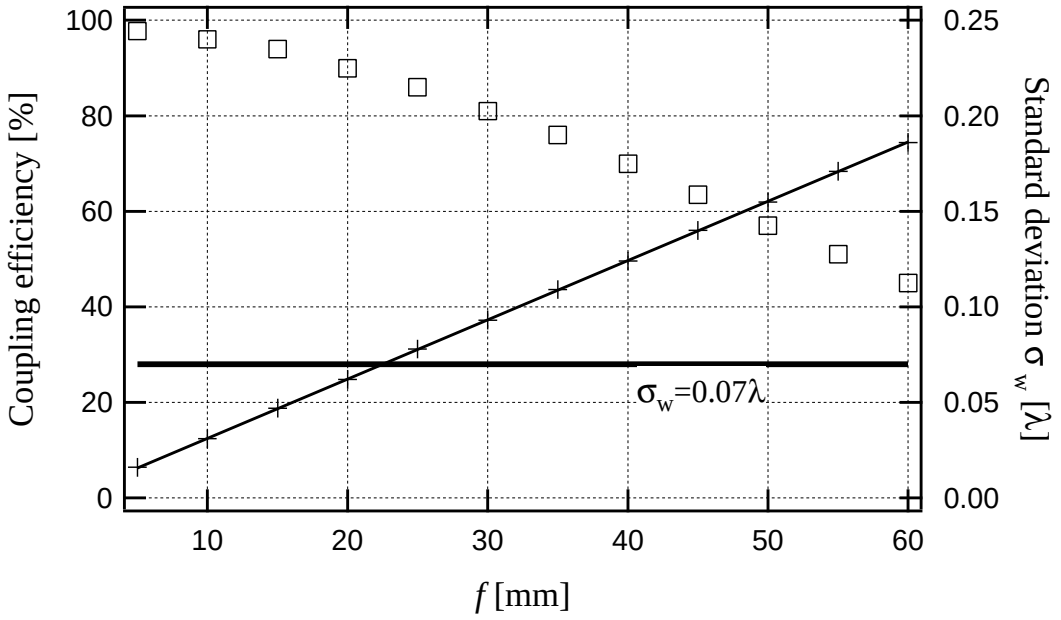

Figure 3.15: Power coupling efficiency (□) and standard deviation $\sigma_{_W}$ (+) of the aberration function W vs. focal length f of the achromat. The achromat is a doublet made of SF2 ($n = 1.64$ at 633 nm) and BK7 ($n = 1.52$ at 633 nm) and has a numerical aperture $NA_{lens} = 0.17$.

(standard deviation $\sigma_{_W}$) on the focal length f. The efficiency is here much higher than for a plano-convex lens; for a focal length $f \lesssim 30$ mm, the insertion loss is less than 1 dB (power coupling efficiency higher than 80%). Figure 3.16 shows the dependence of the standard deviation $\sigma_{_W}$ of the aberrations and the power coupling efficiency as a function of the numerical aperture NA_{lens} of the achromat. The focal length $f = 40$ mm and the numerical aperture of the fibers is $NA_{fiber} = 0.11$. For small NA_{lens}, the power coupling efficiency drops due to clipping effect. This effect begins to influence the power coupling efficiency as soon as $NA_{lens} \lesssim 1.5\ NA_{fiber}$ as already discussed in section 3.4. For large NA_{lens}, the increasing

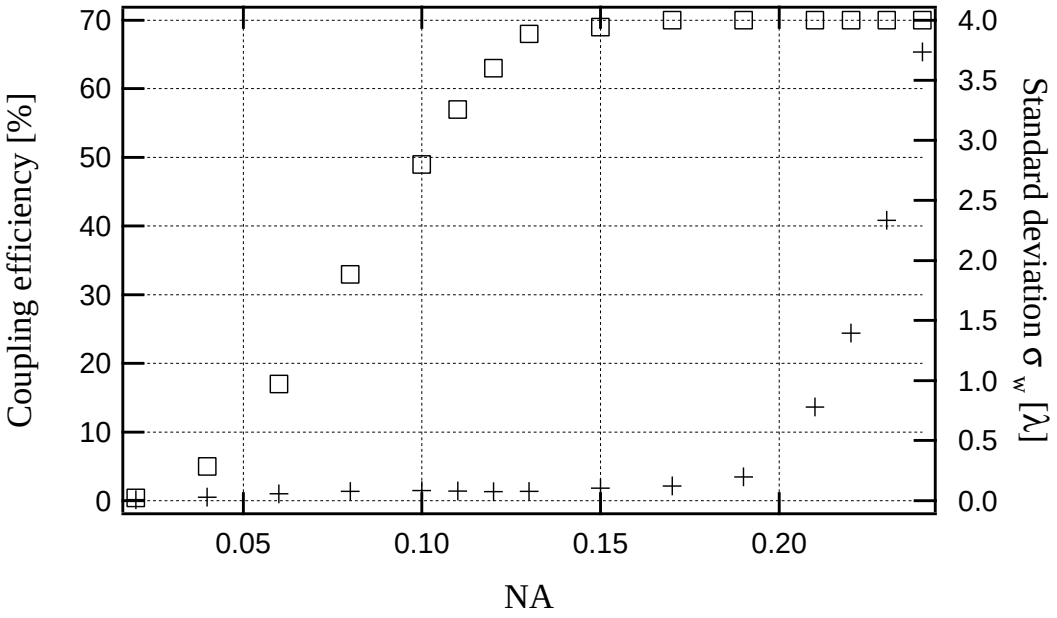

Figure 3.16: Power coupling efficiency (□) and standard deviation σ_W (+) of the aberration function W vs. numerical aperture NA_{lens} of the achromat. The achromat is a doublet made of SF2 ($n = 1.64$ at 633 nm) and BK7 ($n = 1.52$ at 633 nm) and has a focal length $f = 40$ mm.

aberrations of the lens have no influence on the power coupling efficiency, since most of the intensity is within the limit $NA_{lens} \lesssim 1.5\ NA_{fiber}$. The insertion loss approaches a limit of 1.5dB ($\eta = 70\%$).

3.5.2 Alignment tolerances for an achromat on-axis

The tolerances for longitudinal offset (Fig. 3.17), lateral offset (Fig. 3.18) and for angular misalignment (Fig. 3.19) of the receiver fiber with the achromat on-axis and the flat mirror are quite similar to those calculated for simple coupling between two fibers (see Figs. 3.7, 3.8 and 3.9 respectively). The lateral offset

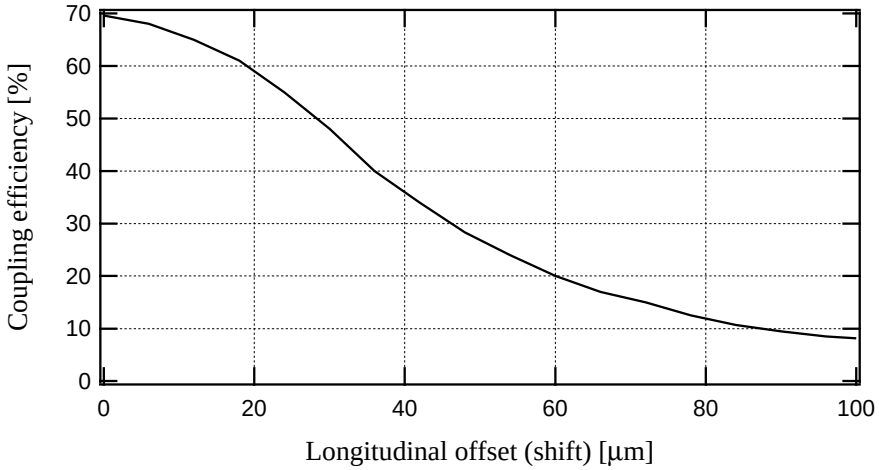

Figure 3.17: Power coupling efficiency for the $4f$ system with the achromat on axis versus longitudinal misalignment of the receiver fiber ($f = 40$ mm, $NA_{fiber} = 0.11$, $NA_{lens} = 0.17$).

of the receiver fiber can be corrected by displacing the achromat laterally or by adjusting the distance between the achromat and the flat mirror (see Fig. 3.11). If we consider 1 dB additional insertion loss (56% coupling efficiency in Fig. 3.18), the lateral tolerance on the receiver fiber is $\delta x = 1$ μm. Since the beam displacement on the receiver fiber is twice the lateral displacement of the lens, the corresponding tolerance for a lateral offset of the achromat is $\delta x/2 = 0.5$ μm.

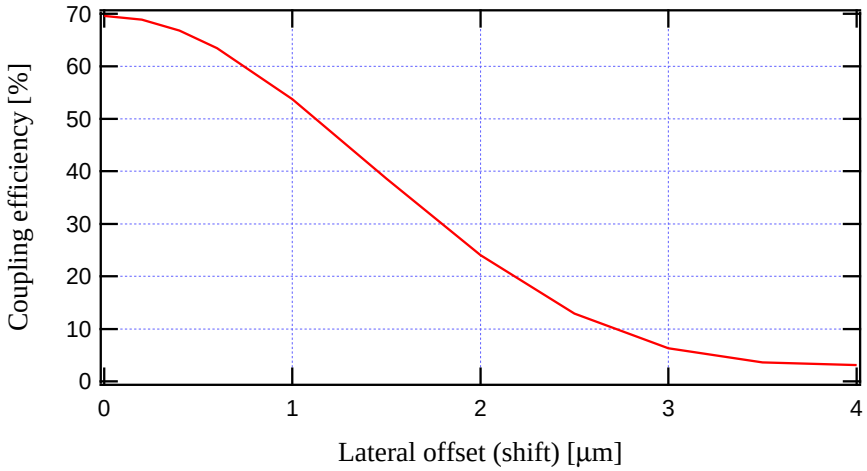

Figure 3.18: Power coupling efficiency for the $4f$ system with the achromat on-axis versus lateral misalignment of the receiver fiber ($f = 40$ mm, $NA_{fiber} = 0.11$, $NA_{lens} = 0.17$).

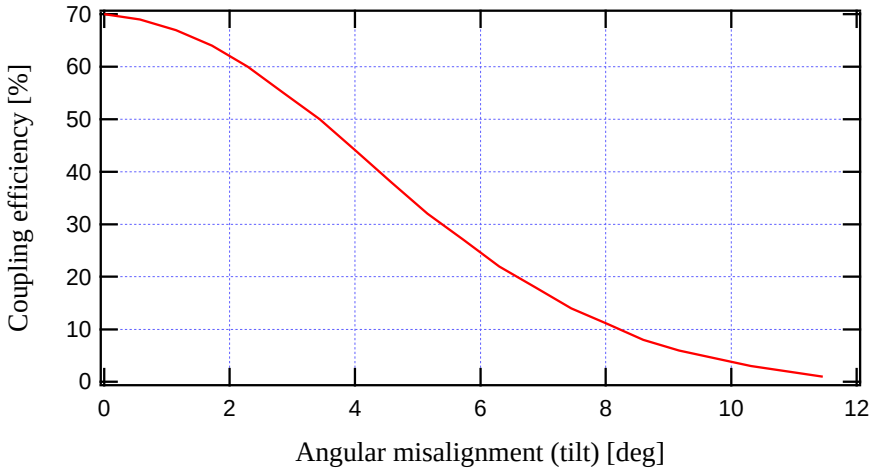

Figure 3.19: Power coupling efficiency for the $4f$ system with the achromat on-axis versus angular misalignment of the receiver fiber ($f = 40$ mm, $NA_{fiber} = 0.11$, $NA_{lens} = 0.17$).

3.5.3 Switching: achromat off axis

Placing the achromat off-axis as shown in Fig. 3.20 enables to connect the receiver fibers. Figure 3.21 shows the coupling efficiency for different switching configu-

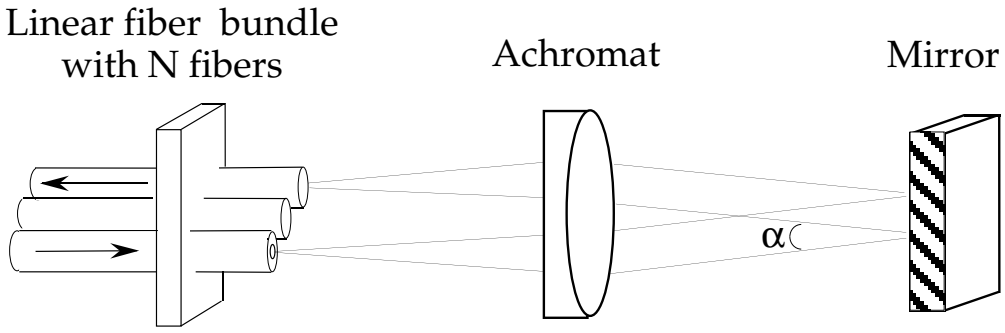

Figure 3.20: Setup of a 1-dimensional, 1 directional $4f$ system with one achromat and a flat mirror ($f = 40$ mm, $NA_{fiber} = 0.11$, $NA_{lens} = 0.17$).

rations using an achromat. The top solid line is for 1 to 1 coupling (source

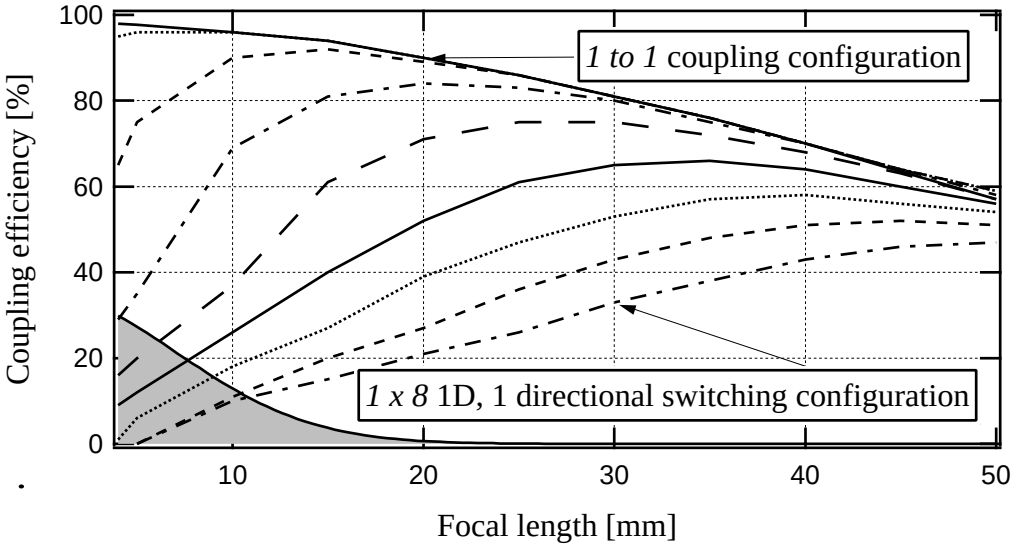

Figure 3.21: Coupling efficiency versus focal length for 1 to 1 coupling configuration, and, 1-dimensional, 1 directional switching configurations 1×1, 1×2, 1×3, 1×4, 1×5, 1×6, 1×7 and 1×8 ($NA_{fiber} = 0.11$, $NA_{lens} = 0.17$).

and receiver fiber are the same, achromat on-axis). The other lines are for 1-dimensional, 1 directional switching configurations 1×1, 1×2, 1×3, 1×4, 1×5, 1×6, 1×7 and 1×8 from second top to last bottom traces. For the

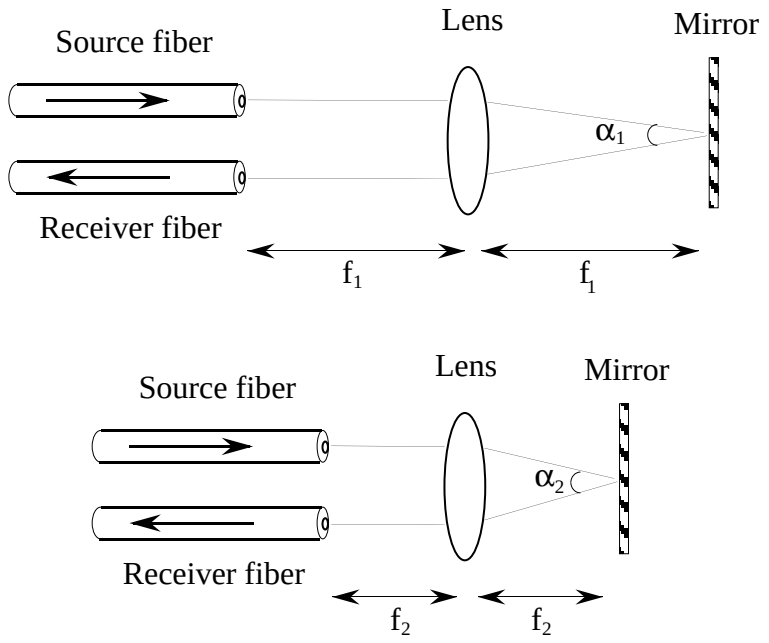

Figure 3.22: Geometry for the same switching configuration realized with lenses of different focal lengths f_1 and f_2.

1×1 switching configuration (receiver fiber next to source fiber), the achromat is shifted 0.125 mm off axis (half of the fibers pitch). For the 1×2 switching configuration, the achromat is shifted 0.250 mm off axis, etc...
Figure 3.21 shows that every switching configuration has a maximum coupling efficiency corresponding to a specific focal length (f_{max}). For example the 1×3, 1-dimensional, 1 directional configuration has a maximum coupling efficiency of 82 % at $f_{max} = 20$ mm. If $f > f_{max}$, the coupling efficiency decrease is a consequence of the increase of the aberrations with the focal length, described by Eq. (3.18) and shown in Fig. 3.15. If $f < f_{max}$, the coupling efficiency decreases due to the aberrations generated by the larger deflection angle α given by the off-axis position of the lens, as shown in Fig. 3.22. For a given focal length, addressing fibers further away from the center (for example 1×8) requires larger deflection angles, which generates larger aberrations. For small focal lengths ($f \lesssim 10$ mm) and for receiver fibers which are far away (left bottom grey zone in Fig. 3.21), the coupling efficiency is affected by a clipping effect. The lateral displacement of the lens is large compared to the diameter of the lens.
For a 2-dimensional, 2 directions system (bi-directional displacement of the achromat in the XY-plane), the receiver fibers are confined within a circle of radius corresponding to the number of receiver fibers of the 1-dimensional, 1 directional system (see Fig. 3.23). The 1-dimensional, 1 directional system with 8 switching configurations for example, corresponds to a 2-dimensional, 2 directions system

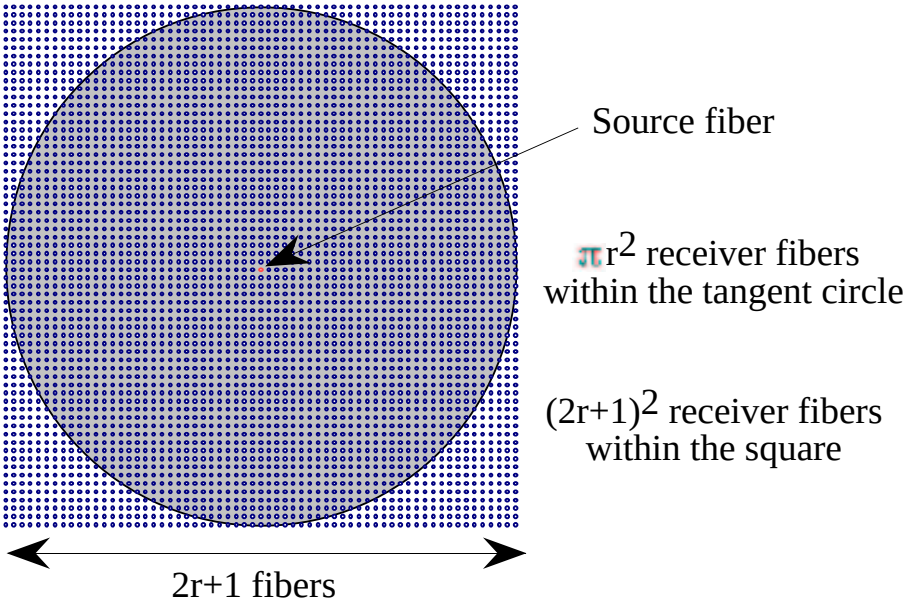

Figure 3.23: 2 dimensional arrangement of fibers. r is the number of receiver fibers for the corresponding 1-dimensional, 1 directional system.

with 201 switching configurations.

Figure 3.24 shows the coupling efficiency and the standard deviation σ_W of the aberrations as a function of the receiver fiber number (1-dimensional, 1 directional). The switching system is a 1-dimensional, 1 directional $4f$ system with an achromat and a flat mirror, as shown in Fig. 3.20, for $f = 40$ mm, $NA_{fiber} = 0.11$ and $NA_{lens} = 0.17$. Figure 3.24 shows that the coupling efficiency decreases rapidly as a function of the receiver fiber number, due to the increasing aberrations. The presented system would allow to switch between $2 \times 7 = 14$ fibers linearly or to $\pi 7^2 \cong 153$ fibers in two dimensions with insertion loss of less than 3dB ($\eta = 50\%$).

These results demonstrate that a correction of the aberrations is essential to address a large number of receiver fibers. In the following sections, we will present mainly two solutions to reduce the amount of aberrations. The first solution (sections 3.6 and 4.3) is to use a deformable mirror which can modify adaptively the wavefront in order to minimize the aberrations. The second solution (sections 3.7 and 4.4) uses another approach, which is to prevent large aberrations in the system by reducing the employed aperture of the achromat. Still another approach could be to use a specially designed holographic optical element (HOE) in order to minimize the aberrations for every configuration. Such an approach has been proposed and investigated [51] for holographic optical scanners.

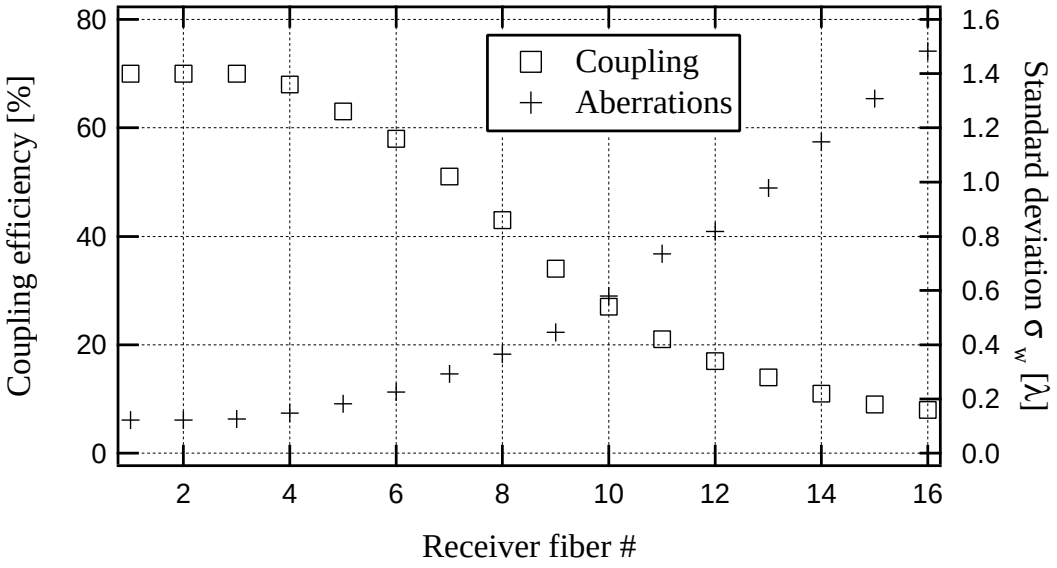

Figure 3.24: Coupling efficiency and standard deviation σ_W of the aberrations versus receiver fiber number for a 1-dimensional, 1 directional $4f$ system with an achromat and a flat mirror as shown in Fig. 3.20 ($f = 40$ mm, $NA_{fiber} = 0.11$, $NA_{lens} = 0.17$).

3.6 Correction of aberrations using a deformable mirror

In the preceding section, we have seen how the coupling efficiency is affected by the aberrations of the switching system between a source fiber and a large number of receiver fibers. In order to correct the aberrations, an adaptive optical element is needed. In theory, a perfect correction of the aberrations leads to a maximum coupling efficiency. This section is dedicated to the description of a micro-electro-mechanical deformable mirror (MEM-DM) used in place of the flat mirror in the $4f$ system (see Fig. 3.11). The deformable mirror allows to modulate the wavefront in order to optimize it for best coupling efficiency as will be shown experimentally in section 4.3.

Conventional adaptive mirrors are complex, large in size and expensive [52] (see for example ref. [53]). They are not suited for integration into a micro-electro-mechanical system. Recently, micro-electro-mechanical deformable mirrors (MEM-DM) have been developed using silicon micromachining. Three types of MEM-DM are currently being pursued: segmented mirrors [54], continuous face sheet mirrors backed by individual actuating elements [55] and microfabricated membrane mirrors [52]. The segmented mirrors have relatively low optical efficiency and diffraction effects. The continuous mirrors with individual actuating elements have a high optical efficiency and minimal diffraction effects, however, optimization of the influence function and interactuator coupling are critical for aberration corrections. The microfabricated membrane mirrors have high optical efficiency and allow several deformation modes of the membrane.

3.6.1 Physical properties of the membrane deformable mirror

The requirements for the adaptive mirror in the optical switching system, high optical efficiency and good potential for aberrations correction, are fulfilled by the microfabricated membrane mirror. The deformable membrane mirror used in this work was fabricated at TU-Delft [52]. Figure 3.25 shows a schematic view of the micromachined deformable mirror. The aluminum-coated silicon nitride membrane forms a thin, elastic, and electrically conducting film acting as a reflecting mirror surface, which is affixed to the supporting circular edge of the substrate. The electrostatic actuators are constructed with electrodes deposited on a ground plane, over which the mirror is attached. When voltages are applied between the electrodes and the mirror membrane, the electrostatic force pulls down the membrane, modulating the shape of the mirror surface. The desired mirror deflection can be achieved by application of appropriate voltages to the electrodes. The membrane's mechanical elasticity and the electrostatic forces

between the membrane surface and the control electrodes determine the deflection (i.e. the shape) of the mirror surface. Individually, each electrode channel modulates the whole surface profile of the mirror, whereas in combination all channels couple together to form the overall modulation of the mirror surface shape within the fixed boundary. The mirror is fabricated by bulk silicon mi-

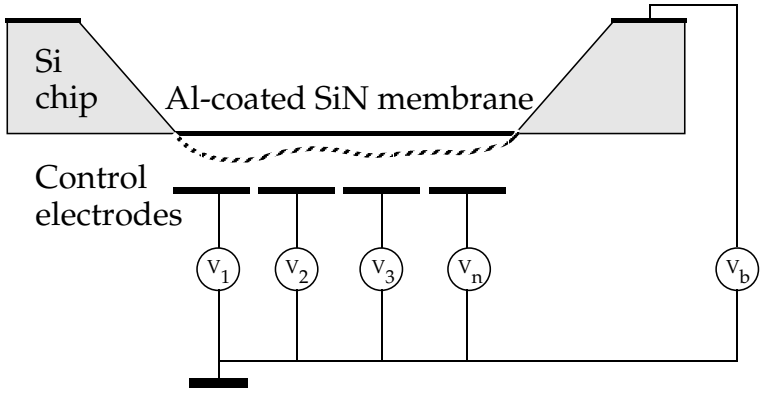

Figure 3.25: Schematic of the membrane micromachined deformable mirror.

cromachining [52]. The membrane has a diameter of 15 mm and is formed by low-stress low-pressure chemical-vapor deposited (LPCVD) silicon nitride with a thickness of 0.8 μm. The surface of the membrane is coated with a reflective aluminum layer. The distance between the membrane and the electrode structure is controlled by a dielectric spacer, supporting the membrane die. The 37 electrodes have a hexagonal structure and are formed in the metallization layer directly on the surface of a PCB holder. Figure 3.26 is a photograph of the membrane deformable mirror. The maximum deflection of the mirror center is 12 μm. The maximum applied control voltage is 190 V.

3.6.2 Control of the membrane MEM deformable mirror

As the membrane can only be deflected towards the electrodes, a bias voltage V_b (see Fig. 3.25) is applied to the membrane to achieve bidirectional movement. With the bias voltage $V_b = 130\ V$ and all control voltages $V_1, ..., V_n$ equal to zero, the membrane will take on a parabolic shape with a maximum deflection of 6 μm. The deflection $U(x, y)$ of the stretched membrane under an external load $P(x, y)$ is given by the Poisson equation [56]:

$$\Delta U(x, y) = \frac{-P(x, y)}{T}. \tag{3.21}$$

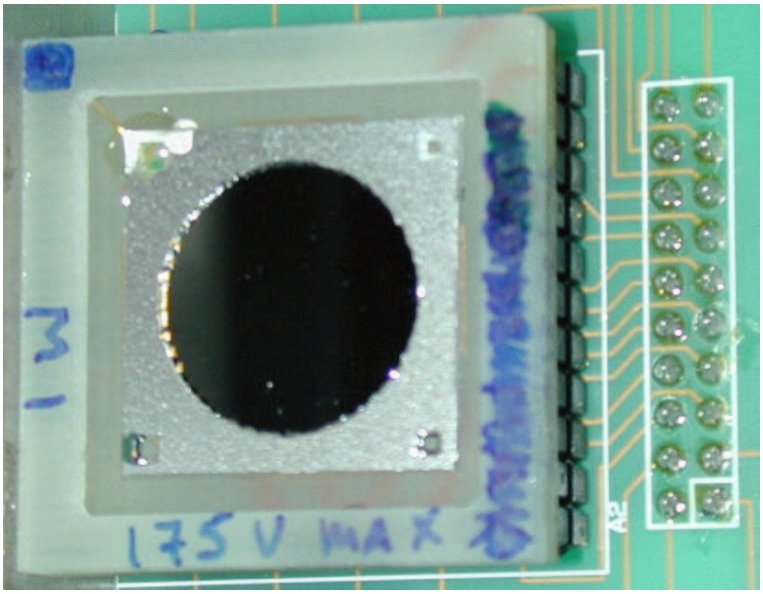

Figure 3.26: Photograph of the deformable mirror.

$P(x, y)$ is

$$P(x, y) = \frac{\epsilon\epsilon_0 V^2(x, y)}{d^2(x, y)}, \tag{3.22}$$

for the case of electrostatic actuation [57], with the dielectric constants ϵ and ϵ_0, the electrical potential distribution of the actuator structure $V(x, y)$ and the distance between the membrane and the actuator structure $d(x, y)$. The mechanical membrane tension is [57]

$$T = \frac{Eh\delta^2}{2(1-\nu)}, \tag{3.23}$$

where E is the Young's modulus of the membrane material, h is the thickness of the membrane, ν is the Poisson ratio of the membrane material, and δ is the in-plane membrane elongation due to stretching. A finite-element model of the membrane deflection has been realized by the Imperial College of Science Technology and Medicine, London [58] to solve numerically the Poisson equation (3.21). It gives a relation between the applied voltage on the 37 electrodes and the generated shape of the membrane. The shape of the membrane is described using orthonormal Zernike circle polynomials (see section 2.2). Each term of the Zernike polynomial corresponds to a deformation mode of the membrane. It makes possible the representation of the deformation of the membrane in a superposition of orthogonal modes. This is particularly interesting as the deformation modes of the membrane relate to the respective aberrations types. Table 3.2 lists the first 20 deformation modes of the membrane.

Mode	Orthonormal Zernike Polynomial	Aberration name
1	1	piston
2	$2\rho\sin\theta$	primary tilt Y
3	$2\rho\cos\theta$	primary tilt X
4	$\sqrt{6}\rho^2\sin 2\theta$	primary astigmatism 45°
5	$\sqrt{3}(2\rho^2-1)$	primary defocus
6	$\sqrt{6}\rho^2\cos 2\theta$	primary astigmatism 0°
7	$2\sqrt{2}\rho^3\sin 3\theta$	trifoil 30°
8	$2\sqrt{2}(3\rho^3-2\rho)\sin\theta$	primary coma Y
9	$2\sqrt{2}(3\rho^3-2\rho)\cos\theta$	primary coma X
10	$2\sqrt{2}\rho^3\cos 3\theta$	trifoil 0°
11	$\sqrt{10}\rho^4\sin 4\theta$	tetrafoil 22.5°
12	$\sqrt{10}(4\rho^4-3\rho^2)\sin 2\theta$	secondary astigmatism 45°
13	$\sqrt{5}(6\rho^4-6\rho^2+1)$	primary spherical
14	$\sqrt{10}(4\rho^4-3\rho^2)\cos 2\theta$	secondary astigmatism 0°
15	$\sqrt{10}\rho^4\cos 4\theta$	tetrafoil 0°
16	$2\sqrt{3}\rho^5\sin 5\theta$	
17	$2\sqrt{3}(5\rho^5-4\rho^3)\sin 3\theta$	
18	$2\sqrt{3}(10\rho^5-12\rho^3+3\rho)\sin\theta$	secondary coma Y
19	$2\sqrt{3}(10\rho^5-12\rho^3+3\rho)\cos\theta$	secondary coma X
20	$2\sqrt{3}(5\rho^5-4\rho^3)\cos 3\theta$	

Table 3.2: Deformation modes of the mirror and the equivalent orthonormal Zernike polynomials.

3.6.3 Measured characteristics of the membrane MEM deformable mirror

Figure 3.27 shows the measured interferograms of the membrane mirror first for the mirror at rest and for the biased mirror, and then for the first 20 modes (in both push and pull deformation). We see that the membrane at rest is not perfectly plane. The deviation from the plane is an astigmatism of around 3 to 4λ. This is a very large aberration (an astigmatism of $\lambda/5$ reduces the coupling efficiency to 50% in our switching system). The astigmatism is due to residual stress in the membrane. This inherent astigmatism will generate an offset for each deformation mode.

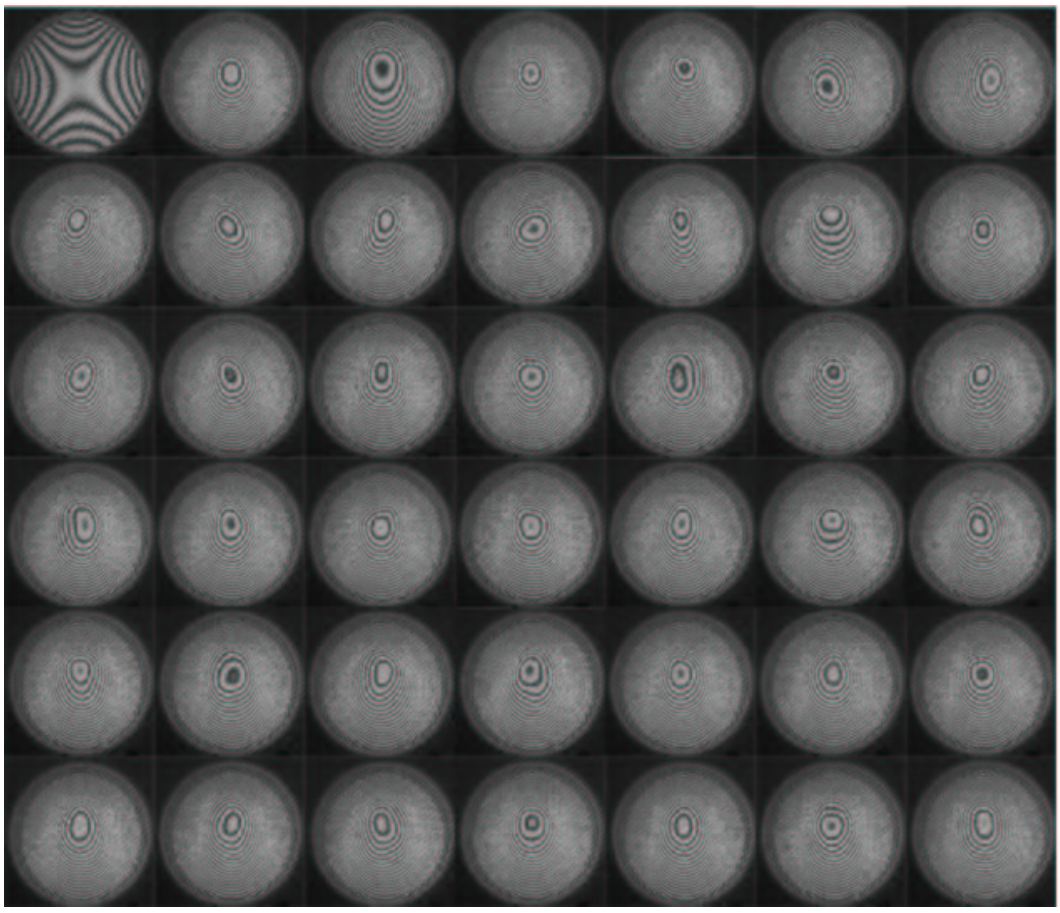

Figure 3.27: Interferograms of the membrane mirror. Membrane at rest (top left). Membrane under biased voltage (2nd left top). From 3rd left top to last: 20 first deformation modes (push and pull) according to Tab. 3.2.

3.7 Reducing the system aberrations with microlenses

In section 3.5 the dependance of the aberrations as a function of the numerical aperture NA of the lens has been shown. Larger NA yield larger standard deviations of the aberrations and consequently lower coupling efficiencies. Figure 3.28 shows the optical path difference W (referenced to the chief ray) for the 1 to 1 coupling configuration of the $4f$ system with an achromat on-axis for a focal length $f = 40$ mm and a numerical aperture $NA = 0.17$.
Reducing the numerical aperture by taking only small parts of the lens would reduce the system aberrations.

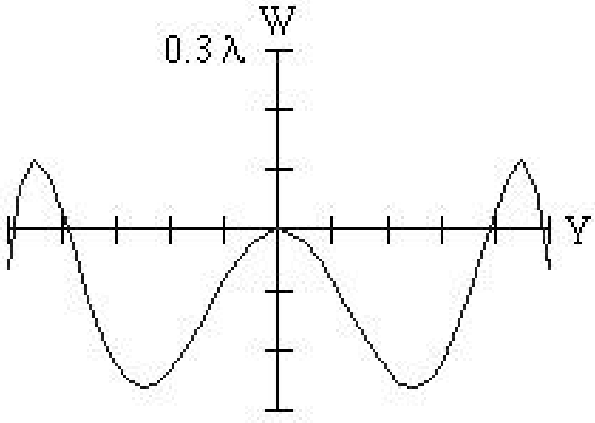

Figure 3.28: Optical path difference for the 1 to 1 coupling configuration of the $4f$ system with an achromat on axis versus normalized exit pupil coordinate Y ($f = 40$ mm and $NA = 0.17$).

3.7.1 Free space switching system with microlenses

In order to reduce the numerical aperture, we propose to place microlenses on-axis in front of every fiber. Figure 3.29 shows the setup of the proposed system. The switching is realized by laterally displacing the achromat. We chose a system with a microlens of diameter $\phi = 245$ μm and $f_{ml} \cong 660$ μm to collimate the Gaussian beam from the source fiber and an achromat of $f = 40$ mm to deflect the light. For fibers with $NA_{fiber} = 0.11$, the effective aperture of the achromat has a diameter of $0.22 f_{ml} = 145$ μm, which is only 0.8% of the total aperture diameter of the achromat. The beam is focused onto the receiver fibers with identical microlenses. The coupling efficiency has been calculated with the ray tracing program Zemax©, as described in section 2.3. For singlemode fibers with $NA_{fiber} = 0.11$, a coupling efficiency of 98% (0.1 dB insertion loss) was found

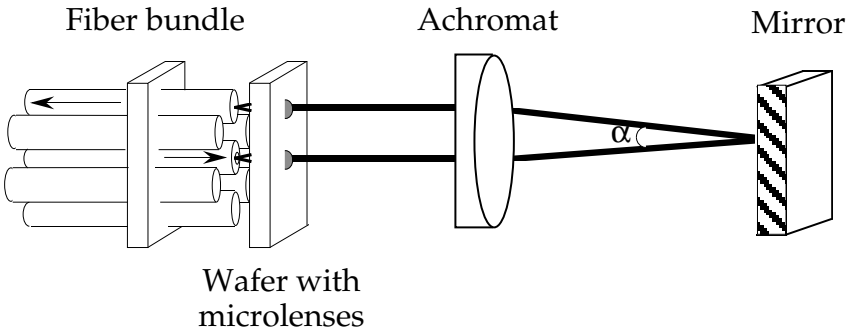

Figure 3.29: Schematic setup of the free space switching system using microlenses to reduce the numerical aperture and an achromat to switch from the source fiber to the receiver fibers.

for the 1 to 1 coupling configuration (source and receiver fiber is the same fiber, achromat on-axis). The same coupling efficiency is obtained for switching configurations up to the deflection limit, where the beam is passing just at the edge of the achromat.

3.7.2 Alignment tolerances of the free space switching optical system with microlenses

The tolerances for lateral and angular misalignment of the receiver fiber, shown in Fig. 3.30 b) and c), are quite the same as the tolerances for the system without microlenses (Figs. 3.18 and 3.19, respectively), whereas, the tolerance for longitudinal misalignment shown in Fig. 3.30 a) is more critical than for the system without microlenses (Fig. 3.17).

The alignment of the microlens array with respect to the fiber array is an additional degree of freedom. However, if the array of microlenses has a lateral offset with respect to the fiber bundle (the offset is the same for every connection), then the system is self-correcting as shown in Fig. 3.31. In the worst case, the deflection generated by the offset of the microlens array make the beam reach the edge of the achromat or the edge of the mirror (see Fig. 3.31), or even worse passing beside the achromat or the mirror. Roughly, a lateral offset of the microlens array is tolerable up to 20% of the radius of the microlens. For our system, using a microlens with a diameter $\phi = 245$ μm, a lateral offset of the microlens array with respect to the fiber bundle of 26 μm causes 1dB insertion loss (80% coupling efficiency). A lateral offset of the microlens array is without noticeable influence up to 15 μm.

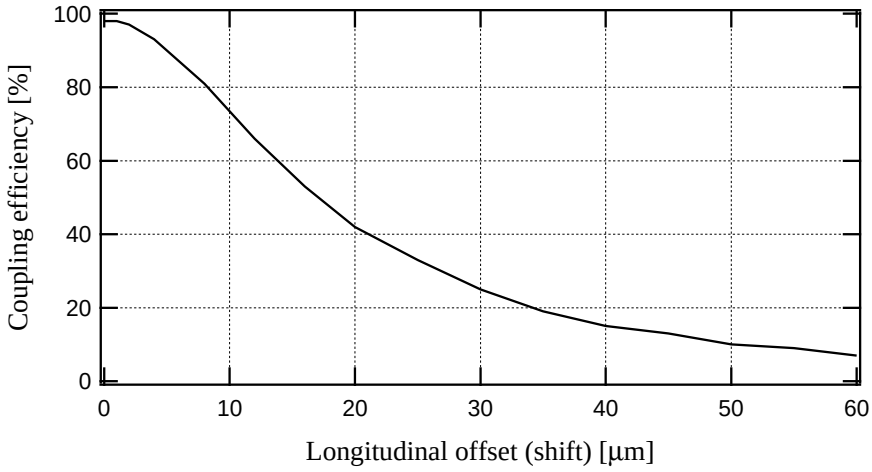

a)

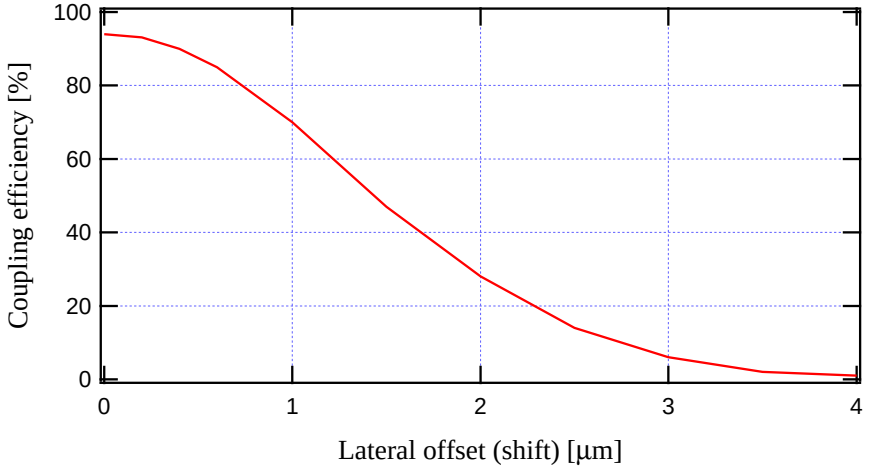

b)

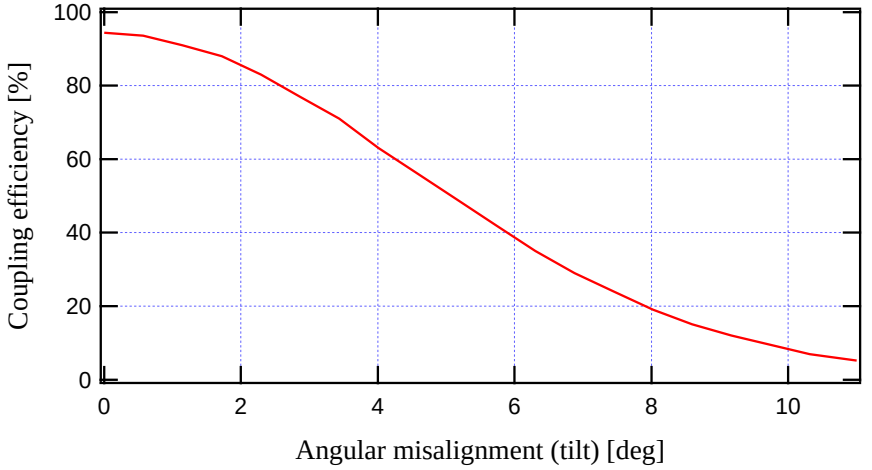

c)

Figure 3.30: $4f$ system with microlenses, achromat and flat mirror ($NA_{fiber} = 0.11$, $f = 40$ mm): power coupling efficiency versus a) longitudinal misalignment, b) lateral misalignment and c) angular misalignment of the receiver fiber.

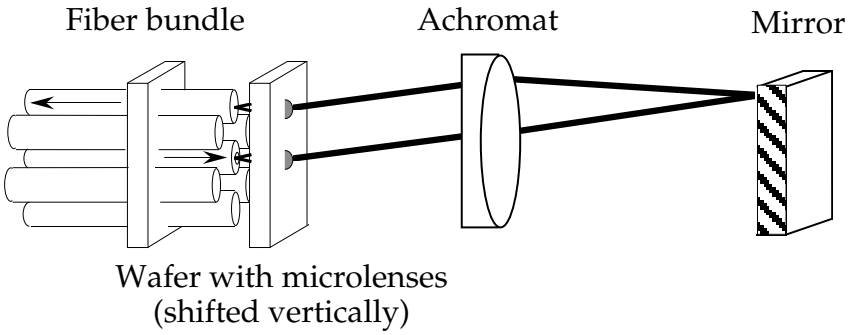

Figure 3.31: Effect of a lateral shift of the array of microlenses with respect to the fiber bundle.

The lateral misalignment tolerances of the achromat shown in Fig. 3.32 are less critical than for the system without microlenses. An offset of $\delta x/2$ of the

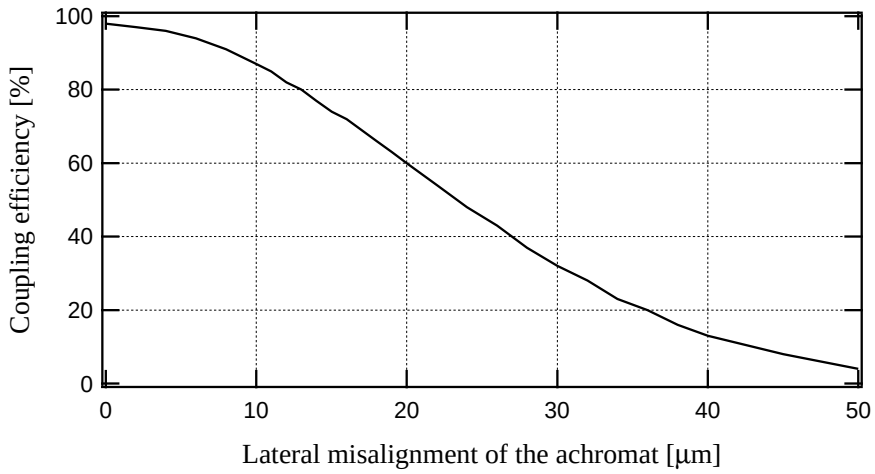

Figure 3.32: $4f$ system with microlenses, achromat and flat mirror: power coupling efficiency versus lateral misalignment of the achromat. ($NA_{fiber} = 0.11$, $f_{achr} = 40$ mm, $f_{ml} = 660$ μm)

achromat generates an offset of the incoming beam on the microlens of δx which finally results in an angular misalignment $\delta\theta \cong \delta x/f_{ml}$ on the receiver fiber, as shown in Fig. 3.33. A lateral misalignment of 13 μm of the achromat causes 1dB insertion loss (80% coupling efficiency). This important result is to compare with the lateral misalignment tolerances of the achromat for the system without microlenses (0.5 μm for 1 dB insertion loss, see Fig. 3.18). As a reminder, the displacement of the achromat to switch from one position to the next one is 125 μm (see section 3.5.3).

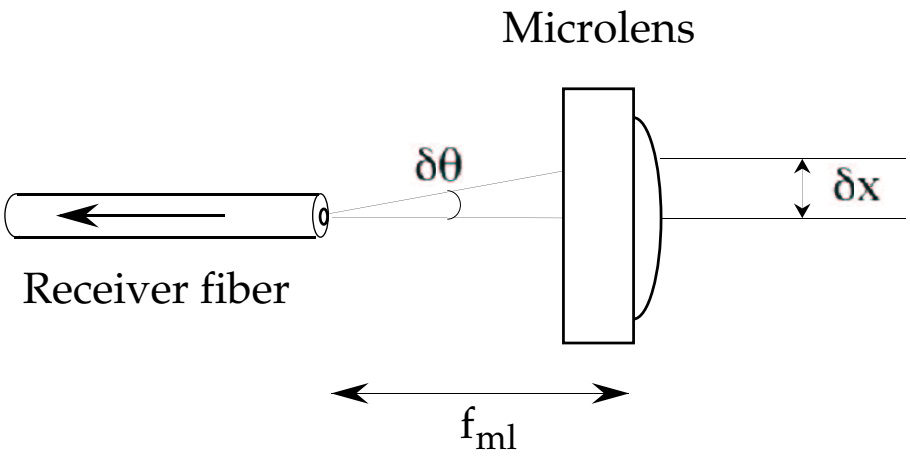

Figure 3.33: Schematic of the angular misalignment $\delta\theta = \delta x / f_{ml}$ resulting from a lateral offset $\delta x/2$ of the achromat (not shown in the figure).

We have seen in this section the advantages to use an array of microlenses in front of the array of fibers. The alignment tolerances of the achromat are relaxed and the power coupling efficiency is high due to low aberrations. Nevertheless, the alignment tolerances of each individual receiver fiber are quite severe: 0.7 μm lateral misalignment of one receiver fiber generates 1dB insertion loss (Fig. 3.30 b)). This critical point requires a high precision on both fiber and microlens arrays. The distance between the microlenses is very accurate as the array is fabricated by photolithography (section 3.7.3). The position of the fibers inside the bundle is however less accurate. This is due to the eccentricity of the core of the fiber which is in the range of 1 μm and to the positioning of the fiber into the bundle. Although a fiber bundle with lateral alignment tolerances better than 1 μm is possible, to date, no such 2-dimensional singlemode fiber bundles are commercially available. Linear arrays of fibers are however commercially available. We will use a linear array of 32 singlemode fibers to demonstrate our switching systems. Fundamentally, there are no more challenges to move the achromat in both X and Y directions than only in one direction.

3.7.3 Fabrication and characteristics of the microlenses

In this section, we describe briefly the fabrication process of the plano-convex microlenses and their main characteristics. The microlenses are fabricated by the melting resist technology [59], as shown in Fig. 3.34. A thick layer (1 μm

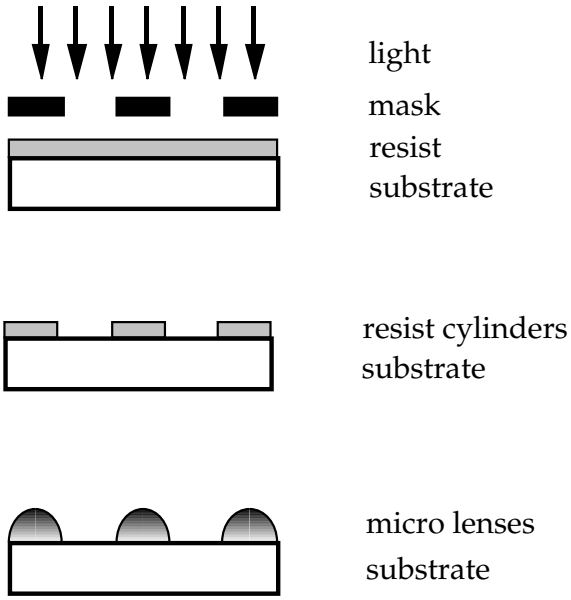

Figure 3.34: The three steps of the melting resist technology for the fabrication of refractive microlenses: exposure, development, and melting of the resist structure.

to 100 μm) of photoresist is spin-coated over a base layer (0.5 μm to 1 μm), spin-coated on a quartz substrate. After a prebake, the resist is exposed. Photoresist cylinders are obtained after standard developing. These cylinders are then melted at a temperature of 150°C to 200°C. The resulting structures act like microlenses. A careful optimization of all process steps is necessary in order to obtain a suitable lens profile with a good optical performance.

The microlens is characterized by the radius r and the height h_l at the vertex. The radius of curvature R at the vertex is then [59]

$$R = \frac{h_l}{2} + \frac{r^2}{2h_l}, \tag{3.24}$$

and the focal length is found to be

$$f_{ml} = \frac{R}{n-1} = \frac{h_l + \frac{r^2}{h_l}}{2(n-1)}, \tag{3.25}$$

where n is the refractive index of the resist. Figure 3.35 shows a photograph of microlenses in photoresist after the melting process.

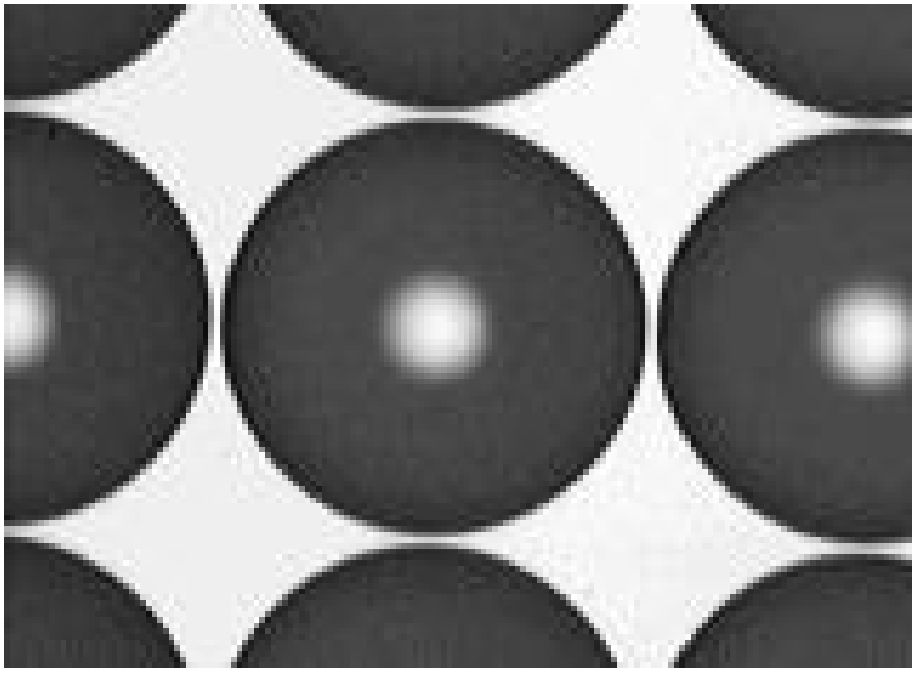

Figure 3.35: Photograph of photoresist microlenses with a diameter of 245 μm.

In order to characterize the microlenses, several methods are used. The height of the lens and its surface profile are measured using a mechanical profilometer. A Twyman-Green interferometer [60, 61] is used to measure the deviation of the surface profile from an ideal sphere and the radius of curvature R at the vertex. In addition a Mach-Zehnder interferometer [60], working in transmission, is used to measure the wave aberrations of the plano-convex microlens.

Chapter 4

Experimental results

This chapter is divided in three sections corresponding to three different $4f$ systems. Section 4.2 describes the system with the lowest complexity. The fiber switch is made of an achromat and a flat mirror. The limits of such an optical switch are demonstrated. In section 4.3, the flat mirror is replaced by a deformable mirror in order to correct the aberrations. The feedback loop driving the deformation of the membrane mirror and the improvements of the coupling efficiency are described. Finally, in section 4.4, an optical switch system with microlenses in front of the fibers, an achromat and a flat mirror is presented. The characteristics of the microlenses and their contribution to the high coupling efficiency are shown.

4.1 General description

All three $4f$ systems are composed of one singlemode source fiber placed in the front focal plane of a lens and a mirror placed in the back focal plane, which reflects the light. After passing the lens again, the light is focused into a singlemode receiver fiber located a the same plane as the source fiber. Moving the lens laterally allows to switch from the source fiber to one of the receiver fibers. Figure 4.1 shows a schematic drawing of the switching system. The lines are rays calculated by the ray-tracing program Zemax©. The experimental setup is schematically shown in Fig. 4.2. Light emitted from a He-Ne laser ($\lambda = 633$ nm) is coupled into a singlemode fiber using an aspheric lens. A coupler 92% / 8% splits the signal into a reference fiber and a source fiber. The source fiber is part of a linear array of 32 singlemode fibers. The 32 fibers are held in a commercially available (Wave Optics) silicon V-groove array, as shown in Fig. 4.3. The distance between adjacent fiber cores is 250 μm $\pm$ 0.5 μm. The singlemode fibers have a cut-off wavelength $\lambda_{cut-off} = 590$ nm. The mode field diameter is $2w_s = 4.5$ μm, corresponding to a core diameter of $\phi_{core} = 3.8$ μm and the numerical aperture of $NA_{fiber} = 0.11$. The cladding diameter is $\phi_{cladding} = 125$ μm. The linear array of

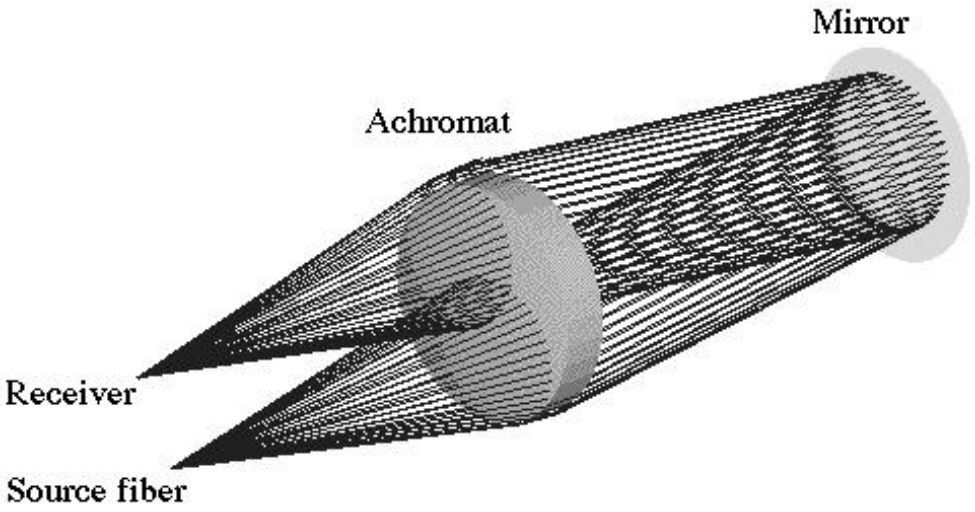

Figure 4.1: Ray tracing of the switching system.

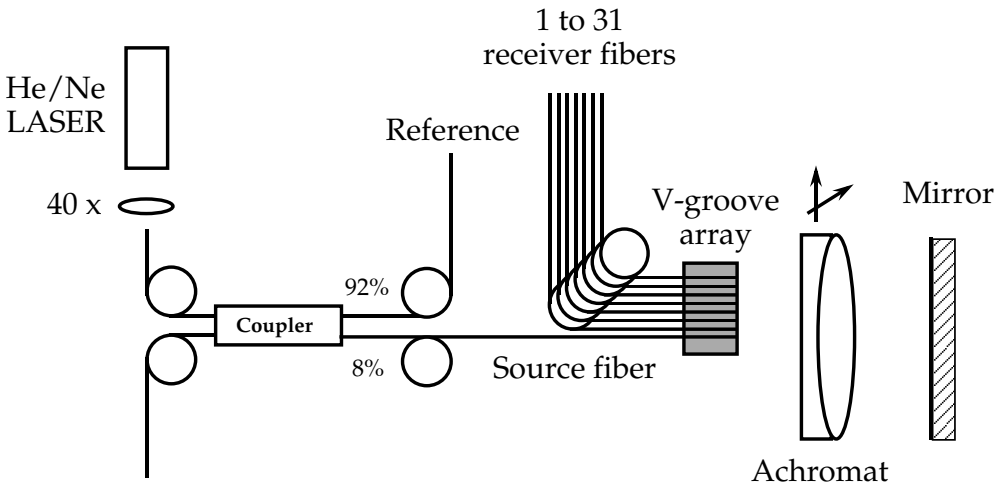

Figure 4.2: Experimental setup of the switching system.

fibers is placed in the front focal plane of the lens, whereas the mirror is placed in the back focal plane. The lens is an achromat of focal length $f = 40$ mm with an anti-reflective coating (reflectance $< 0.3\%$). The achromat is a commercially available doublet (Linos # 322209, see Fig 3.14) made of SF2 (n=1.64 at 633 nm) and BK7 (n=1.52 at 633 nm). Switching from the source fiber to any of the 31 receiver fibers is possible by moving the achromat laterally using a precision x-y stage with a resolution of ~ 0.14 μm. The signals from the receiver fiber and the reference fiber are detected with calibrated silicon photodiodes. The ratio of the receiver and the reference signal gives the coupling efficiency. The way

we use the linear array of fibers, the source fiber at one end, demonstrates the feasibility of a system, which is twice as large with symmetric displacement of the achromat. The 32 fiber linear array can demonstrate the feasibility of a 1 × 62 1-dimensional system. Moreover, 2-dimensional arrays could be switched if the achromat is displaced in both x and y directions. The 32 fiber linear array can thus demonstrate the feasibility of a 1 × 3019 2-dimensional system (see Fig. 3.23).

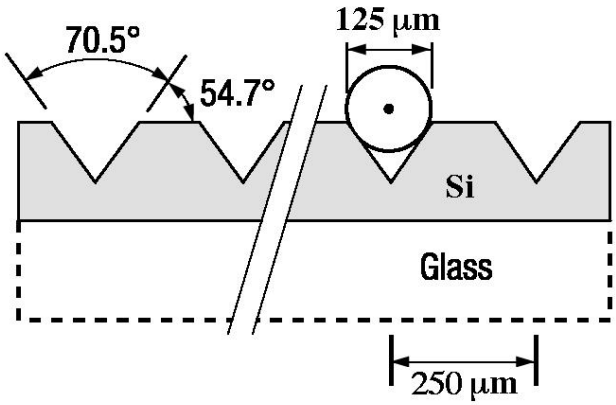

Figure 4.3: Schematic drawing of the array of V-grooves in silicon to hold the fibers.

4.2 Fiber switch with a flat mirror

In the first system, we use a flat, silver-coated mirror with a reflectivity of 96%. The surface quality is better than $\lambda/10$. Switching from the source fiber to any of the 31 receiver fibers is obtained by moving the achromat laterally with the precision x-y stage (see Fig. 4.2). The coupling efficiency is optimized by adjusting the distance between the fiber holder and the achromat for every connection. Figure 4.4 shows the measured coupling efficiency, together with the calculated values (see section 3.5.3). The total losses due to the optical elements are estimated to

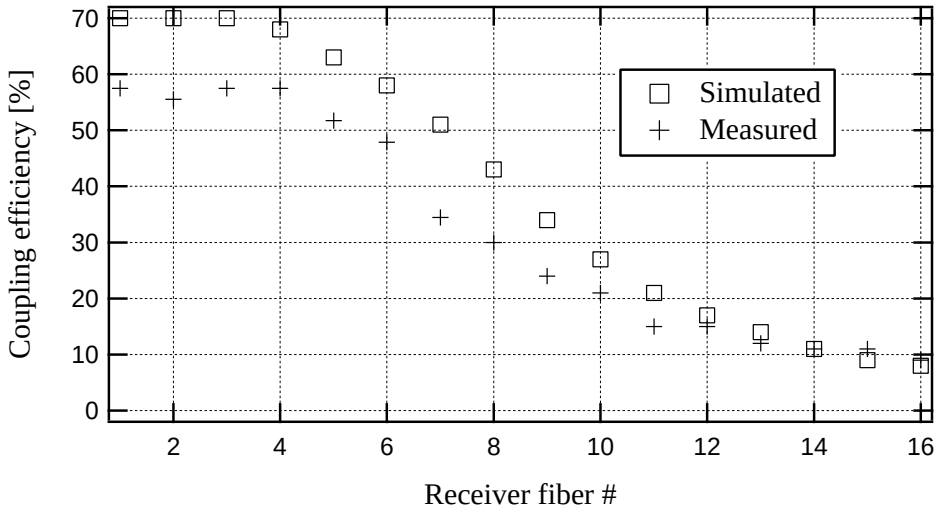

Figure 4.4: Measured coupling efficiency using a flat mirror, compared with simulation (section 3.5.3.

be 14%, by taking into account 4% Fresnel losses at the interfaces of the source and the receiver fiber, 1% transmission loss for the achromat and 0.3% reflectance at both interfaces, and 96% reflectivity for the mirror. Figure 4.4 shows the coupling efficiency for 1 dimensional, 1 directional 1×16 switching. The measured coupling efficiency decreases with increasing distance between the source fiber and the receiver fibers, as predicted by the simulations. This decrease is due to the aberrations of the system described in section 3.5. These results demonstrate the limit for such an optical switch without further aberration correction. Six receiver fibers can be addressed with a coupling efficiency better than 50% (less than 3 dB insertion loss) without the 14% residual losses. A corresponding 2-dimensional system with less than 3 dB insertion loss could address 113 receiver fibers (quadratic array of fibers encircled in a radius of 6 fibers, see Fig. 3.23).

The tolerances for a lateral offset of the receiver fiber are also measured and the result is shown in Fig. 4.5.

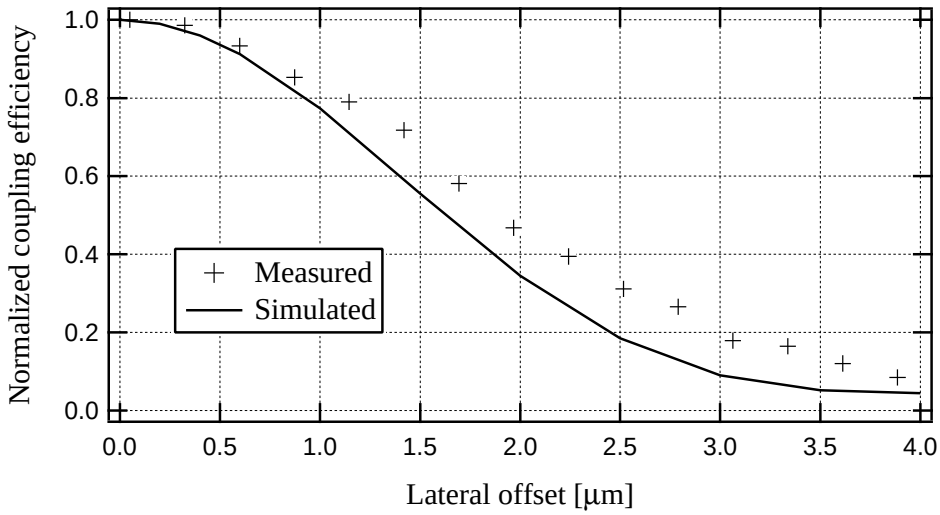

Figure 4.5: Measured coupling efficiency for a lateral offset of the receiver fiber, compared with simulation (section 3.5.2).

These measured tolerances are in good agreement with the simulated ones (see section 3.5.2). For high efficiency, an accuracy of 0.5 μm is required for the position of the receiver fiber. A lateral misalignment of the achromat produces a lateral misalignment of the beam on the receiver fiber twice as large. Therefore, the required accuracy for the position of the achromat is 0.25 μm.

4.3 Fiber switch with a deformable mirror

In order to correct the aberrations of the system, we replace the flat mirror used in section 4.2 by a deformable membrane mirror described in section 3.6. The membrane deformable mirror is used to modify the wavefront and to optimize it in order to maximize the power coupling efficiency measured at any of the 31 receiver fibers. Figure 4.6 is a picture of the experimental setup.

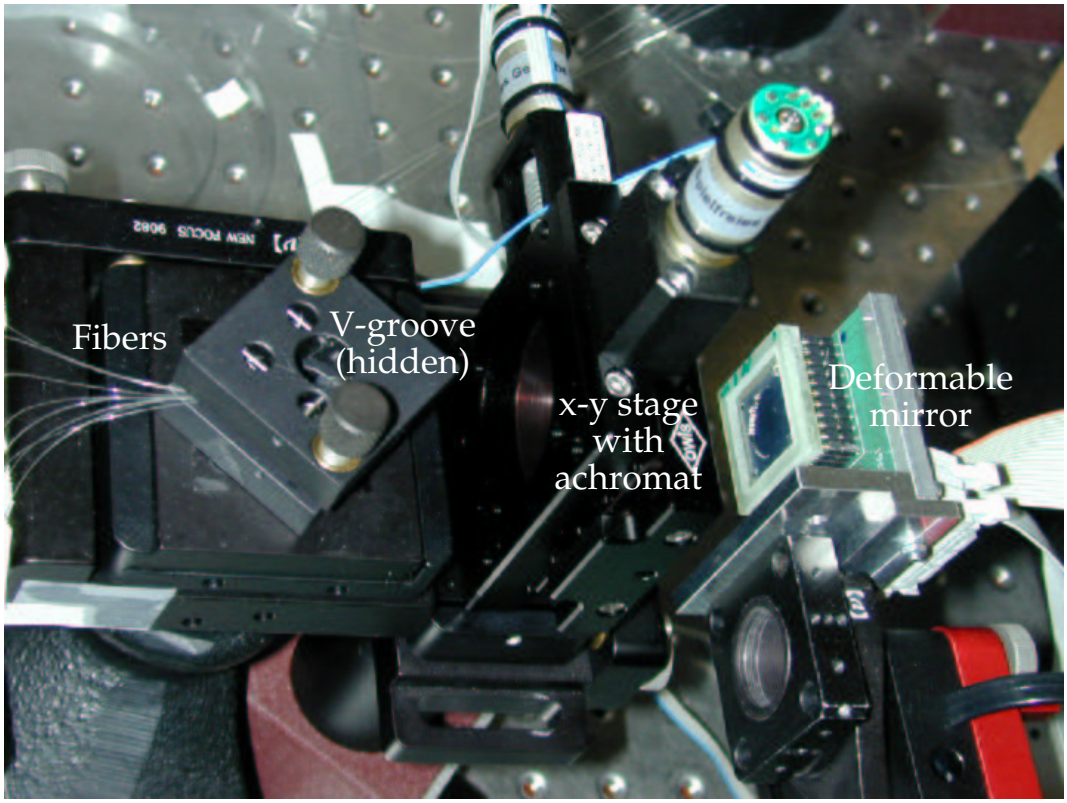

Figure 4.6: Experimental setup of the switching system with the 1-D array of fibers, the achromat mounted on a x-y stage and the deformable mirror.

In order to achieve a bidirectional movement of the membrane of the deformable mirror, a bias voltage of $V_b = 130\ V$ is applied to the membrane. When all control voltages of the electrodes are equal to zero, the membrane has a parabolic shape with a deflection of 6 μm at the center (see section 3.6). The chosen connection (among the 31 possibilities) is set by the lateral displacement of the achromat. A feedback loop based on a genetic algorithm [62] optimizes the receiver fiber coupling efficiency for each receiver fiber individually. The genetic algorithm, schematically described in Fig. 4.7, is based on the deformation modes of the mirror (see Tab. 3.2). A first set of one thousand deformations is

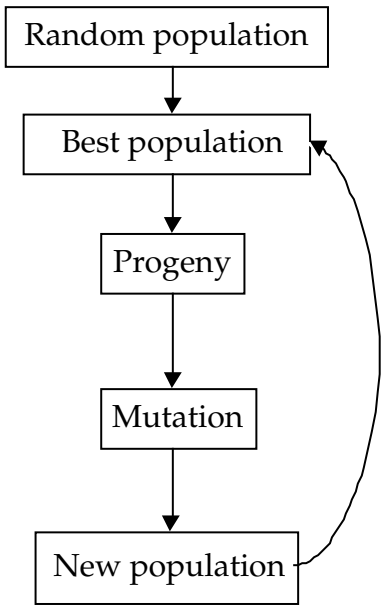

Figure 4.7: Genetic algorithm based on the deformation modes of the membrane.

randomly chosen. Each deformation is the result of the random superposition of several modes. Each mode corresponds to a specific electrode configuration. From this first set of one thousand configurations the best ten are kept. The value of each mode of the ten configurations is used to generate one hundred progeny configurations with 10% of mutations. Among these one hundred configurations, the ten best are kept to generate the second generation. In general, after ten generations the algorithm has converged (see Fig. 4.8). The important parameters to get good convergence are the amount of mutations, as well as the number of modes used. Fifteen to twenty modes are enough for the optimization. If less than fifteen modes are used, the optimization is not optimal. With more than twenty modes, the algorithm gets slower without a significant improvement of the result. It is not astonishing that the number of useful modes is in the 15-20 range as it corresponds to the aberrations up to the sixth order (secondary aberrations). Optimization curves for most of the 31 configurations are shown in Fig. 4.8. These curves represent the evolution of the power coupling efficiency. The optimization time is several minutes. However, each connection has its own optimized deformation which can be memorized, storing the voltage applied on each electrode. With these preset values, and thanks to the good repeatability of the deformation of the membrane [63], the optimized deformation can be recalled for a later connection to the same receiver fiber. The reproducibility of a connection could however not be tested, because of a large backlash ($\sim$ 20 μm) of the x-y stage. The optimized power coupling efficiency is between 25% and 51%, as shown in Fig. 4.9. The total loss due to the optical elements is estimated

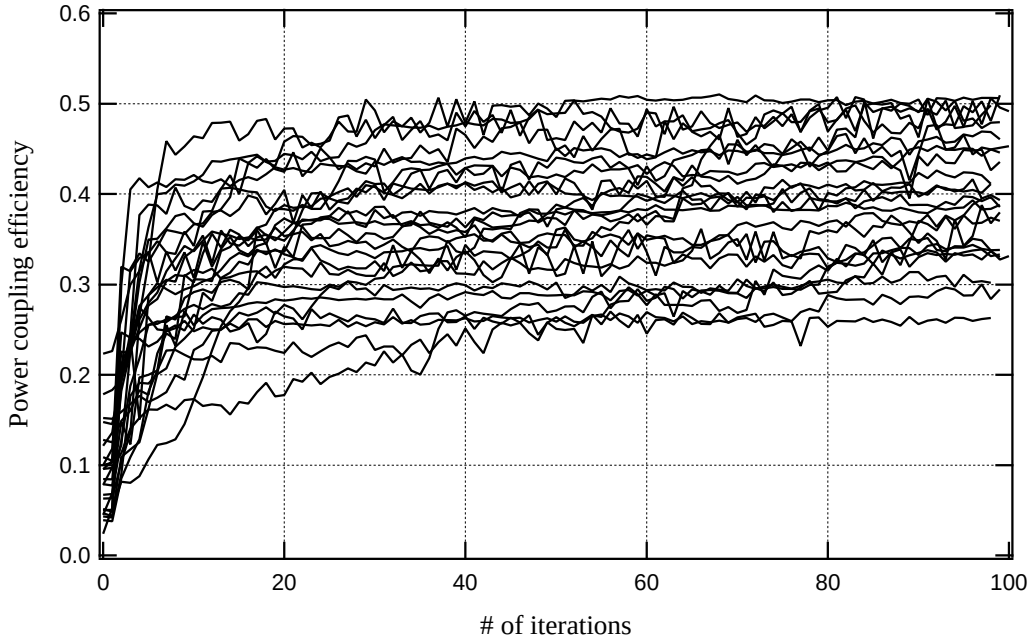

Figure 4.8: Optimization curves for most of the 31 configurations.

to be 22%, by considering two interfaces between the receiver fiber and air, with 4% Fresnel losses each, 1% transmission loss inside the achromat and 0.3% of reflectance at both interfaces and a reflectivity of 87% for the mirror. The difference between the maximum coupling efficiency (78%) and the measured ones (51%) has several reasons. First, the mirror we used has a high astigmatism at rest, because of residual stress in the membrane (see section 3.6). Simulations show that an astigmatism of $\lambda/5$ leads to a coupling efficiency decrease of 50%. The measured deviation of the membrane from the perfect plane corresponds to $3\lambda - 4\lambda$ at rest. 4λ corresponds to a quarter of the correction range of the mirror. Although the mirror has the potential to correct its own imperfections, this limits the ability to further correct the system aberrations. A second point limits the performance of the mirror: the instability of the voltage supply. Fluctuations have been measured which lead to a maximum deformation fluctuation of 0.1 μm ($\cong \lambda/6$) at the center of the membrane at maximum voltage $V = 190\ V$.

With the voltage of the electrodes, the surface deformation of the mirror can be reconstructed using a finite element model [58]. This model describes the membrane surface with a set of Zernike polynomials. The Zernike coefficients are directly related to the corrected aberrations (see section 2.2). Figure 4.10 shows a reconstructed membrane surface for a connection to the 15th receiver fiber with 51% power coupling efficiency. The deformation due to the corrections of the

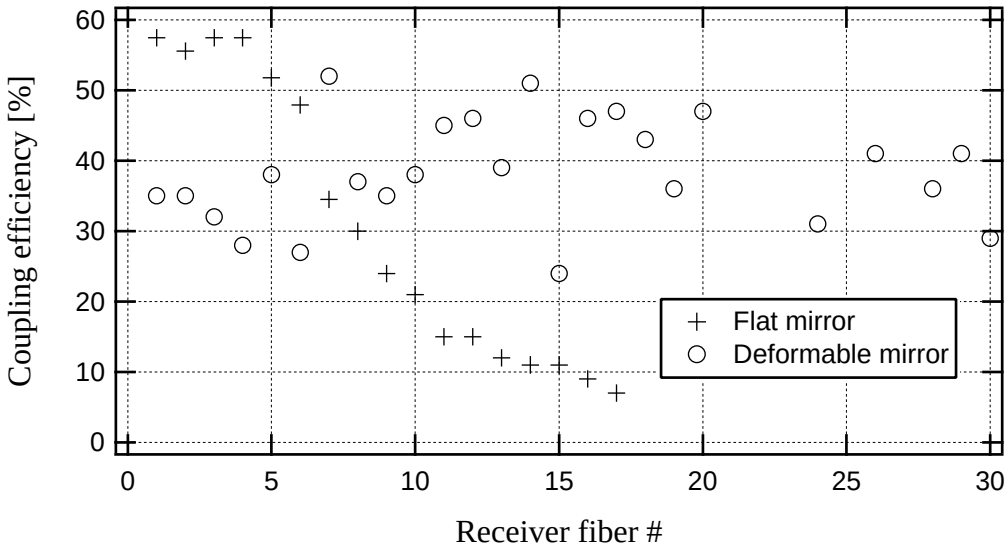

Figure 4.9: Measured coupling efficiency using a deformable mirror, compared with the flat mirror (section 4.2).

aberrations is added to the initial bias deformation. The corresponding Zernike coefficients are presented in Fig. 4.11. The piston term (1) and the defocus term (5) are due to the bias deformation. The other main terms are primary astigmatism (4 & 6), coma (9), spherical aberration (13) and secondary astigmatism (12 & 14).

We would expect that the Zernike coefficients corresponding to the deformation of the membrane are related to the Zernike coefficients describing the aberrations of the connection without deformable mirror. Figure 4.12 shows the Zernike coefficients calculated from a simulation of the connection to the 15th receiver fiber with a flat mirror. The main terms beside piston and defocus are primary and secondary astigmatism (6 & 14) and spherical aberration (13). The comparison of both Zernike coefficients of the reconstructed membrane deformation and of the simulated system with a flat mirror does not show any evident correlation. This is mainly due to the intrinsic astigmatism of the membrane, which generates an offset for all other deformation modes and thus leads to another set of (real deformation) Zernike polynomials. Moreover, the finite element model does not take into account the stress of the membrane. This leads to an offset for the calculated deformation Zernike polynomials. Because of the finite number of electrodes (37), the capacity of the deformable mirror is limited to the first 15-20 Zernike coefficients.

Figure 4.13 shows a simulated interferogram of the calculated aberrations for the connection to the 15th receiver fiber with a flat mirror given by the Zernike coefficients shown in Fig. 4.12. The interferogram results from the interference of

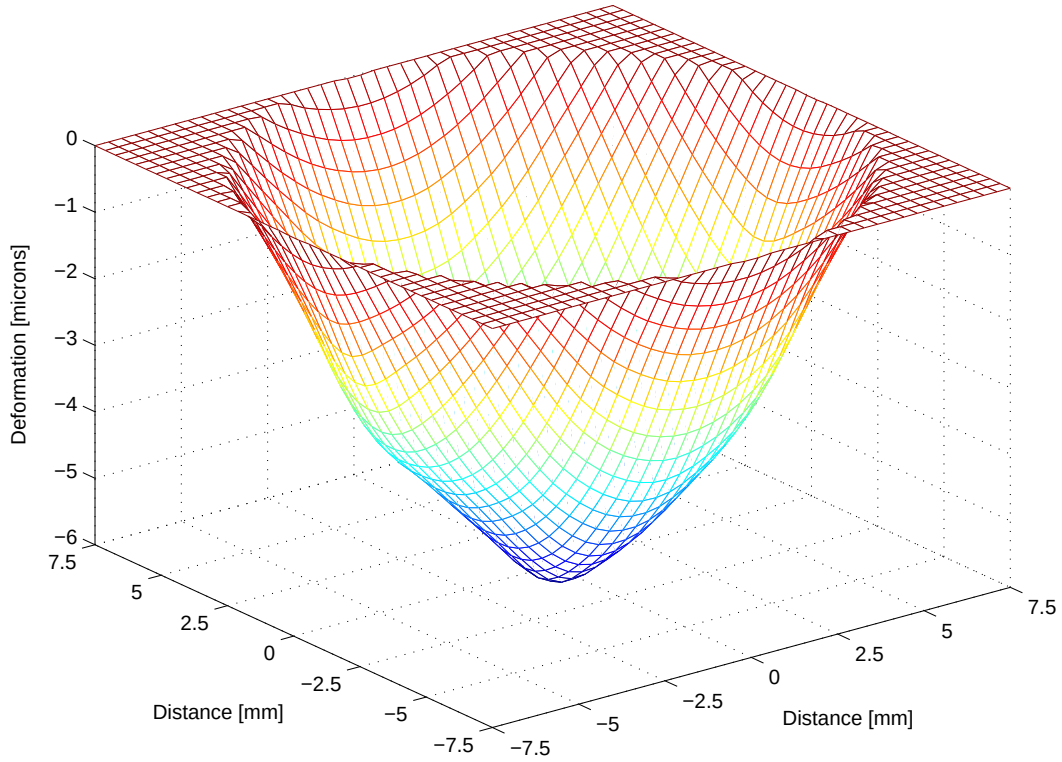

Figure 4.10: Reconstructed membrane surface of the mirror for the optimized connection to the 15th receiver fiber (bias voltage + electrodes voltage).

the simulated beam with a reference beam, which has an optical path difference (OPD) equal to zero.

In this section, we have shown how a deformable membrane mirror can correct the aberrations of an optical switching system. The measured coupling efficiency for connections up to the 31th receiver fiber of a 1 dimensional, 1 directional system fluctuates between 25% and 51% (including the 22% losses due to the optical components). Compared to an optical system without correction of the aberrations (see section 4.2), the system with the deformable mirror is better for connections from the eighth receiver fiber and higher (see Fig. 4.9). We demonstrated a 1-dimensional, 1 directional 1×31 optical switching system which corresponds to a 1×3019 2-dimensional system (see Fig. 3.23). The limit of the 1-dimensional, 1 directional 31th receiver fiber is given by the size of the achromat and its lateral displacement required for the switching. A larger achromat (with a larger focal length) and a larger deformable mirror should be able to address more receiver fibers.
The correction of aberrations was limited in our experiments by the residual stress

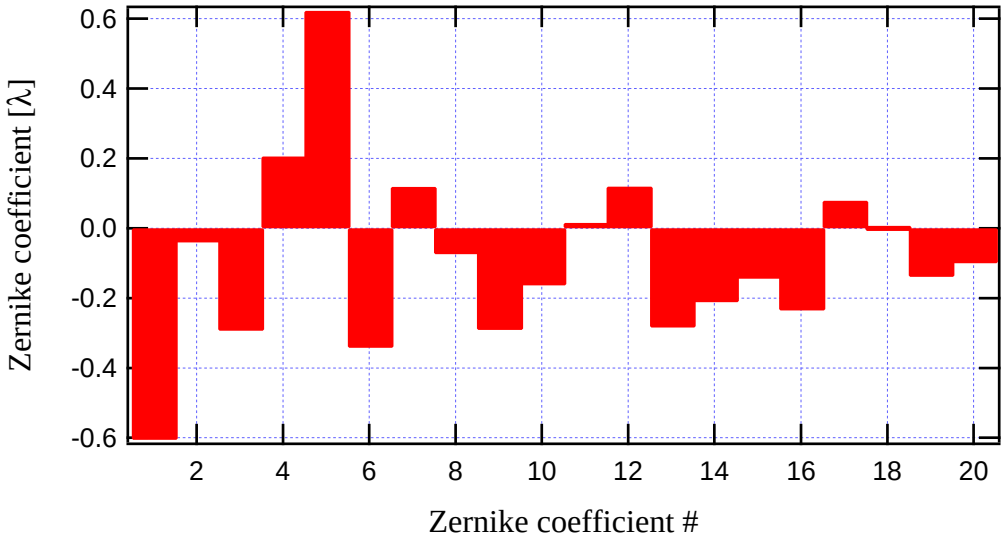

Figure 4.11: Zernike coefficients representing the reconstructed deformation of the membrane for the connection to the 15th receiver fiber. (See Tab. 3.2 for the description of the coefficients)

of the membrane. Deformable membrane mirrors with almost no stress have been reported [52] and would improve the coupling efficiency by around 10 percents. Because of the hexagonal geometry of the electrode structure, some types of aberrations can be corrected more easily than others. For example, the secondary astigmatism (or ashtray) is particularly well adapted to be corrected by a hexagonal structure of electrodes. In contrary, the spherical aberration is more difficult to correct, since the center part of the membrane has to be pushed and a circular ring has to be pulled (see Fig. 2.8). A circular structure of electrodes would be more adapted for such a deformation. Deformable membrane mirrors with different electrode structures are commercially available [64] and show the feasibility of such improvements.
In conclusion, the use of a mirror with less stress in the membrane and with a specific structure of electrodes (adapted to the main aberrations to correct) would bring a significantly better coupling efficiency. Finally, the use of a x-y stage with a repeatability better than 1 μm is necessary to recall memorized connections. Such x-y stage are commercially available (e.g. Newport$_{\circledR}$: M-MFN and PM or OWIS: LIMES).

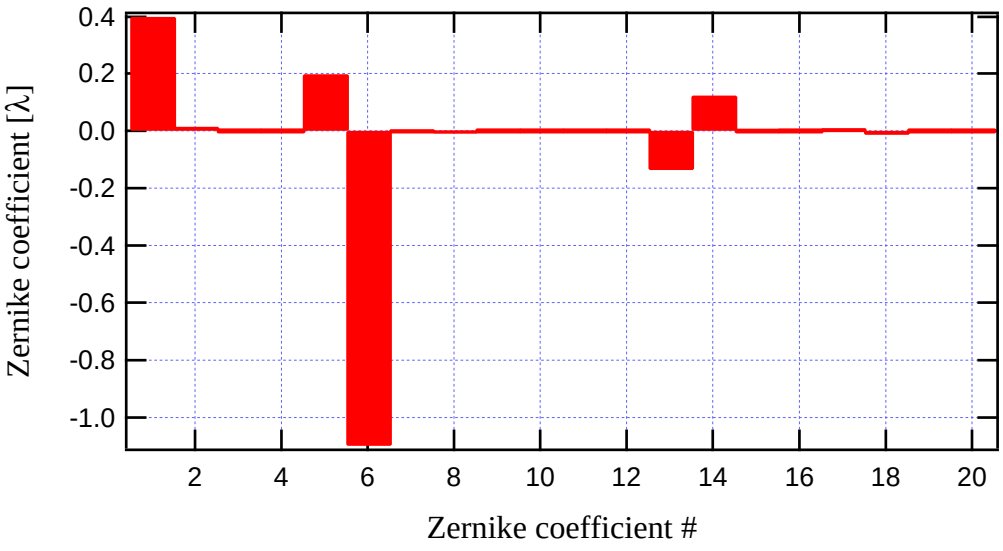

Figure 4.12: Calculated Zernike coefficients for the connection to the 15th receiver fiber with a flat mirror. (See Tab. 3.2 for the description of the coefficients)

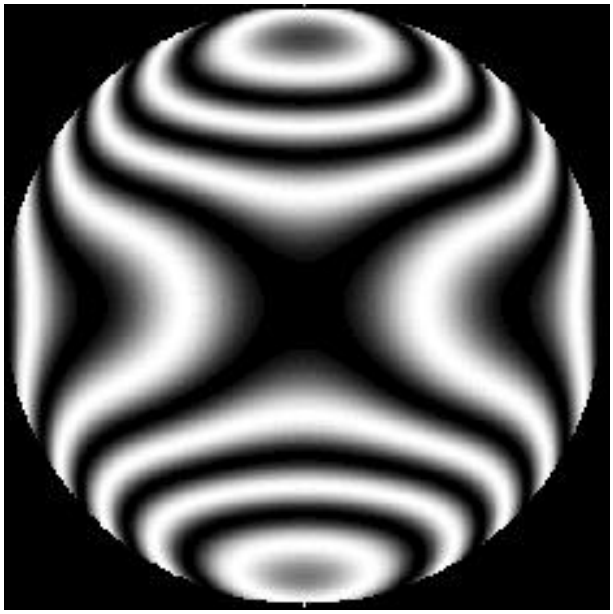

Figure 4.13: Simulated interferogram of the calculated aberrations for the connection to the 15th receiver fiber with a flat mirror.

4.4 Fiber switch using microlens arrays

In section 4.2, the limit of the optical switch using an achromat and a flat mirror has been demonstrated. In section 4.3, we introduce a deformable mirror to correct the aberrations. In the present section, we investigate another way to reduce the aberrations. As described theoretically in section 3.5, the aberrations are proportional to the power four of the numerical aperture of the system. In order to reduce the effective aperture of the achromat, we propose to place a microlens in front of each source and receiver fiber (see Fig. 3.29). The function of the microlens placed at the output of the source fiber is to collimate the beam. The microlenses placed in front of the receiver fibers focuses the beam into the fiber core. The switching function is done by a lateral displacement of the achromat. We use a microlens fabricated by the melting resist technology (see section 3.7.3) with a diameter $\phi = 245\ \mu$m. The measured height at the vertex is $h_l = 23.6\ \mu$m. The focal length is calculated by Eq. (3.25) as $f_{ml} \simeq 660\ \mu$m. The microlens aberrations of the illuminated disc ($\phi = 94\ \mu$m) were measured with a Mach-Zehnder interferometer (see section 3.7.3). The result is shown in Fig. 4.14. The measured

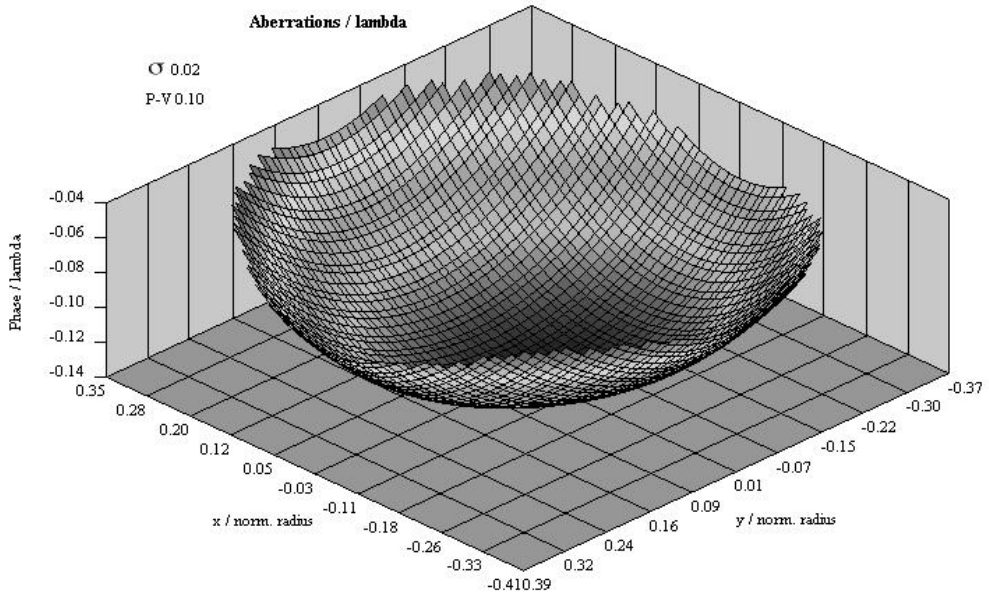

Figure 4.14: Aberrations of the illuminated disc ($\phi = 94\ \mu$m) of the microlens ($f_{ml} \simeq 660\ \mu$m), measured with a Mach-Zehnder interferometer.

standard deviation of the aberrations (see Eq. (2.57)) is $\sigma_{_W} = 0.02\lambda$, which corresponds to a Strehl ratio of $0.98 \cong \eta$. The quality of the microlens is then very good. Almost no losses are generated by the aberrations of the microlens. Figure 4.15 shows the corresponding Zernike coefficients of the microlens aberrations. The experimental setup of the switching system is shown in Fig. 4.16. The wafer

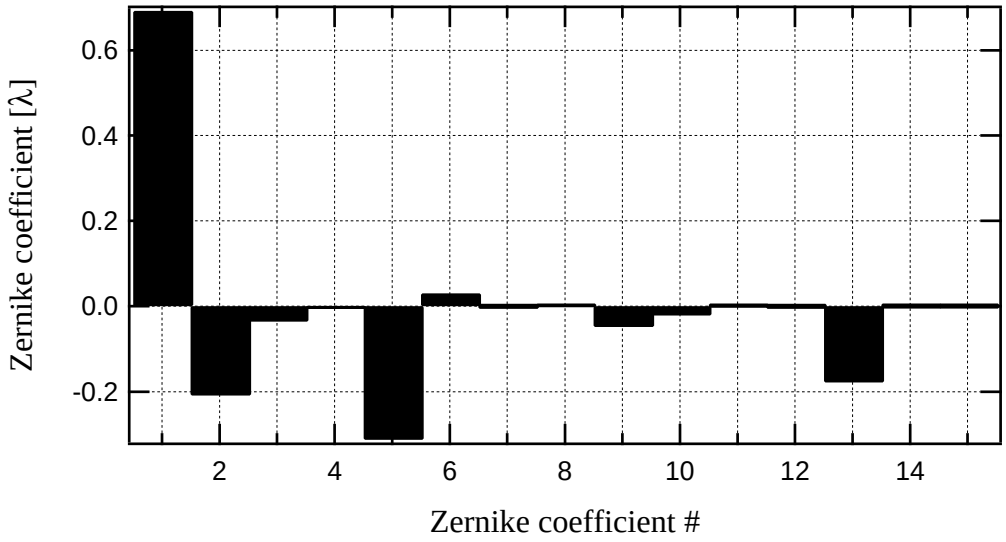

Figure 4.15: The first fifteen Zernike coefficients of the illuminated disc (ϕ = 94 μm) of the microlens, obtained from Fig. 4.14. (See Tab. 3.2 for the description of the coefficients)

with the array of microlenses is placed in front of a V-groove array, containing the fibers, as shown in Fig. 4.3, and is adjusted using a x-y-z stage (1 μm resolution). The lateral displacement of the achromat allows to switch the 31 receiver fibers. The collimated beam is focused onto the flat mirror. Figure 4.17 shows a detailed view of the array of microlenses and the linear array of V-grooves. The system allows to switch the signal from the source fiber, up to the 31th fiber with a coupling efficiency between 50% and 61%, as shown in Fig. 4.18. The total loss due to the optical elements is estimated to be 36%, by considering two interfaces between the microlens and air (index matching oil is used between the fibers and the wafer with the microlenses, see Fig. 3.29), with 4% Fresnel losses each, 14% transmission loss inside the photoresist microlens, 1% transmission loss inside the achromat and 0.3% of reflectance at both interfaces and a reflectivity of 96% for the mirror. The theoretical maximum efficiency is 98% (see section 3.7.1). If we add the losses due to the optical elements (36%) to the maximum measured coupling efficiency (61%), we almost reach the theoretical limit. Cross talk is less than -30 dB (detection limit).
The resist is a material which degrades with the time. It has to be replaced by other materials which are more stable and have less absorption (resist has 14% absorption at λ = 0.633 μm). The resist microlenses can be transferred into different materials by reactive ion etching (RIE) [48]. The choice of the material is wavelength dependent. Fused silica is used for applications with UV light to

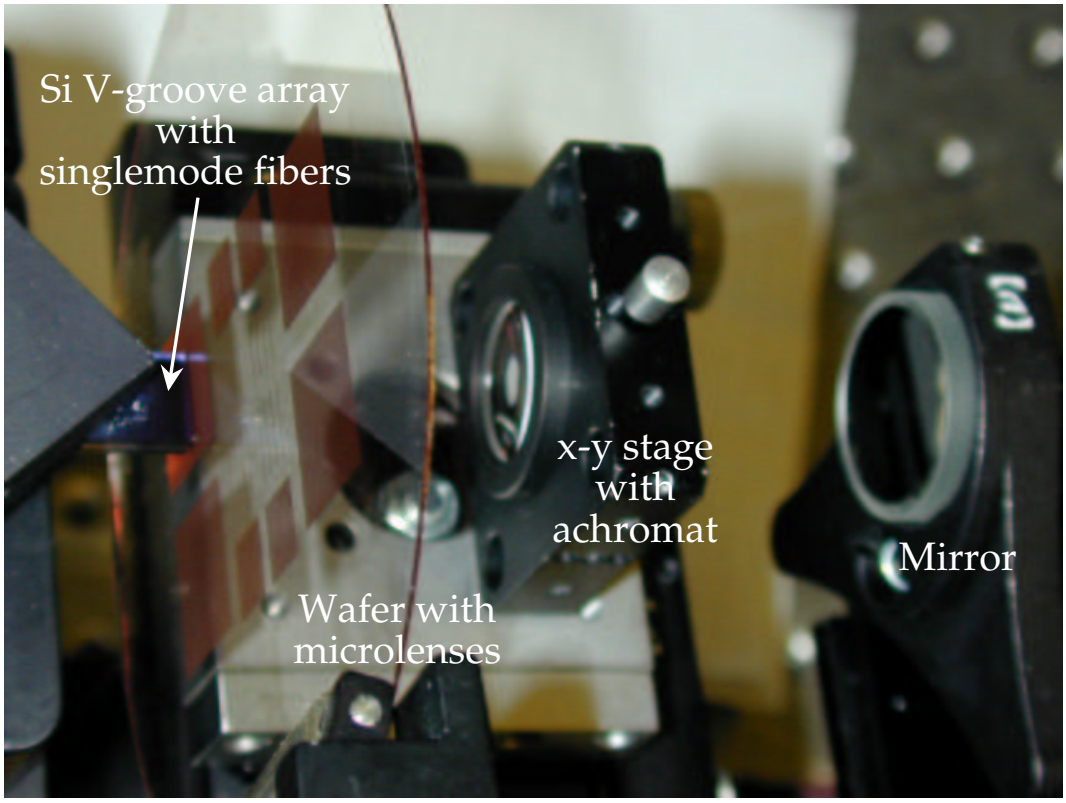

Figure 4.16: Experimental setup of the switching system using a microlens array.

visible and silicon is used for IR applications.

The measured coupling efficiency as a function of the lateral offset of the achromat is shown in Fig. 4.19. These measured tolerances are less critical then the simulated ones (see section 3.7.2, Fig. 3.32). This is probably due to a slight defocus of the microlens which generates a wider spot on the fiber. For high efficiency, an accuracy of the achromat of 10 μm is required. Compared to the switching system without microlens arrays (see section 4.2, Fig. 4.5), which requires 0.25 μm accuracy on the position of the achromat for high efficiency, the system using microlenses is much less critical.

The use of microlenses gives high coupling efficiency with relaxed tolerances of the alignment for the incoming beam on the receiver microlens. The alignment of the linear fiber array with the microlens array is realized with a precision x-y-z stage (1 μm resolution). The reported results indicate that the alignment of the microlens array with the fiber array is possible. Several alignment schemes using a micro-optical bench have been proposed to align plano-convex microlenses with singlemode fibers placed in V-grooves [65, 66]. These solutions, however,

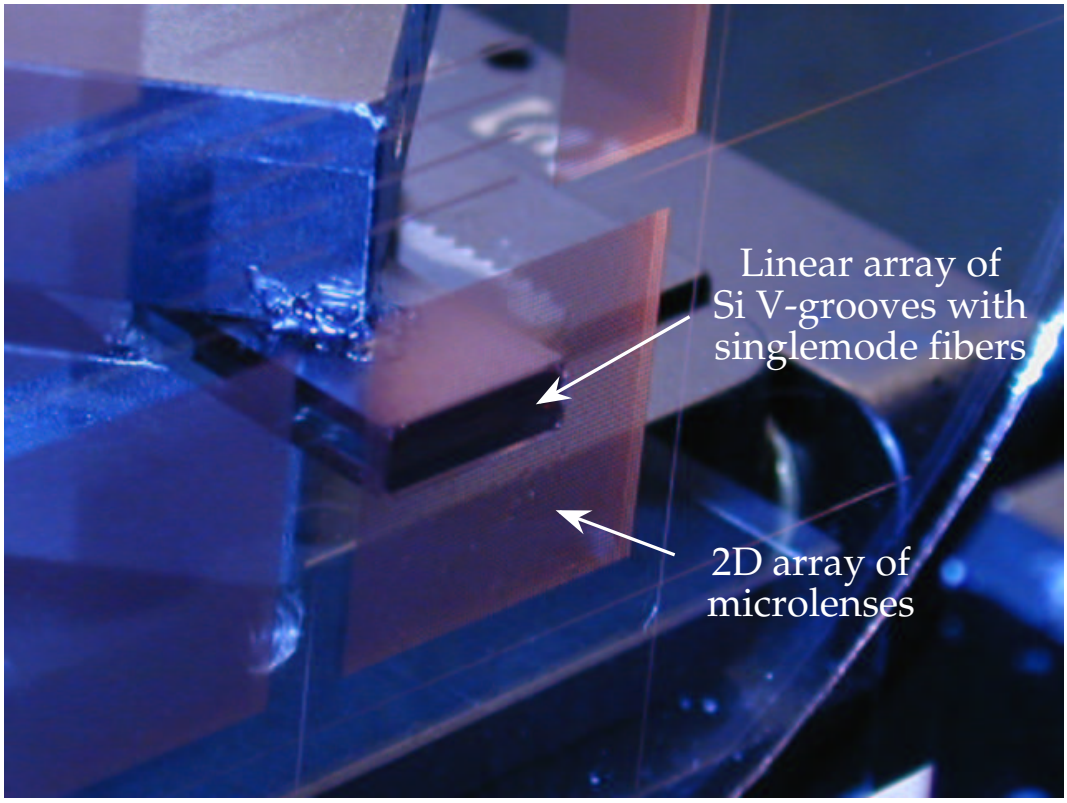

Figure 4.17: The V-groove and the array of microlenses.

remain 1-dimensional. Finally, due to the 20 μm backlash of the x-y stage used to move the achromat, it was not possible to reproduce a connection automatically. However, as mentioned in section 4.3, x-y stages with a backlash of less than 1 μm and resolution in the order of 0.05 μm are commercially available (e.g. Newport$_{\circledR}$: M-MFN or OWIS: LIMES). With such x-y stages, a given connection could be reproduced.

In conclusion, the feasibility of an optical switching system using microlenses for large number of interconnects has been demonstrated. Insertion loss as low as 1 dB (80% coupling efficiency) is almost possible if the microlenses are made in a material with low absorption, like fused silica for UV light and visible or silicon for IR. The use of IR light ($\lambda = 1.55$ μm) instead of red light ($\lambda = 0.633$ μm) would even relax the alignment tolerances. In fact, the diameter of the core of singlemode fibers is around 10 μm for $\lambda = 1.55$ μm and around 4 μm for $\lambda = 0.633$ μm.

Other approaches to replace the array of microlenses have been reported. The fabrication of a lens directly on top of the fiber as was proposed for laser to fiber coupling by Kuwahara et al. [67] and Yamada et al. [68] (arc discharge machining), and by Presby et al. [69] and Edwards et al. [70] (laser micromachining).

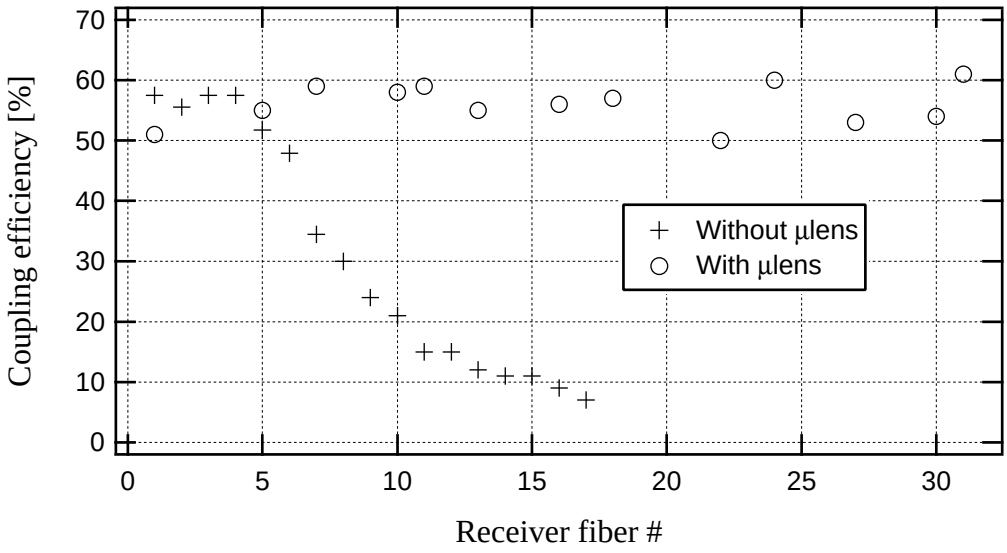

Figure 4.18: Measured coupling efficiency using microlens arrays, compared with the flat mirror (section 4.2).

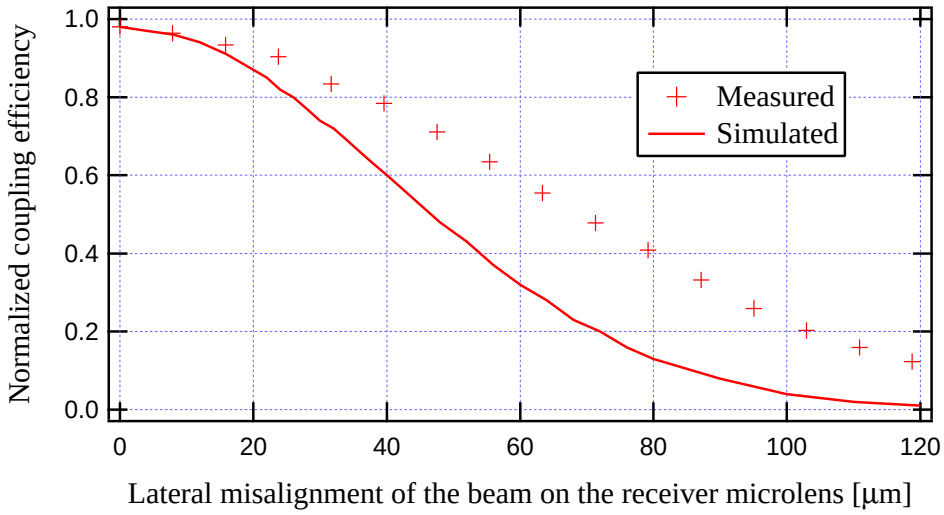

Figure 4.19: Measured coupling efficiency for a lateral misalignment of the beam on the receiver microlens, compared with simulation (section 3.7.2, Fig. 3.32).

Nevertheless, the surface of such microlenses is difficult to fabricate accurately. Moreover, an accurate control of the height of the lens is not possible. As the focal length depends on the height of the lens, homogenous lensed fibers array is not possible with these techniques. Another approach is possible using graded-index (GRIN) fiber-lenses as proposed by Emkey et al. [71] and Chanclou et al.

[72, 73].
Compared to these other approaches, the arrays of microlenses fabricated by the melting resist technology have the advantage of a high homogeneity of the surface quality and of the focal length.

Chapter 5

Conclusion

5.1 Summary of the main results

The aim of this work was to investigate a free space optical switch for large number of interconnects 1 × N, with N>1000. The design of the switch has been studied and a $4f$ imaging system was found to be ideal. The switching is realized by an off-axis position of a lens which has to be large enough ($\phi_{lens} \gtrsim 1.5NA_{fiber}f + b$, where b is the size of the fiber bundle and f the focal length). The aberrations due to the off-axis position of the lens generate losses which limit the number of interconnects. For an insertion loss less than 3 dB, a $4f$ imaging 2-dimensional switching system using an achromat with a focal length $f = 40$ mm is limited to 1 × 153. Experimentally, this limit was found to be 1 × 113. In order to go beyond this limit, two solutions have been proposed and realized. The first solution is to correct adaptively the aberrations, whereas the second solution prevents the generation of large aberrations by a modification of the optical system. A third option would be to use a complex lens system specially designed to be diffraction limited as reported by Ford et al. [22].

A deformable membrane mirror was used to correct adaptively the aberrations. A 1-dimensional, 1 directional system was realized and it demonstrated the capacity to correct the aberrations for a 2-dimensional switch up to 1 × 3019 with measured insertion losses between 6 dB and 3 dB (including 1 dB loss due to optical elements). In our experiment, the number of 3019 is limited by the size of the fiber bundle and by the size of the lens, rather than by the potential of correction by the membrane mirror. Using a larger lens and a larger fiber bundle would allow even more receiver fibers to be connected within the range of 6 dB to 3 dB insertion losses. There is a 2 dB difference between the minimum measured insertion loss (3 dB) and the theoretical limit of 1 dB (losses due to the optical elements in the system). This difference is due to the astigmatism of the deformable mirror at rest, which is caused by the residual mechanical stress

in the membrane. The measured residual astigmatism ($\sim 3 - 4\lambda$) represents a quarter of the correction range of the adaptive mirror. This astigmatism cannot be corrected completely by the adaptive mirror itself, which is the reason for the measured minimum insertion loss of 3 dB. Nevertheless, mirrors with better quality of the membrane are reported [52] and should allow at most 2 dB minimum insertion loss. For 3 dB additional losses, a lateral alignment precision of 0.25 μm was measured for the switching element (the achromat). The resolution of the actuator moving the achromat has therefore to be at least $\Delta x/x_{tot} = 6 \cdot 10^{-5}$, where $x_{tot} = 3.875$ mm is the total displacement of the achromat (31×125 μm).

The modified $4f$ imaging system uses additional microlenses to reduce the aberrations. A hybrid optical system using microlenses and an achromat to switch the connections was investigated. The 245 μm diameter microlenses ($f \cong 660$ μm) are fabricated by the melting resist technology and are arranged in an array with a pitch of 250 μm, corresponding to the pitch size of the array of fibers. Insertion losses below 0.1 dB were calculated for a 1×3019 2-dimensional system. Insertion losses between 3 dB and 2 dB were measured with the realized system. The difference is mainly due to the losses of the optical elements in the system (1.9 dB). The 1-dimensional, 1 directional system which has been realized demonstrates a 2-dimensional 1×3019 system. Again, in our experiment, the number of 3019 is limited rather by the size of the fiber bundle and by the size of the lens. Using a larger lens and a larger fiber bundle would allow even more receiver fibers to be connected within the range of 3 dB to 2 dB insertion losses. The system using microlenses showed relaxed tolerances for the alignment of the achromat, compared to the system without microlenses. For 3 dB additional losses, a lateral alignment precision of 10 μm was measured for the switching element (the achromat). This alignment tolerance results in a resolution of $\Delta x/x_{tot} = 3 \cdot 10^{-3}$.

All switching systems presented in this work have a very low crosstalk, intrinsic to their design. A crosstalk of less than -30 dB (detection limit) was measured.

5.2 Outlook

The systems investigated in this work are slow, because the switching is done by moving the achromat. Shorter switching times could be achieved if the switching was done by tilting the mirror. Although the deformable mirror can hardly be tilted rapidly and precisely enough, due to its size, weight and electronic connections, an additional mirror could be used. Figure 5.1 shows a setup with a switching mirror and a deformable mirror. The switching mirror could be tilted, for example, by piezoelectric actuators, which are precise and rapid.

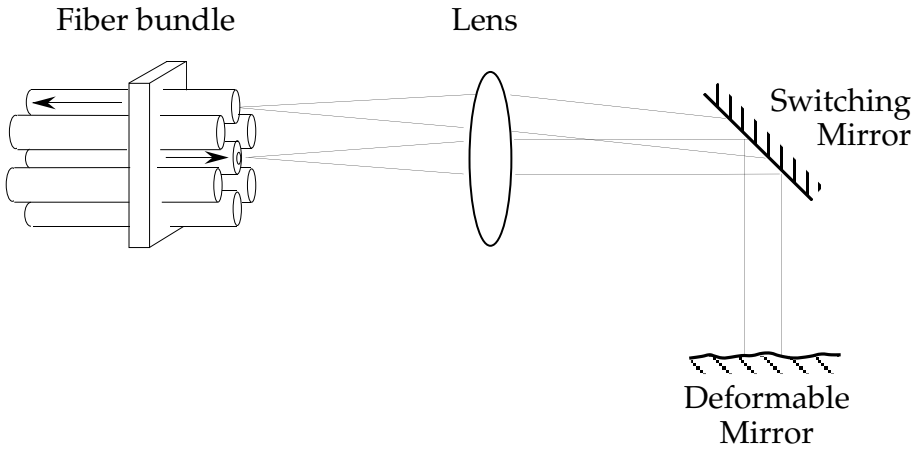

Figure 5.1: Proposed setup with a switching mirror and a deformable mirror.

For the system with microlenses, a possibility to get shorter switching times is to use an array of micromirrors instead of a single macro-mirror. This approach has been first proposed by Hagelin et al. [74] and then also by Lucent [28] with a different optical setup shown in Fig. 5.2. Lucent's optical setup uses diffractive

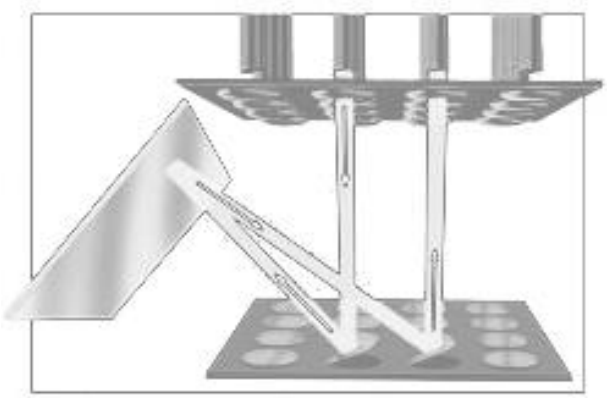

Figure 5.2: Lucent's optical cross-connect using an array of diffractive microlenses and an array of micro-mirrors [28].

microlenses for collimating the light leaving the source fiber and focusing the light onto the receiver fibers, but no macro-lens (achromat). The micromirrors are the switching elements. This setup enables to realize a real N $\times$ N interconnect compared to our 1 $\times$ N switch. However, without a macro-lens, the limits imposed by the divergence of the Gaussian beam are more severe. In fact, with a collimated waist diameter of typically $2w \cong 300$ μm (mirror diameter $\phi = 500$ μm), the Rayleigh range is only $z_r \cong 5$ cm. With an estimated path length of 10 cm,

the Lucent switch is at the limit of the size without penalty resulting from the divergence of the beam. The spacing between the fibers is 1 mm, imposed by the array of micro-mirrors with 500 μm diameter.

Other systems which have short switching times and use micro-mirrors have been reported. For example, Lin et al. reported a N × N switch [75, 26], using vertical micromirrors, schematically shown in Fig. 1.2. The light leaving a source fiber is collimated by a GRIN lens attached to the fiber. The vertical array of micro-mirrors redirects the light onto a receiver fiber. Here again, the divergence of the beam is a limiting parameter. Figure 5.3 shows the Rayleigh range for the collimated path and the maximum distance (path length) for several cross-connects as a function of the collimated beam waist. The calculations are based

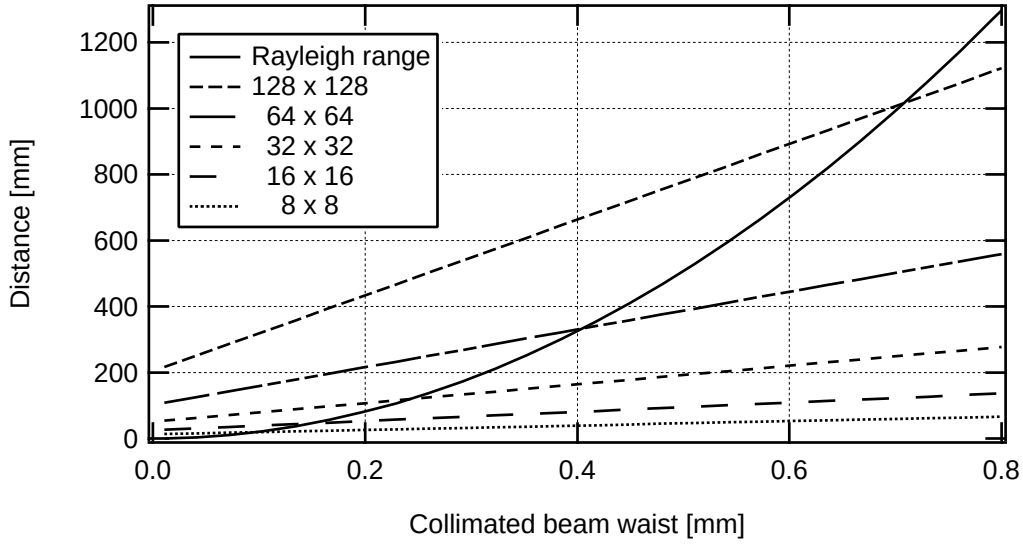

Figure 5.3: Rayleigh range within the collimated path and maximum distance for several N × N cross-connects as a function of the collimated beam waist. ($\lambda = 1550$ nm, $w_0 = 5.25$ μm)

on the parameters of a cross-connect reported by Lin et al. [75, 26]. He reports results for a collimated beam waist of 100 μm (mirror radius $r = 150$ μm) with insertion losses of 2.9 dB for the 16 × 16 cross-connect and of 6.9 dB for the 32 × 32 cross-connect. From Fig. 5.3, we see that a collimated beam waist of 100 μm limits the switch to 16 × 16 cross-connects. Larger collimated beam waists (and therefore larger mirrors) are needed for cross-connects with more than 16 × 16 connections.

As a final remark, we see that an optical switch for large number of interconnects has a minimum size given by the physical dimensions of the fibers

(ϕ_{fiber} = 125 μm), the number of fibers, and, by the physical properties (e.g. divergence) of Gaussian beams.

Bibliography

[1] A. G. Bell, "Selenium and the Photophone," *Nature*, vol. 22, pp. 500–503, 1880.

[2] T. H. Maiman, "Stimulated optical radiation in ruby," *Nature*, vol. 187, pp. 493–494, 1960.

[3] K. C. Kao and G. A. Hockham, "Dielectric-fibre surface waveguide for optical frequencies," *Proc. IEE*, vol. 113, no. 7, pp. 1151–1158, 1966.

[4] F. P. Kapron, D. B. Keck, and R. D. Maurer, "Radiation losses in glass optical waveguides," *Applied Physics Letters*, vol. 17, no. 10, pp. 423–425, 1970.

[5] V. M. Andreev Alferov, D. Z. Garbuzov, Yu. V. Zhilyaev, E. P. Morozov, E. L. Portnoi, and V. G. Trofim, "Effect of the heterostructure parameters on the laser threshold current and realization of continuous generation at room temperature," *Soviet Physics-Semiconductors*, vol. 4, pp. 1573–1577, 1970.

[6] I. Hayashi, M. B. Panish, P. W. Foy, and S. Sumski, "Junction lasers which operate continuously at room temperature," *Applied Physics Letters*, vol. 17, no. 3, pp. 109–111, 1970.

[7] T. C. Cannon, D. L. Pope, and D. D. Sell, "Installation and performance of the chicago lightwave transmission system," *IEEE Trans. Commun.*, vol. 26, no. 7, pp. 1056–1060, 1978.

[8] K. Oe, S. Ando, and K. Sugiyama, "1.3 μm CW operation of GaInAsP/InP DH diode lasers at room temperature," *Jpn. J. Appl. Phys.*, vol. 16, no. 7, pp. 1273–1274, 1977.

[9] J. I. Yamada, S. Machida, and T. Kimura, "2 Gbit/s optical transmission experiments at 1.3 μm with 44 km single-mode fibre," *Electron. Lett.*, vol. 17, no. 13, pp. 479–480, 1981.

[10] S. Fujita, M. Kitamura, T. Torikai, N. Henmi, H. Yamada, T. Suzuki, I. Takano, and M. Shikada, "10 Gbit/s, 100 km optical fibre transmission experiment using high-speed MQW DFB-LD and back-illuminated GaInAs APD," *Electron. Lett.*, vol. 25, no. 11, pp. 702–703, 1989.

[11] M. C. Amann, "Wide range tunable lasers for WDM applications," in *Fifth Optoelectronics Conference*, Makahuri Messe, Japan, 1994, pp. 208–209.

[12] A. K. Srivastava, Y. Sun, J. W. Sulhoff, C. Wolf, M. Zirngibl, R. Monnard, A. R. Chraplyvy, A. A. Abramov, R. P. Espindola, T. A. Strasser, J. R. Pedrazzani, A. M. Vengsarkar, J. L. Zyskind, J. Zhou, D. A. Ferrand, P. F. Wysocki, J. B. Judkins, and Y. P. Li, "1 Tb/s transmission of 100 WDM 10 Gb/s channels over 400 km of Truewave^{TM} fiber," in *Optical Fiber Communication Conference*, San Jose, CA, 1998, IEEE/OSA, Postdeadline paper PD10.

[13] Gordon A. Thomas, Boris I. Shraiman, Paul F. Glodis, and Michael J. Stephen, "Towards the clarity limit in optical fibre," *Nature*, vol. 404, pp. 262–264, 2000, 16 March.

[14] "Optical networking trial underway at university," *Fiber Product News*, November 2000.

[15] Jaafar M. H. Elmirghani and Hussein T. Mouftah, "Technologies and architectures for scalable dynamic dense WDM networks," *IEEE Communications Magazine*, pp. 58–66, 2000, February.

[16] H. Fujita and H. Toshiyoshi, "Micro-optical devices," in *Handbook of Microlithography, Micromachining, and Microfabrication*, P. Rai-Choudhury, Ed., pp. 435–516. SPIE, Bellingham, WA, first edition, 1997.

[17] M. Tachikura, T. Katagiri, and N. Kobayashi, "Strictly nonblocking 512x512 optical fiber matrix switch based on three-stage clos network," *IEEE Photonics Technology Letters*, vol. 6, no. 6, pp. 764–766, 1994.

[18] G. Gonzalez and S.D. Collins, "Magneitcally actuated fiber-optic switch with micromachined positioning stages," *Optics letters*, vol. 22, no. 10, pp. 709–711, 1997.

[19] Martin Hoffmann, Peter Kopka, and Edgar Voges, "All-silicon bistable micromechanical fiber switch based on advanced bulk micromachining," *IEEE Journal of Selected Topics in Quantum Electronics*, vol. 5, no. 1, pp. 46–51, 1999.

[20] Eric Ollier, Claude Chabrol, Thierry Enot, Patrick Brunet-Manquat, Jacques Margail, and Patrick Mottier, "1x8 micro-mechanical switches based

on moving waveguides for optical fiber network switching," in *International Conference on Optical MEMS*, Kaui, HI, 2000, pp. 39–40, IEEE/LEOS.

[21] Rolf Göring, Thomas Martin, Bernt Goetz, and Dirk Döring, "Miniaturized piezoelectrically driven fiber optics switches with transmittive microoptics," in *Miniaturized Systems with Micro-Optics and MEMS*, Santa Clara, CA, 1999, vol. 3878, pp. 136–143, SPIE.

[22] J. E. Ford and D. J. DiGiovanni, "1 x N fiber bundle scanning switch," *IEEE Photonics Technology Letters*, vol. 10, no. 7, pp. 967–969, 1998.

[23] Hiroshi Toshiyoshi, Guo-Dung John Su, Jason LaCosse, and Ming C. Wu, "Surface micromachined 2D lens scanner array," in *International Conference on Optical MEMS*, Kaui, HI, 2000, IEEE/LEOS, Post deadline paper.

[24] A. Azzam Yasseen, Joseph N. Mitchell, James F. Klemic, David A. Smith, and Mehran Mehregany, "A rotary electrostatic micromotor 1x8 optical switch," *IEEE Journal of Selected Topics in Quantum Electronics*, vol. 5, no. 1, pp. 26–32, 1999.

[25] P. M. Hagelin, U. Krishnamoorthy, J. P. Heritage, and O. Solgaard, "Scalable optical cross-connect switch using micromachined mirrors," *IEEE Photonics Technology Letters*, vol. 12, no. 7, pp. 882–884, 2000.

[26] L. Y. Lin, E. L. Goldstein, and R. W. Tkach, "On the expandability of free-space micromachined optical cross connects," *IEEE Journal of Lightwave Technology*, vol. 18, no. 4, pp. 482–489, 2000.

[27] Cornel Marxer and Nicolaas F. de Rooij, "Micro-opto-mechanical 2x2 switch for single-mode fibers based on plasma-etched silicon mirror and electrostatic actuation," *IEEE Journal of Lightwave Technology*, vol. 17, no. 1, pp. 2–6, 1999.

[28] D. T. Neilson, V. A. Aksyuk, S. Arney, N. R. Basavanhally, K. S. Bhalla, D. J. Bishop, B. A. Boie, C. A. Bolle, J. V. Gates, A. M. Gottlieb, J. P. Hickey, N. A. Jackman, P. R. Kolodner, S. K. Korotky, B. Mikkelsen, F. Pardo, G. Raybon, R. Ruel, R. E. Scotti, T. W. Van Blarcum, L. Zhang, and C. R. Giles, "Fully provisioned 112x112 micro-mechaincal optical cross-connect with 35.8Tb/s demonstrated capacity," in *Optical Fiber Communication Conference*, Baltimore, 2000.

[29] Q. Lai, W. Hunziker, and H. Melchior, "Low power compact 2 x 2 thermooptic silica-on-silicon waveguide switch with fast response," *IEEE Photonics Technology Letters*, vol. 10, no. 5, pp. 681–683, 1998.

[30] R. Krähenbühl, R. Kyburz, W. Vogt, M. Bachmann, T. Brenner, E. Gini, and H. Melchior, "Low-loss polarization-insensitive InP-InGaAsP optical space switches for fiber optical communication," *IEEE Photonics Technology Letters*, vol. 8, no. 5, pp. 632–634, 1996.

[31] E. Flück, F. Horst, B. J. Offrein, R. Germann, H. W. M. Salemink, and G. L. Bona, "Compact versatile thermooptical space switch based on beam steering by a waveguide array," *IEEE Photonics Technology Letters*, vol. 11, no. 11, pp. 1399–1401, 1999.

[32] N. A. Riza and S. Yuan, "Low optical interchannel crosstalk, fast switching speed, polarization independent 2 x 2 fibre optic switch using ferroelectric liquid crystal," *Electronics Letters*, vol. 34, no. 13, pp. 1341–1342, 1998.

[33] N. K. Shankar, J. A. Morris, C. P. Yakymyshyn, and C. R. Pollock, "A 2 x 2 fiber optic switch using chiral liquid crystals," *IEEE Photonics Technology Letters*, vol. 2, no. 2, pp. 147–149, 1990.

[34] R. McAdams, Larry, R. N. McRuer, and Joseph W. Goodman, "Liquid crystal optical routing switch," *Applied Optics*, vol. 29, no. 9, pp. 1304–1307, 1990.

[35] B.E.A Saleh and M.C. Teich, *Fundamentals of Photonics*, John Wiley & Sons, 1991.

[36] A. Yariv, *Optical Electronics in Modern Communications*, Oxford University Press, New York, fifth edition, 1997.

[37] Govind P. Agrawal, *Fiber-Optic Communication Systems*, John Wiley & Sons, 1992.

[38] John David Jackson, *Classical Electrodynamics*, John Wiley & Sons, second edition, 1975.

[39] I. N. Bronstein and K. A. Semendiaev, *Aide-mémoire de mathémathiques*, Eyrolles, Paris, eighth edition, 1985.

[40] Allan W. Snyder and John D. Love, *Optical Waveguide Theory*, Chapman and Hall, London, 1983.

[41] D. Marcuse, "Loss analysis of single-mode fiber splices," *The Bell System Technical Journal*, vol. 56, no. 5, pp. 703–718, 1977.

[42] Anthony E. Siegman, *Lasers*, University Science Books, Mill Valley, CA, 1986.

[43] H. Kogelnik and T. Li, "Laser beams and resonators," *Applied Optics*, vol. 5, no. 10, pp. 1550–1567, 1966.

[44] Virendra N. Mahajan, *Optical Imaging and Aberrations, PartI, Ray Geometrical Optics*, SPIE, Bellingham, 1998.

[45] H. H. Hopkins, *Wave theory of Aberrations*, Oxford University press, London, 1950.

[46] Daniel Malacara and Zacarias Malacara, *Handbook of lens design*, Marcel Dekker, New York, 1994.

[47] Joseph W. Goodman, *Introduction to Fourier Optics*, McGraw-Hill, second edition, 1996.

[48] H. P. Herzig, Ed., *Micro-Optics*, Taylor & Francis, London, 1997.

[49] W. T. Welford, *Aberrations of optical systems*, Adam Hilger, Bristol, 1986.

[50] Warren J. Smith, *Modern Optical Engineering*, McGraw-Hill, New York, second edition, 1990.

[51] H. P. Herzig and R. Dändliker, "Holographic optical scanning elements: analytical method for determining the phase function," *Journal of the Optical Society of America A*, vol. 4, no. 6, pp. 1063–1070, 1987.

[52] Gleb Vdovin and Simon Middelhoek, "Technology and applications of micromachined silicon adaptive mirrors," *Opt. Eng.*, vol. 36, no. 5, pp. 1382–1390, 1997.

[53] R. P. Grosso and M. Yellin, "The membrane mirror as an adaptive optical element," *J. Opt. S. Am.*, vol. 67, pp. 399–406, 1977.

[54] William D. Cowan, Max K. Lee, Byron M. Welsh, Victor M. Bright, and Michael C. Roggemann, "Surface micromachined segmented mirrors for adaptive optics," *IEEE Journal of Selected Topics in Quantum Electronics*, vol. 5, no. 1, pp. 90–101, 1999.

[55] Thomas G. Bifano, Julie Perreault, Krishnamoorty Raji Mali, and Mark N. Horenstein, "Microelectromechanical deformable mirrors," *IEEE Journal of Selected Topics in Quantum Electronics*, vol. 5, no. 1, pp. 83–89, 1999.

[56] R. K. Tyson, *Principles of adaptive optics*, Academic Press, San Diego, CA, second edition, 1998.

[57] Gleb Vdovin, *Adaptive Mirror Micromachined in Silicon*, Ph.D. thesis, TU-Delft, 1996.

[58] C. Paterson, I. Munro, and J. C. Dainty, "A low cost adaptive optics system using a membrane mirror," *Optics Express*, vol. 6, no. 9, pp. 175–185, 2000.

[59] Ph. Nussbaum, R. Völkel, H. P. Herzig, M. Eisner, and S. Haselbeck, "Design, fabrication and testing of microlens arrays for sensors and microsystems," *Pure & Applied Optics*, vol. 6, pp. 617–636, 1997.

[60] Max Born and Emil Wolf, *Principles of Optics*, Cambridge University Press, Cambridge, sixth edition, 1999.

[61] Johannes Schwider and Oliver Falkenstörfer, "Twyman-Green interferometer for testing microspheres," *Optical Engineering*, vol. 34, no. 10, pp. 2972–2975, 1995.

[62] David B. Fogel, "An introduction to simulated evolutionary optimization," *IEEE Transactions on Neural Networks*, vol. 5, no. 1, pp. 3–14, 1994.

[63] Gleb Vdovin and P. M. Sarro, "Flexible mirror micromachined in silicon," *Applied Optics*, vol. 34, no. 16, pp. 2968–2972, 1995.

[64] Flexible Optical BV, "http://www.okotech.com," 2000.

[65] H. Kiessling, U. Danzer, and J. Schwider, "Monomode fiber-array connectors," Annual report, Universität Erlangen-Nürnberg, 1996.

[66] Yasuhiko Aoki, Toshio Kato, Rogerio Jun Mizuno, and Kenichi Iga, "Micro-optical bench for alignment-free optical coupling," *Applied Optics*, vol. 38, no. 6, pp. 963–965, 1999.

[67] H. Kuwahara, M. Sasaki, and N. Tokoyo, "Efficient coupling from semiconductor lasers into single-mode fibers with tapered hemispherical ends," *Applied Optics*, vol. 19, no. 15, pp. 2578–2583, 1980.

[68] Jun-Ichi Yamada, Yasuji Murakami, Jun-Ichi Sakai, and Tatsuya Kimura, "Characteristics of a hemispherical microlens for coupling between a semiconductor laser and single-mode fiber," *IEEE Journal of Quantum Electronics*, vol. 16, no. 10, pp. 1067–1072, 1980.

[69] H. M. Presby, A. F. Benner, and C. A. Edwards, "Laser micromachining of efficient fiber microlenses," *Applied Optics*, vol. 29, no. 18, pp. 2692–2695, 1990.

[70] Christopher A. Edwards, Herman M. Presby, and Corrado Dragone, "Ideal microlenses for laser to fiber coupling," *Journal of Lightwave Technology*, vol. 11, no. 2, pp. 252–257, 1993.

[71] William L. Emkey and Curtis A. Jack, "Analysis and evaluation of graded-index fiber-lenses," *Journal of Lightwave Technology*, vol. 5, no. 9, pp. 1156–1164, 1987.

[72] P. Chanclou, M. Thual, J. Lostec, D. Pavy, M. Gadonna, and A. Poudoulec, "Collective microoptics on fiber ribbon for optical interconnecting devices," *Journal of Lightwave Technology*, vol. 17, no. 5, pp. 924–928, 1999.

[73] P. Chanclou, M. Thual, J. Lostec, D. Pavy, and M. Gadonna, "Focusing and coupling properties of collective micro-optics on fiber ribbons," *Opt. Eng.*, vol. 39, no. 2, pp. 387–392, 2000.

[74] P. M. Hagelin, U. Krishnamoorthy, C. M. Arft, J. P. Heritage, and O. Solgaard, "Scalable fiber optic switch using micromachined mirrors," in *Transducers'99*, Sendai, Japan, 1999, pp. 782–785.

[75] L. Y. Lin, E. L. Goldstein, and R. W. Tkach, "Free-space micromachined optical switches for optical networking," *IEEE Journal of Selected Topics in Quantum Electronics*, vol. 5, no. 1, pp. 4–9, 1999.

Acknowledgments

Although this thesis is a personal work, many people contributed to its achievement. Some directly for the scientific work and other less directly, but as much important, by their interaction in the everyday life. I would like to express here my special thanks to:

Prof. René Dändliker for being my thesis advisor and giving me the opportunity to realize this work in his group as well as for his helpful comments and advises.

Prof. Hans Peter Herzig who directly supervised this work and brought many ideas through discussions.

The other members of the jury: Prof Olav Solgaard and Dr. Gian-Luca Bona for their critical review of my thesis.

Dr. Etienne Rochat who introduced me to the world of optical fibers and contributed to the realization of a pulsed fiber laser. We also spent motivating lunch breaks sailing on the lake of Neuchâtel.

Dr. Cornel Marxer whose mirrors enabled to realize my first MOEMS experiments.

Stefano Bottinelli who realized xy-stages by electro-erosion.

Dr. Yves Salvadé for introducing me to LabVIEW programming as well as to the St-Martin tradition in Jura.

Frédéric Gonté, the "specialist" of the deformable mirror. Together, we realized the adaptive experiments.

Dr. Ken Weible who gave me some of his knowledge for transferring structures into optical materials using the Ion Beam Milling and the STS Induced Coupled

Plasma facilities.

Jean-Christophe Roulet for valuable discussions about innovative realizations, but also for the 24 crazy hours we spent skiing together without interruption.

Irène Philipoussis for fabricating the microlenses.

Marcel Groccia for the electronic realizations, but overall for his kindness.

Jean-Luc Kumin and Jean-René Von Allmen for their help in conceiving mechanical constructions and for their fabrication.

Urban Schnell, Sike Traut, Antonnello Nesci and Olivier Ripoll with who I shared the same office during several years.

Mary-Claude Gauteaub, Sandrine Piffaretti, Joëlle Banjac, Caroline Huguenin and Martial Racine for their perfect administrative work.

All the members of the Applied Optics group and more generally of the Institute of Microtechnology for the nice and stimulating atmosphere.

My parents who continuously supported me throughout all these years and who gave me many encouragements.

My wife Marie for her love, her patience and her support which were particularly welcome during the last months.